
Flip Chip
Bonding Technologies
for
Hybrid Integration

Mark Fretz

2009

FACULTE DES SCIENCES

Secrétariat-Décanat de la faculté

- Rue Emile-Argand 11
- CP 158
- CH-2009 Neuchâtel

IMPRIMATUR POUR LA THESE

Flip Chip Bonding Technologies for Hybrid Integration

Mark FRETZ

UNIVERSITE DE NEUCHATEL

FACULTE DES SCIENCES

La Faculté des sciences de l'Université de Neuchâtel,
sur le rapport des membres du jury

MM. H.P. Herzig (directeur de thèse),
W. Noell, T. Scharf, C. Bosshard (CSEM-Alpnach)
et T. G. Harvey (Epigem, Redcar UK)

autorise l'impression de la présente thèse.

Neuchâtel, le 24 septembre 2009

Le doyen :
F. Kessler

UNIVERSITE DE NEUCHATEL
FACULTE DES SCIENCES
Secrétariat - décanat de la faculté
Rue Emile-Argand 11 - CP 158
CH-2009 Neuchâtel
Felix Kessler

To Marlène Zbinden
and to
my Parents; Béatrice and Peter

Table of Contents

Abstract	vii
Zusammenfassung	ix
1 Introduction	1
1.1 Aim of this work	1
1.2 State of the art bonding and flip chip bonding techniques	2
1.3 Flip chip bonding technologies for hybrid integration . . .	4
1.4 Novel approaches in this work	4
1.5 The structure of the thesis	4
2 Flip Chip Bonding Technologies	7
2.1 Introduction	7
2.2 Test device: design and fabrication	9
2.3 Measurement method and setup	17
2.4 Bonding procedures	21
2.4.1 Flip chip bonding with eutectic AuSn20 solder . . .	21
2.4.2 Thermocompression bonding with gold studs . . .	27
2.4.3 Flip chip bonding with anisotropic conductive ad- hesives (ACA)	31
2.5 Results and discussion	37
2.6 Conclusions and outlook	43
3 CASE I: Pressure Strip	45
3.1 Introduction	46
3.2 System design	47
3.3 Bonding procedure	49
3.4 Characterisation	53
3.4.1 Measurement method and setup	56
3.4.2 Response to pressure and temperature	57
3.4.3 Sensitivity and TCS	58
3.4.4 Offset and TCO	65
3.5 Wind tunnel tests	71
3.6 Highly-integrated pressure strip	71
3.7 Conclusions and outlook	73

4	Novel Approaches to Sensor Packaging	75
4.1	Introduction	75
4.2	ACA bonding on PMMA	78
4.2.1	Characterisation of electrical and mechanical contact	78
4.2.2	Characterisation of sealing properties	80
4.2.3	Reliability	83
4.2.4	Autoclave tests	91
4.2.5	Conclusions	95
4.3	Flip chip packaging of MEMS devices	96
4.3.1	Experimental procedure	96
4.3.2	Results	99
4.3.3	Discussion	101
4.3.4	Conclusions	102
4.4	Simulation of hygro swelling induced stresses in a MEMS device	103
4.4.1	Simulation model	104
4.4.2	Diffusion	104
4.4.3	Hygro swelling	106
4.4.4	Comparison between hygro swelling and thermally induced deformation	107
4.4.5	Conclusions	109
5	CASE II: Flow Sensor	113
5.1	Introduction	113
5.2	System design	114
5.2.1	Concept	114
5.2.2	Governing equations	115
5.2.3	Design	116
5.3	Bonding procedures	119
5.4	Characterisation	119
5.4.1	Measurement method and setup	121
5.4.2	Sensitivity and flow rate range	122
5.4.3	Temperature dependence of offset	125
5.4.4	Response time	125
5.5	Conclusions	127
6	Conclusions and Outlook	129
6.1	Conclusions	129
6.2	Outlook	130

A 4-Point Measurement Error Estimation	131
B Number of spheres within a contact in ACA bonding	132
Bibliography	135
List of Figures	143
List of Tables	147
List of Publications	149
Acknowledgement	151
Curriculum Vitae	153

Abstract

Hybrid integration and especially the packaging of microelectromechanical systems (i.e. MEMS) cannot rely on standardised packaging solutions due to the diversity of microsystems. As an example, the packaging requirements of a pressure sensor are different from that of an accelerometer. Usually pressure sensors do not require a special sealing, whereas accelerometers need to be hermetically packaged. On the other hand, diaphragm-based (i.e. membrane) pressure sensors ask for special precautions in the die-attach process: Mismatches of the *coefficient of thermal expansion* between the components of the package may induce stress and strain in the membrane. Since the output signal of a pressure sensor is a measure of the static deformation of the membrane, temperature variations of the environment may render an improperly attached pressure sensor useless. Moreover, an inappropriate bonding process may bias the output signal or the bonding process may render the pressure sensor even useless.

In the present work several flip chip bonding processes with the focus on electrical properties and applicability were evaluated. Specifically, a bonding process based on anisotropic conductive adhesives (ACA) suitable for diaphragm-based pressure sensors was developed. The flip chip bonded sensors respond linearly to the applied pressure. The sensitivity to pressure and the offset shift due to temperature changes are within the tolerances of the sensor die according to the data sheet.

The developed ACA-bonding process provides electrical and mechanical connection as well as fluidic sealing of the membrane to the outside world.

Small changes of the bonding process allowed to adapt the process to plastic substrates with a low glass transition temperature T_g . Such substrates are usually employed in microfluidic applications because they are low-cost, easy to machine, resistant to acids and lyes, and compatible with most chemical and biological materials. Specifically, it was shown that the process is capable of bonding Si-chips onto PMMA substrates with a T_g of 100 °C. The process is especially suited for semiconductor chips which are too small for a standard microgasket approach.

The results of the process development were applied to two novel cases:

i) A *pressure strip* was developed which provides a non-destructive way to measure flow and pressure distributions and arbitrarily shaped bodies. The pressure strip consists of three components: A mechanically rigid carrier with an array of pressure sensors which transform the measured pressure into an electrical signal, a mechanically flexible fluidic strip which comprises openings and microfluidic channels which detect and guide the pressure signal to the pressure sensors, and a flexible electronic strip which processes the electronic signals and provides electrical connection to the outside world. Functionality was proven in a wind tunnel. Furthermore, the sensitivity to pressure and temperature was measured and are within the tolerances of the pressure sensors specifications which proves the quality of the developed bonding process.

ii) A novel *flow sensor* to measure very low-rate flows in the range of $1 \mu\text{l/s}$ was designed and implemented by using the previously developed flip chip ACA-bonding process. The concept is based on the measurement of pressures of a fluid at the inlet and outlet of a microchannel. These pressures are guided to the front and back side of a differential pressure sensor. The pressure sensor is hence exposed only to the relatively small pressure difference between inlet and outlet. The system pressure has no impact on the pressure sensor. Existing flow sensors with comparable flow rate ranges either have longer response times or are sensitive to pressure peaks.

Zusammenfassung

Die Aufbau- und Verbindungstechnik von hybriden Systemen und mikroelektromechanischen Systemen (abgekürzt: MEMS) kann aufgrund der Vielfältigkeit von Mikrosystemen nicht auf standardisierte Prozesse zurückgreifen. Die Anforderungen an die Integration eines Drucksensorchips unterscheiden sich z.B. signifikant von denen an die Integration eines Beschleunigungssensors, wie er z.B. in Motorfahrzeugen zur Steuerung von Airbags zum Einsatz kommt. Üblicherweise bestehen keine speziellen Anforderungen an die Versiegelung von Drucksensorchips, wohingegen Beschleunigungssensoren hermetisch versiegelt sein müssen. Andererseits verlangen Drucksensorchips spezielle Vorkehrungen beim Verbinden mit dem Träger. Steife Verbindungen von Materialien mit unterschiedlichen Wärmeausdehnungskoeffizienten (CTE) rufen Spannungen und Verformungen in der Membrane des Drucksensorchips hervor. Da das Ausgangssignal eines Drucksensors ein Mass der statischen Verformung der Membrane ist, können Schwankungen der Umgebungstemperatur den Sensor bei unpassender Verbindungstechnik unbrauchbar machen. Darüberhinaus kann ein unangemessener Verbindungsprozess Verformungen in der Membrane hervorrufen, welche das Ausgangssignal unmittelbar verfälschen.

Wir präsentieren einen Flip-Chip-Verbindungsprozess, welcher auf anisotrop leitendem Epoxidkleber (ACA) basiert. Wir konnten zeigen, dass dieser Prozess geeignet ist für membranbasierte Drucksensorchips. Das Ausgangssignal des auf diese Weise geklebten Drucksensors reagiert linear auf äussere Druckschwankungen. Dabei liegen die Druck- und Temperaturempfindlichkeit innerhalb der vom Datenblatt des Sensors vorgegebenen Toleranzen.

Der von uns entwickelte ACA-Verbindungsprozess stellt sowohl den elektrischen als auch den wasserdichten mechanischen Kontakt her, welcher die Membrane einseitig von der Aussenwelt abschirmt.

Kleine Anpassungen am Verbindungsprozess ermöglichten den Einsatz von polymeren Trägermaterialien mit einer Glasübergangstemperatur T_g im Bereich von $100\text{ }^\circ\text{C}$. Solche polymeren Substrate sind in der Mikrofluidik weitverbreitet, weil sie kostengünstig, einfach zu bearbeiten, relativ beständig gegen Säuren und Basen und kompatibel mit den häufigsten Chemikalien (mit Ausnahme von Alkohol) und biologi-

schen Materialien sind. Wir konnten zeigen, dass der Prozess das Verbinden von Siliziumchips und PMMA-Substraten erlaubt. Der Prozess eignet sich besonders für Halbleiterchips, welche zu klein sind für die 'Microgasket'-Verbindungsmethode.

Die gewonnenen Erkenntnisse über die untersuchten Verbindungstechniken ermöglichten die Verwirklichung von zwei Demonstratoren:

i) Ein *druckempfindlicher Streifen* zur nichtinvasiven Messung von Gas- und Flüssigkeitsströmen und Drücken auf beliebig geformten Oberflächen wurde entwickelt. Der Streifen besteht aus drei Komponenten: einem mechanisch steifen FR4-Träger mit den Drucksensoren, welche den gemessenen Druck in elektrische Signale umwandeln; einer mechanisch flexiblen 'fluidischen' Folie mit Öffnungen und mikrofluidischen Kanälen, welche den Druck zu den Sensoren weiterleitet; und einem flexiblen elektronischen Streifen, welcher die elektronischen Komponenten zur Signalverarbeitung aufnimmt. Die Funktionalität wurde an einem Flügelmodell in einem Windkanal nachgewiesen. Darüberhinaus wurde die Empfindlichkeit der integrierten Drucksensoren auf Druck und Temperaturschwankungen bestimmt. Die gemessenen Werte liegen innerhalb der im Datenblatt der Sensoren angegebenen Toleranzen, was ein Beleg für die Qualität des entwickelten Verbindungsprozesses ist.

ii) Ein neuartiges *Flusssensor*-Konzept zur Messung von Flussraten im Bereich von $1 \mu\text{l/s}$ wurde entwickelt und umgesetzt. Dabei fand der vorgängig entwickelte ACA-Verbindungsprozess Verwendung. Das Konzept des Flusssensors basiert darauf, dass die Drücke eines Fluids am Anfang und Ende eines Mikrokanals jeweils zu Vorder- und Rückseite der Membrane eines Drucksensorchips geleitet werden. Der Sensor wird dadurch nur der relativ kleinen Druckdifferenz ausgesetzt, welche sich entlang des Kanals ausbildet. Der Systemdruck selbst wirkt nicht auf die Membrane.

Introduction

1.1 Aim of this work

The aim of this thesis is twofold: to investigate and develop flip chip bonding techniques with regard to microelectromechanical systems and chips with a sensing element and to apply the results to different applications and cases.

MEMS devices such as diaphragm-based pressure sensors [1] are sensitive to external loads. The package of such a device must provide protection as well as electrical and mechanical connection to the outside world while maintaining the performance of the MEMS device.

Flip chip bonding and interconnection technology are wide research fields [2]. However, standard bonding techniques are not easily adapted to MEMS packaging. For instance, epoxy bonding provides a strong mechanical connection. Thermally induced expansion of the carrier board will therefore induce stresses and/or strains in the MEMS device due to differences in the *coefficient of thermal expansion* [3] of the components. Thermally induced stresses [4] may limit the temperature range in which the packaged MEMS devices work properly and may render necessary temperature measurements of the package and frequent calibration.

The main goals of this thesis can therefore be summarised as follows:

- Evaluation of flip chip bonding techniques with a focus on electrical performance and applicability.
- Process development of flip chip bonding processes for MEMS and low T_g substrates.
- Implementation of the bonding processes in specific cases. These are
 - Microfluidic applications
 - Case I: Pressure sensing devices
 - Case II: Flow sensor device

1.2 State of the art bonding and flip chip bonding techniques

There are four interconnection techniques in electronic packaging: Wire bonding, flip chip bonding, beam lead, and TAB (Tape Automated Bonding). Among these interconnection techniques wire bonding is the most used process because it requires no special treatment of the chip or processing of the bond pads. Especially in the development phase of chip or package it is convenient to employ wire bonding. Design changes in pad geometry or size only require reprogramming of the wire bonding machine. A drawback are the long wires which are a limiting factor in high-frequency applications. A thorough discussion on the existing interconnection methods is found in [5].

Reflow chip joining with solder bumps is the most widespread and advanced flip chip technology. It provides the highest reliable interconnections of all flip chip processes and is well characterised. The drawbacks are the need of chip pad preparation (UBM = under bump metallisation, enables soldering) because commonly used aluminum pads are not solderable due to a native oxide layer which is not easily removed by solder-enhancing fluxes. The solder bumps need to be protected against corrosion and mechanical impact due to thermal expansion mismatches of the components and external loads. An epoxy underfill is usually employed to fill the gap between chip and substrate. It protects the solder balls from moisture and reduces the stresses by distributing the forces on a larger surface.

Alternatives to soldering are thermocompression processes (see table 1.1). Usually, protruding gold sockets are produced on the aluminum pads. Heat and pressure during bonding provides a welded joint between the gold socket (i.e. gold stud or gold bumps) and the bond pad of the substrate. Thermocompression bonding is an alternative for devices which do not allow solder processes. The drawbacks are the comparably high bonding temperatures and forces. Not every chip can stand such a process. This method does not require UBM nor controlled atmosphere or fluxes. Gold bumps are not prone to corrosion. Therefore, underfilling the gap with an epoxy is not necessarily needed if the chip is protected by the package against external mechanical loads.

Flip chip bonding with anisotropic conductive adhesive (ACA) combines the advantages of underfills and bonding with gold bumps in one bonding step: Small conductive particles are dispersed in an epoxy-matrix. The particle density is not high enough to provide homogeneous

- Eutectic/non-eutectic solder ball assembly with [2]
 - capillary underfill [6]
 - no-flow underfill [6]
- Flip chip assembly using gold studs [2]
 - thermocompression [7]
 - thermosonic bonding [8]
 - non-conductive adhesive [9]
 - conductive adhesive (dipping) [2]
- Anisotropic conductive adhesive assembly [2]
 - paste (usually called ACA) [10]
 - film (usually called ACF) [11]
- Conductive adhesive bump assembly [2, 12]
 - thermoplastic adhesive [13]
 - thermoset adhesive [14]

Table 1.1: Most common flip chip bonding processes and references for further reading.

conductivity. Electrical interconnection is established by the conductive particles which are squeezed between the opposing bond pads of chip and substrate. The ACA can be dispensed on the interconnect array of the substrate. The chip is attached with ACA. Relatively low bonding forces and temperatures are required for electrical connection. Gold bumps on the chip pads define the contact surface and the bondline thickness (BLT, i.e. thickness of the gap between chip and substrate). The ACA matrix protects the interconnects against moisture and adds strength to the joint.

Table 1.1 lists the most common flip chip processes and references for further reading. Beam lead and TAB are not discussed as they are not relevant for the present work.

1.3 Flip chip bonding technologies for hybrid integration

In this thesis, we refer to *hybrid integration* as a combination of different materials for substrates and chips (e.g. ceramics, plastics, metals, and semiconductors) and the combination of different bonding techniques. Possible applications of the here developed flip chip processes go beyond electronic packaging which has a different definition of hybrid integration [5]. We mainly target sensor applications such as non-invasive pressure measurement on aerodynamic bodies, liquid handling, analytical instrumentation, lab-on-a-chip, and molecular diagnostics.

1.4 Novel approaches in this work

We present for the first time a flip chip bonding process with ACA which is able to package stress-sensitive devices such as MEMS. The bonding process is especially suited for microfluidic applications because the adhesive provides electrical and strong mechanical connection as well as fluidic sealing of the sensing element of a chip.

Comprehensive studies on face-up bonded diaphragm-based differential pressure sensors were carried out in this thesis. The results are benchmarks for the characteristics of flip chip bonded pressure sensors.

The bonding methods were then used to realise a pressure sensing strip for non-destructive measurement of pressures on arbitrarily shaped bodies and a novel flow sensor concept based on a differential pressure sensor. Furthermore, the ACA bonding process was adapted to enable bonding of Si-chips onto plastic substrates with a low glass transition temperature T_g .

1.5 The structure of the thesis

This thesis is structured as follows: Chapter 2 summarises the investigated flip chip bonding processes 'bonding with eutectic AuSn20 solder', 'thermocompression with gold studs', and 'bonding with anisotropic conductive adhesive' (ACA). The research focuses on electrical properties of the flip chip interconnects and feasibility of the bonding processes.

Chapter 3 deals with face-up bonding of diaphragm-based (i.e. membrane) differential pressure sensors. The investigated bonding methods are adhesive bonding with compliant silicone and hard epoxy. As from now we refer to face-up silicone bonding as 'standard bonding' because

it is a widespread method for pressure sensor bonding. The developed bonding method was used to implement a pressure sensing strip.

The measured characteristics of such bonded sensors are benchmarks for flip chip bonded pressure sensors.

Chapter 4 introduces novel approaches to sensor packaging. On the one hand, the here developed flip chip process with ACA is especially suited for low-cost microfluidic devices including drug deliver and liquid handling applications. On the other hand, the process allows flip chip bonding of stress-sensitive MEMS devices demonstrated with a diaphragm-based differential pressure sensor.

A flow sensor for very low flow-rates is described in chapter 5. The key packaging technology is the flip chip process with ACA introduced in chapter 4.

Chapter 6 summarises the main results of this thesis and identifies potential further improvements of the processes and their applications.

Flip Chip Bonding Technologies

2

Flip chip bonding is the face-down attachment of electronic components onto substrates, PCBs, and carriers. Conductive bumps provide electrical and mechanical connection. Flip chip is in competition to wire bonding and Tape-automated bonding (TAB).

In the 1960's, IBM invented a solder-bumped flip chip process, so-called C4 (Controlled Collapse Chip Connect) [15]. Flip chip was meant to replace widespread wire bonding, because, at this time, wire bonding was considered expensive, unreliable, and low-productive [2]. But wire bonding was further developed. Nowadays it is a fast, automated, flexible and high-yield process [16]. It meets today's needs of semiconductor industries. Furthermore, the expensive infrastructure for wire bonding (and flip chip bonding) and many years of experience have prevented manufacturers of electronics components from replacing wire bonding by flip chip technologies.

Today, flip chip is applied where semiconductor manufacturers or packaging companies profit from its advantages in size, cost, reliability, and performance over wire bonding:

- Flip chip technology provides improved performance. Due to short electrical connections inductance is low. It allows higher frequency applications with low crosstalk.
- The whole front surface of a chip can be used for interconnection pads. Wire bonds require bond pads at the peripherals, increasing the chip size as the number of bond pads increases.
- Flip chip bonding requires less height if wire bonding and protection (e.g. overmold) are eliminated.

2.1 Introduction

Face-down attachment with solder bumps (usually Pb containing) is the most widespread flip chip technology. The down-facing chips are tacked by a flux which promotes wetting of the solder pads by spreading over

the pads and by reducing native oxides. Other solder materials like eutectic AuSn20 do not need fluxes, as the high Au content prevents strong oxidation.

Apart from soldering, there are other flip chip technologies like thermocompression, anisotropic conductive adhesives (ACA) bonding, and bonding with conductive polymer bumps. There are two driving forces for new flip chip technologies: Cost reduction and bonding limitations. The first is an important factor in high-volume production and cost-conscious industries, the latter in cases where delicate components or special requirements in packaging rule out solder-bumped flip chip bonding.

This chapter characterises and compares three flip chip techniques which are not yet widespread: Fluxless soldering with eutectic AuSn20 solder bumps, thermocompression (TC) with gold stud bumps, and bonding with anisotropic conductive adhesive with regard to electrical performance and ease of bonding process.

Eutectic AuSn20 solder (figure 2.1) is nowadays mainly used in optoelectronics applications, where flux residues alter the performance of optics components like lenses or laser dies.

Thermocompression with gold stud bumps eliminates the need of

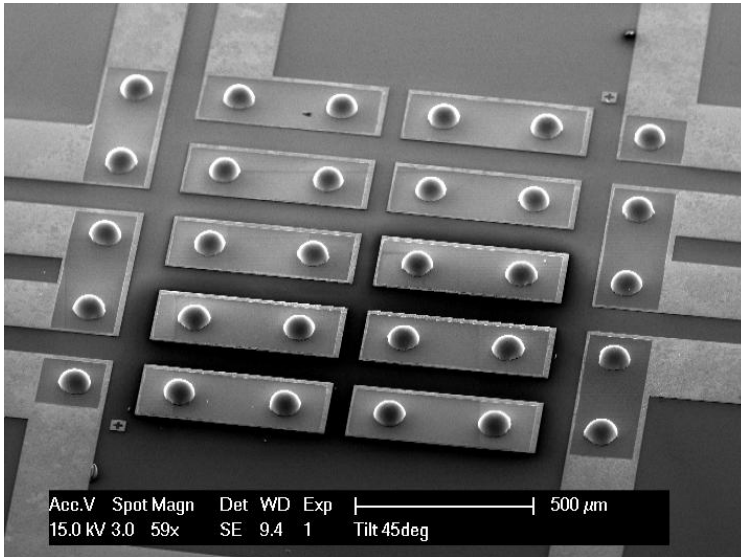


Figure 2.1: Test device with an array of solder bumps.

under-bump metallisation (UBM). Therefore, it can reduce cost.

ACA bonding, like TC bonding, eliminates the need of UBM. The electrical contact is provided by gold studs and conductive particles which are dispersed in the ACA matrix. A detailed description of the bonding processes and their characteristics are given in section 2.4. Measurement method and setup are described in section 2.3, and design and fabrication of the test devices are presented in section 2.2.

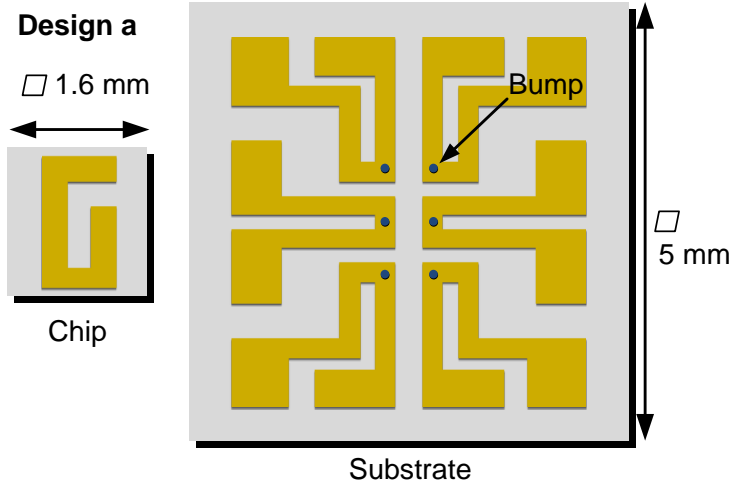
2.2 Test device: design and fabrication

Design

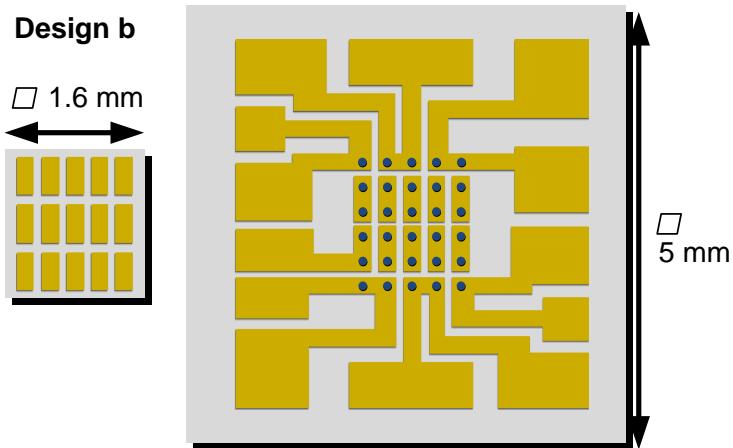
In order to characterise flip chip bonding techniques, two distinct sets of substrate and chip with appropriate metal structures were designed for measuring electrical resistances of single bumps and so-called daisy-chains (a series of contacts). Figure 2.2 depicts the metal structures of the chips and the substrates. The substrate provides larger landing pads at the peripherals which can be contacted by probe needles.

Design (a) comprises sites for six flip chip contacts (depicted with circles in figure 2.2(a)). It can be either a gold stud bump or solder bump assembly. For the latter case, a Si_3Ni_4 passivation layer was added on top of the metal layer. More information on the passivation layer is given below. The metallisation of the chip is designed in a way that it electrically connects all bumps. It allows determination of the resistance of the four bumps, labelled with 1,2,3, and 4 on the left side in figure 2.3. Two probe needles are required for driving a current, and two probe needles for measuring the voltage drop across a bump. A detailed description of the measurement principle is given in section 2.3 and [2].

Design (b) comprises sites for 30 flip chip contacts (figure 2.2(b)). The chip metallisation is designed in such a manner that they form a daisy-chain (contacts in series) with the substrate metallisation and the bumps, as depicted on the right side in figure 2.3. If current-driving probes are contacting the pads labelled with IN and OUT1, a current is driven through all 30 bumps, alternately going up and down the bumps and along the metal lines between the bumps. The measured resistance value is the sum of all resistances in the path of the current. Furthermore, the resistance of single columns -consisting of 6 serial bumps- can be measured when the probes connect the pads IN and OUT2. In contrast to design (a), the metal lines between the bumps contribute to the measured resistance. Hence, this design can not be used to precisely measure bump resistances. The benefit of this design is that we can gain information about the bonding process itself. It provides knowl-



(a) Test device for measuring electrical resistances of single bumps.



(b) Test device for measuring electrical resistances of daisy-chains.

Figure 2.2: Design of test devices for characterisation of single bumps and daisy-chains.

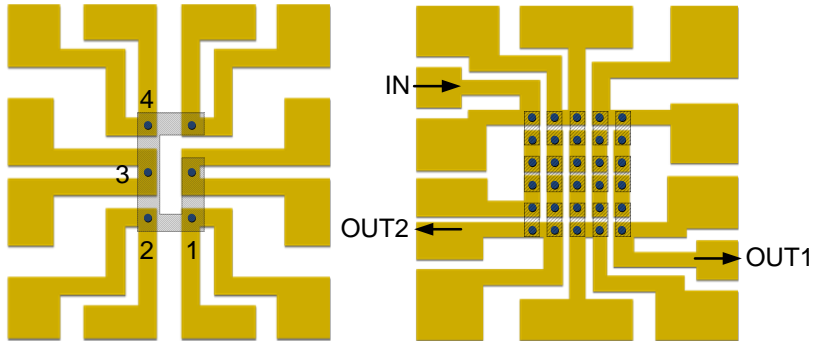


Figure 2.3: Overlaid metal structures of chip and substrate. The hatched shapes depict the chip metallisation.

edge about the repeatability and ease of the bonding process and its dependency on the bonding parameters like bonding temperature and force, atmosphere, and alignment precision between chip and substrate. The less critical the process is, the bigger the process window becomes. Small process windows usually require expensive and sometimes slow process equipment, which can precisely control the bonding parameters.

Daisy-chains are also employed to detect small changes in the contact resistance like early corrosion. In a daisy-chain the increase in resistance is multiplied, provided that all flip chip contacts are subject to the same environmental conditions.

Fabrication

Two types of devices were fabricated for each design. *First type* devices have simple metal structures on a silicon or borofloat substrate. Some devices of this type also have Si_3Ni_4 structures on top of the metal, which act as a flow stop for soldering processes.

Second type devices additionally have eutectic AuSn20 solder bumps on the substrate.

First type devices without solder bumps were fabricated at Division C of CSEM¹. As substrate material we used 4" silicon and borofloat wafers. The silicon wafers were treated in a furnace in order to grow a 2 μm thick electrically passivating oxide layer, as shown in figure 2.4.

¹Division C runs CSEM's wafer fab, located at the headquarter in Neuchâtel, Switzerland.

A positive photoresist was spin-coated on the wafers, prebaked, and photolithographically structured. Then three metals were sequentially evaporated on the wafers: $0.06\ \mu\text{m}$ titanium (as adhesion layer), followed by $0.2\ \mu\text{m}$ platinum (acting as diffusion barrier and wetting layer) and $1\ \mu\text{m}$ gold. The thick gold layer should guarantee long-term stability of the metal system, because thin gold layers below $0.2\ \mu\text{m}$ are known to be permeable. Oxides can reach subjacent metal layers and cause oxidation or even corrosion. Atoms of the subjacent metal layer can diffuse to the surface of the gold layer. Both processes alleviate solderability (by reducing wettability of the subjacent layer) and wire-bondability of the gold surface, which is required for a reliable stud bump process [16]. This is a well-known phenomena for nickel layers which are protected by a thin gold layer. If such devices are not stored in non-oxidising atmospheres, solderability and wettability will decrease in time. Even though platinum does not oxidise at any temperature, it is corroded by halogens and sulfur.

After having stripped the resist, a $0.2\ \mu\text{m}$ thick Si_3Ni_4 layer was grown by means of a plasma enhanced chemical vapour deposition process (PECVD). Photoresist was coated and photolithographically structured in order to protect the Si_3Ni_4 structures in the subsequent etching process. Finally, the resist was stripped and the wafer diced.

Second type devices with AuSn20 solder bumps were fabricated at Division C and IZM². The process flow is depicted in figure 2.5, the process steps carried out by IZM are starred.

First, a thin TiW and a $0.12\ \mu\text{m}$ thick gold layer were sputtered. This metal was used as a base for the subsequent electroplating process, in which a $1.5\ \mu\text{m}$ thick gold layer was deposited. This layer was structured by photolithography to form the final metal structure of the device. The Si_3Ni_4 layer was fabricated as already described in the process for first type devices. Then the solder was electroplated in openings of the previously structured photoresist. Finally, the resist was stripped, the plating base etched, and the solder bumps were reflowed.

²Fraunhofer-Institut für Zuverlässigkeit und Mikrointegration IZM, Berlin.

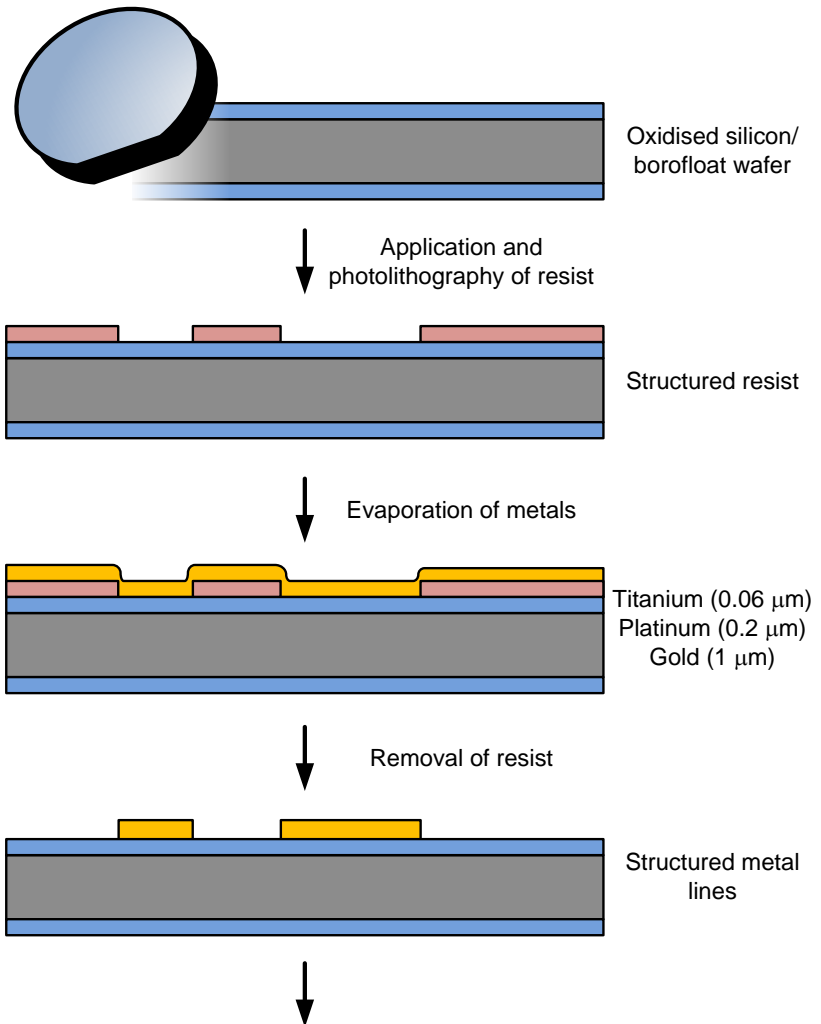


Figure 2.4: Process flow of devices for gold stud bump assembly.

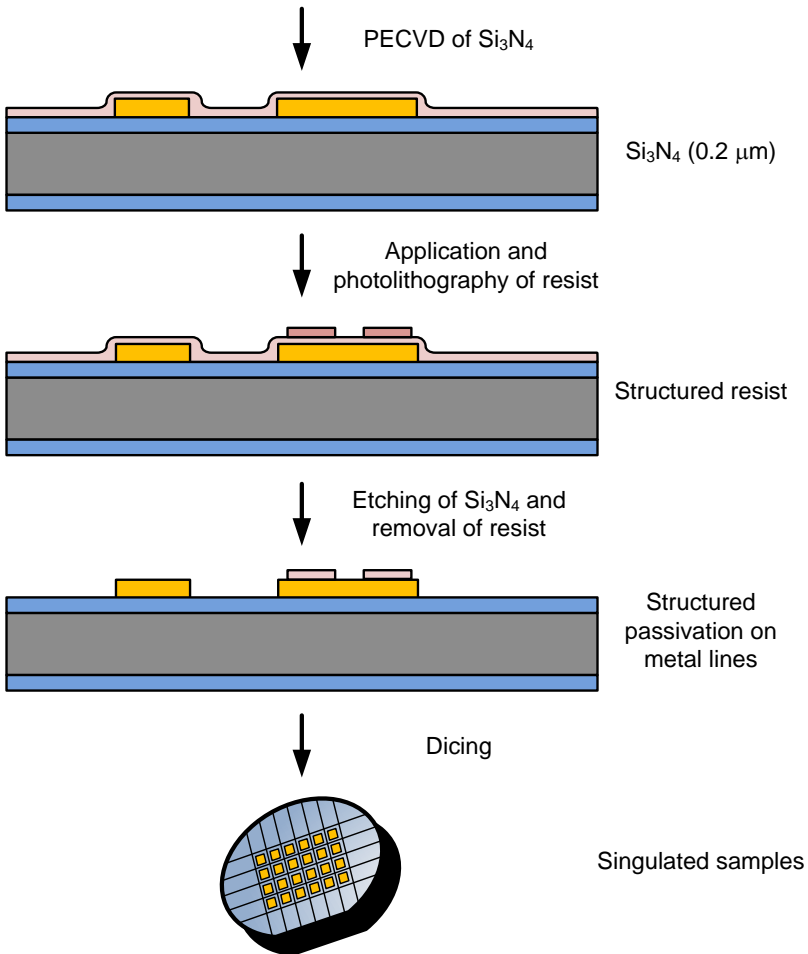


Figure 2.4: Continued.

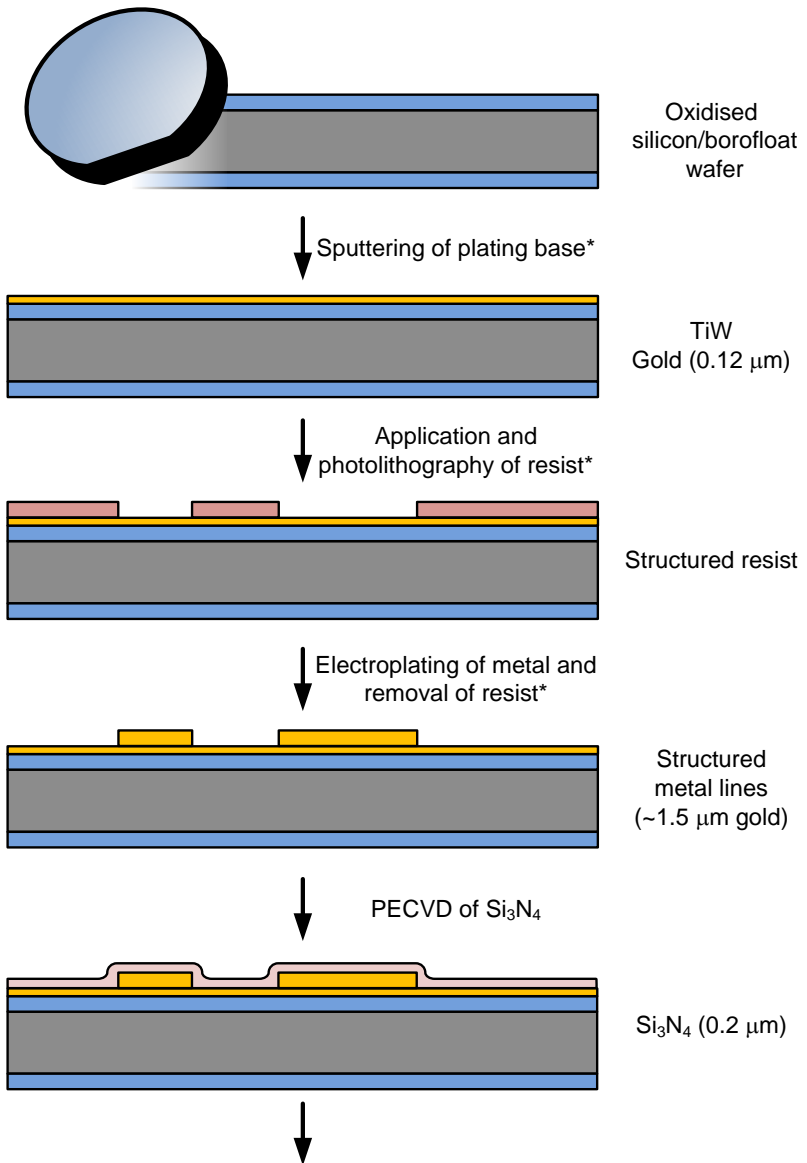


Figure 2.5: Process flow of second type devices for solder bump assembly.

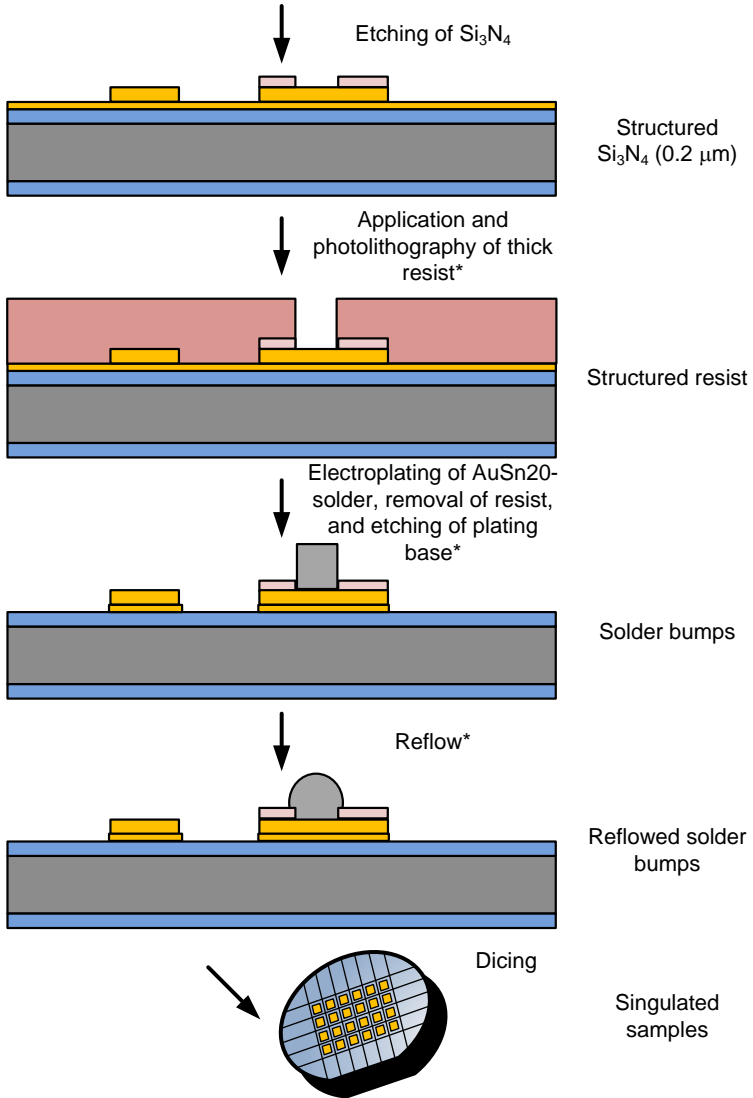


Figure 2.5: Continued.

2.3 Measurement method and setup

The characterisation scheme is illustrated in figure 2.6. Each step is discussed below.

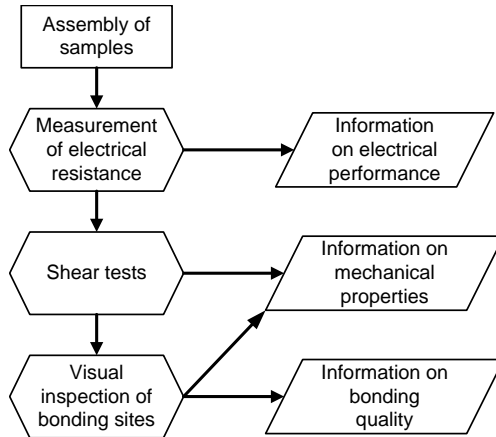


Figure 2.6: Flow diagram for the characterisation scheme.

Measurement of electrical resistance

Resistance measurements of small interconnects require an accurate measurement unit and a dedicated setup. A Keithley 2750 Multimeter with an input impedance of $10\text{ M}\Omega$ was used. Usually, a so-called 4-point or 4-wire configuration is set up in order to measure low resistances (see figure 2.7). A current is driven through the resistance R_{Bump} which has to be measured. In a 2-point configuration the voltage drop across the measurement unit would be measured. The ratio *voltage drop/current* is identified as the resistance in question (assuming ohmic behaviour of all components). But the voltage drop along the wires and across the contacts between wires and device is included in the measurement. Hence, the calculated resistance value is too high. In a 4-wire configuration the contribution of the wires and the contacts can be avoided. This is achieved by employing a second circuit for measuring the voltage drop (solid blue lines in figure 2.7). Ideally, there is no current going through the voltage measurement unit. As a consequence, there is no voltage drop along the blue wires and the contacts. The measured resistance comprises the resistance of the investigated element (R_{Element}) and the resistances (R_{Lines}) of the lines between contacts and element. Since

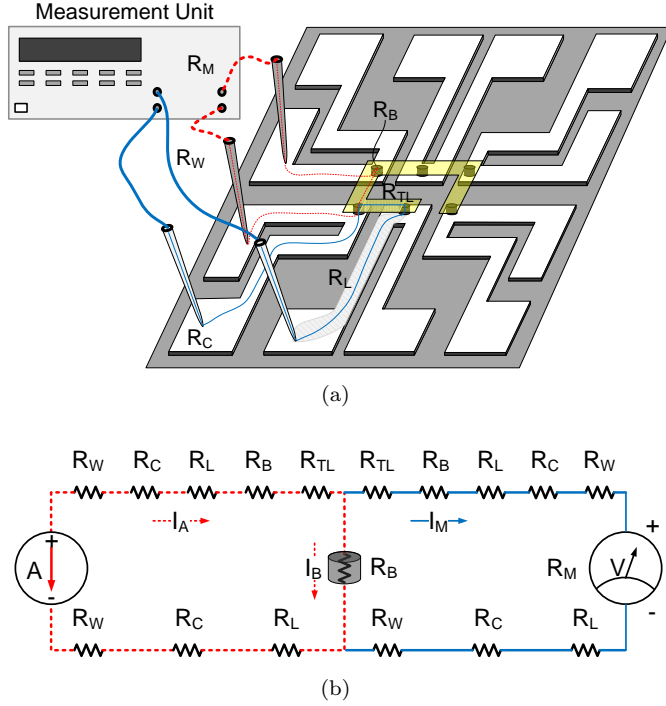


Figure 2.8: 4-Point measurement principle. The contributing resistances (a) and the circuit schematic (b) are illustrated. The dashed red lines depict the electrical circuit providing the driving current, whereas the solid blue lines depict the voltage-measurement circuit.

$$R_B = -\frac{U_B}{I_B}. \quad (2.2)$$

The minus sign stems from the fact that the voltage U_B has the opposite sign than U_M , according to Kirchhoff's voltage law. Estimating the contributing resistances of the setup (see table 2.1), it can be shown that R_B and R_{Measure} are related by the following approximation (see appendix A):

$$R_B \simeq R_{\text{Measure}} \cdot (1 + 4 \cdot 10^{-7}). \quad (2.3)$$

The error induced by the measurement setup is therefore negligible. The uncertainty of the measurement is given by the accuracy of the measure-

ment unit.

- R_W : Connection wires $\sim 1 \Omega$
- R_C : Probe-to-metal-line contact $\sim 1 \Omega$
- R_L : Bottom substrate metal line $\sim 100 \text{ m}\Omega$
- R_{TL} : Top die metal line $\sim 20 \text{ m}\Omega$
- R_B : Interconnect bump $\sim 10 \text{ m}\Omega$
- R_M : Measurement unit $\sim 10 \text{ M}\Omega$

Table 2.1: Relevant resistances in the 4-point setup depicted in figure 2.8.

Shear test and visual inspection

The dies were sheared with the dage series 4000 shear tester with a shear tool which is wider than the chip. The employed shear parameters are listed in figure 2.9. The shear speed is held constant during the test, while the force is steadily increased in order to keep the shear speed at the preset value. The applied shear force is measured as a function of time. When the assembly breaks (eg. joints, silicon chip, metallisation) the force falls back and the shear test is stopped. The maximum measured force is called '*force at break*'.

The sheared dies are inspected under a microscope. Information is gained on the failure mechanism (eg. joints, silicon chip, metallisation) and, for instance, on the wetting of the bond pads in the solder process, the adhesion of the stud bumps in the thermocompression process, and the adhesion of the ACA/non-conductive adhesive.

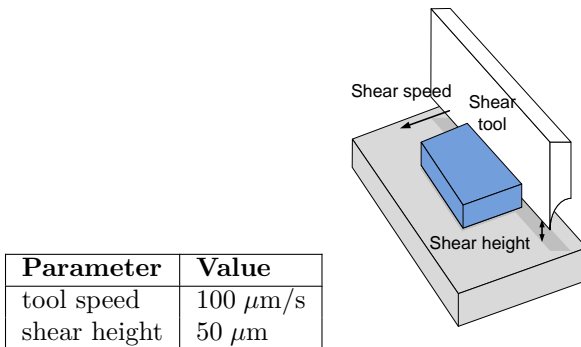


Figure 2.9: Shear test parameters and test setup.

2.4 Bonding procedures

In the following subsections, each investigated bonding procedure is described in detail. All assembly steps were carried out with the flip chip bonder FC150 from SET. Arm (chip holder) and chuck (substrate holder) can be independently heated and cooled. The chuck provides movement and rotation of the substrate in the horizontal plane. The arm provides rotation of the chip around two axes out of the horizontal plane. These five coordinates allow precise in-plane alignment and control of the coplanarity of chip and substrate. Coplanarity is especially important in ACA processes and stud bump assemblies with non-conductive adhesives. A tilt between chip and substrate will prevent certain stud bumps from contacting the opposing pads. Bonding forces and temperatures in the ACA process are usually not high enough to compensate tilts by compressing stud bumps. Thermocompression processes, where gold studs are bonded to the opposing pads by applying high forces and temperatures, are less delicate. However, a tilt may prevent an equal distribution of the applied force to the stud bumps. This may cause reliability problems because the pressure (acting on a single bump) cannot be controlled [7].

2.4.1 Flip chip bonding with eutectic AuSn20 solder

The binary alloy phase diagram of Au and Sn shows a eutectic point at 278 °C and 20 weight% Sn [18, 19]. It consists of the so-called ζ' -phase Au_5Sn with a Sn concentration of 16.7 at% Sn³ ($\hat{=}$ 10.76 wt% Sn) and the AuSn-phase with 50 at% Sn ($\hat{=}$ 37.6 wt% Sn). The weight fractions $W_{\text{Au}_5\text{Sn}}$ and W_{AuSn} of the two phases in the eutectic can also be calculated from the phase diagram by applying the following equation [19]:

$$W_{\text{Au}_5\text{Sn}} = \frac{C_{\text{AuSn}} - C_{\text{AuSn20}}}{C_{\text{AuSn}} - C_{\text{Au}_5\text{Sn}}}. \quad (2.4)$$

The concentrations $C_{\text{Au}_5\text{Sn}}$ and C_{AuSn} need to be specified in terms of only one constituent (Sn or Au). With the cited values for wt% Sn we find the weight fractions $W_{\text{Au}_5\text{Sn}}$ and W_{AuSn} of the eutectic AuSn20 solder:

$$W_{\text{Au}_5\text{Sn}} = 65.6 \%, \quad (2.5)$$

$$W_{\text{AuSn}} = 34.4 \%. \quad (2.6)$$

³ at% = atomic percent

The Au-Sn alloy with this composition (hereafter called AuSn20) is the most often used solder in the field of optoelectronic packaging. It allows fluxless and Pb-free soldering of Au pads at relatively high temperatures. It provides a hard bond and shows no creep. Fluxless soldering is not only important in optoelectronics. Residues of the flux may affect the performance of optical components as well as micromechanical components. For example, residues on the facette of a laser die will attenuate the transmitted energy and hence heat locally the laser die and reduce the output power and quality of the laser beam. Residues on micromechanical components such as diaphragm based pressure sensors may alter the elastic properties of the membrane.

As mentioned above, the AuSn20 solder shows no creep. However, Pb containing solder joints which are under elevated temperature loads and static mechanical stresses show time-dependent and permanent deformation. Empirically, it is found that creep occurs at temperatures above $0.4 \cdot T_M$ (T_M = absolute melting temperature), but below the plastic deformation region. Soldered laser dies may fail after a certain time because creep may change the laser beam path.

In the here presented experiments, the solder bumps are on the substrate (see figure 2.2 in section 2.2). Figure 2.10 shows a micrograph⁴ made with a scanning electron microscope (SEM). The Si_3Ni_4 passivation layer around the solder bumps is clearly visible. The solder is electrodeposited in circular holes with $80 \mu\text{m}$ in diameter. In the subsequent reflow process, the solder forms a $40 \mu\text{m}$ high half-sphere, protruding over the Si_3Ni_4 opening. Figure 2.11 shows a magnified view of a solder bump. The typical texture of AuSn20 can be seen.

Figure 2.12 shows the developed bonding process with solder bumps, carried out in atmosphere. First, chip and substrate are aligned in the flip chip bonder FC150. Then the parts are assembled. A temperature profile is run while applying a constant force of 20 g. The temperature of the preheated parts is raised from $150 \text{ }^\circ\text{C}$ to $320 \text{ }^\circ\text{C}$ in 20 seconds. The temperature was held for 10 seconds before the parts were cooled by a nitrogen flow below melting point. The parts were preheated for convenience because it is time and nitrogen consuming if the flip chip bonder has to be cooled down to room temperature between two assemblies.

The here presented bonding parameters are nominal values. Regarding the temperature, there is always a difference between programmed temperature and temperature of the parts, which becomes bigger, the

⁴SEM micrographs shown in this thesis were taken in collaboration with M. Dadras from CSEM Neuchâtel.

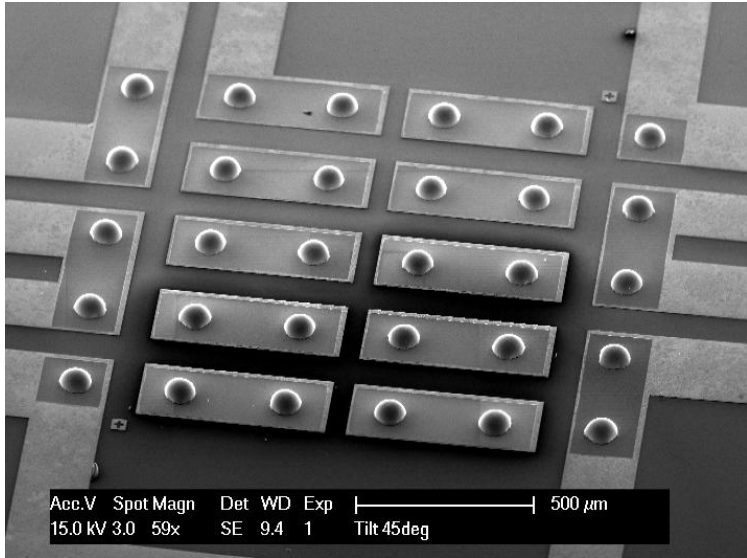


Figure 2.10: SEM micrograph of an array of AuSn20 solder bumps.

steeper the temperature ramp. It turned out that the FC150 could not hold the force at a constant value of 20 g, which is the lower limit of the FC150 according to the specifications.

It was not the scope to find an optimal true bonding temperature, force, or time, but to find an easily applicable, short, and repeatable bonding process. This was achieved with the above presented bonding process carried out in atmosphere with the flip chip bonder FC150. The bonding parameters are listed in table 2.2.

Alternatively, the FC150 offers an option for controlling the distance between chip and substrate. At the beginning of the bonding process, a reference (zero distance) is measured by physically contacting the solder bumps and the chip pads. When the solder becomes liquid, a negative value of distance guarantees a slight squeezing of the solder. The required force is automatically regulated by the flip chip bonder.

Figures 2.13(a) and 2.13(b) show SEM micrographs of polished cross sections through reflowed and soldered bumps. Figure (a) shows a reflowed bump (as-received). Three different phases can be distinguished in vertical direction. At the bottom, a socket of pure Au of $12\ \mu\text{m}$ thickness is visible, followed by a dendritic-shaped Au_5Sn phase and the AuSn20 eutectic solder. The intermetallic phase Au_5Sn originates

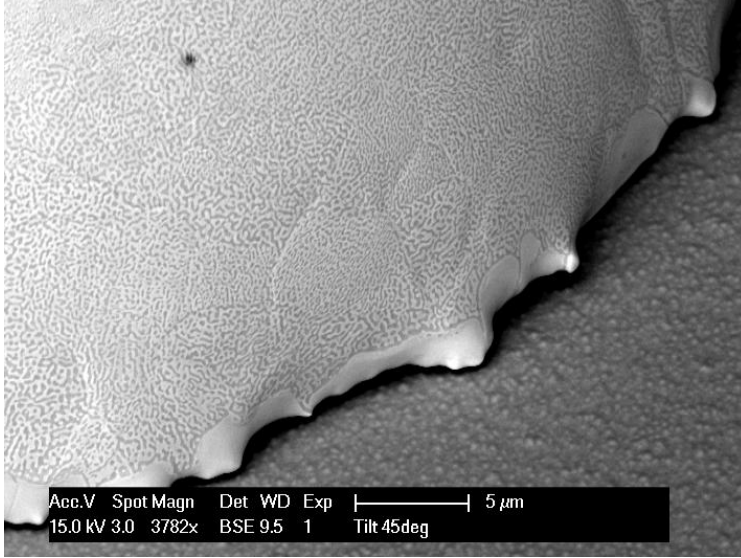


Figure 2.11: SEM micrograph of a portion of a solder bump. The typical texture of eutectic AuSn20 solder can be seen.

Eutectic AuSn20 solder	
Ramp up	in 20 seconds from 150 °C to 320 °C
Hold time	10 seconds
N ₂ cooling	15 seconds (below melting point)

Table 2.2: Parameters for bonding with eutectic AuSn20 solder developed in the thesis.

already after electrodeposition of the layers and appears at the boundary of the Au and Sn layers [20]. The contrast between ζ' and pure Au is low, because the ζ' -phase is Au-rich. The brightness of back-scattering-electron micrographs (BSE) increases with the mass of the atoms. Au₅Sn consists of 89.24 wt% Au, which makes it difficult to distinguish from pure Au. However, it is noticeable that polishing artefacts like scratches and breakouts are more pronounced in the Au-phase, which, we believe, is due to a difference in the hardness of the two phases.

Figure 2.13(b) is a micrograph of a cross section through a soldered bump. The chip electrode is visible above the solder bump. A comparison of the two figures reveals that the solder composition has changed

in the vicinity of the chip pad. It is due to diffusion of Au from the chip metallisation into the solder. This area becomes more Au-rich than the eutectic AuSn20-phase. A change in composition is therefore an evidence for wetting, because diffusion can only take place if the liquid solder is in close contact with the chip metallisation.

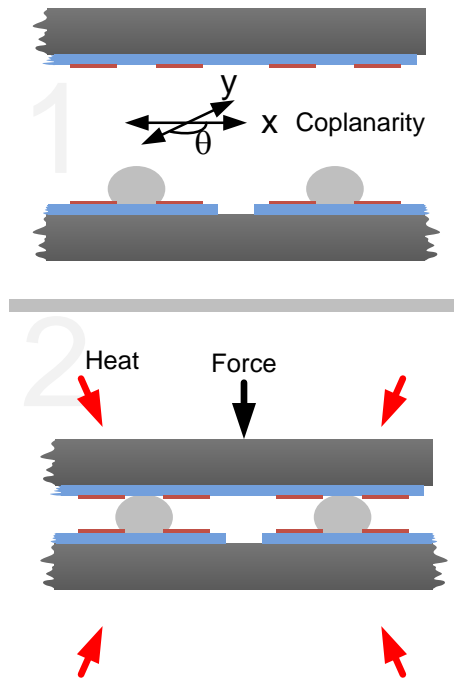
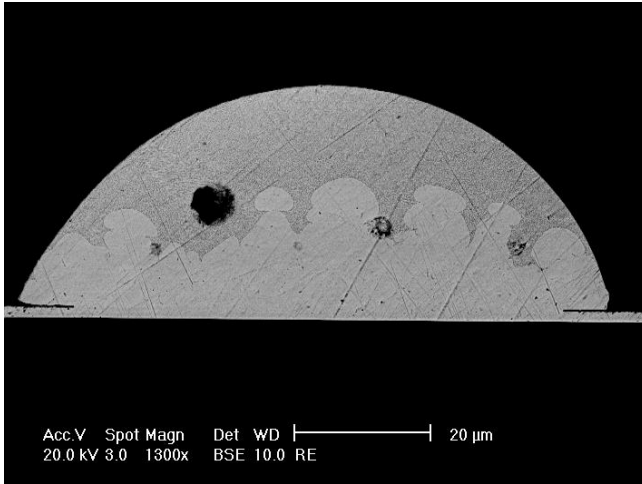
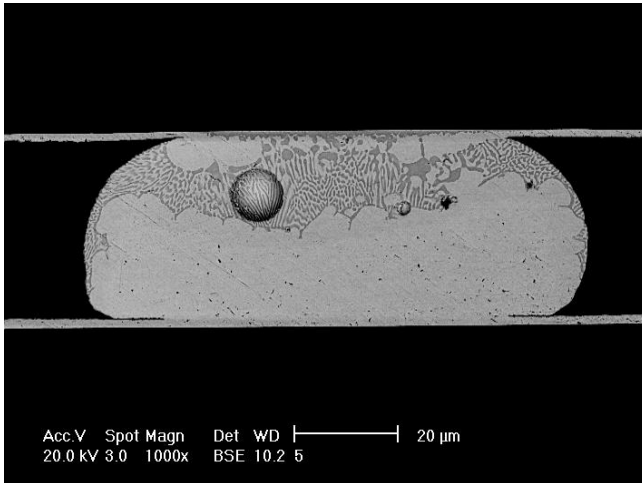


Figure 2.12: Process steps for bonding with eutectic AuSn20 solder: Chip and substrate have to be aligned (1). Then they are bonded by increasing the temperature above the melting point of the solder and by applying moderate force (2). The force supports wetting of the chip pads.



(a) Reflowed bump.



(b) Soldered bump.

Figure 2.13: Cross sections of a reflowed and soldered a bump. The reflowed bump (a) consists of three phases. At the bottom, a $12\ \mu\text{m}$ thick socket of pure Au is left, followed by the intermetallic Au_5Sn phase with its dendritic shape. On top, the eutectic AuSn_{20} phase with its typical tiger skin structure is forming a half-sphere. In (b) the bump is soldered to the chip (top). The composition of the alloy changed in the vicinity of the chip metallisation due to Au diffusion.

2.4.2 Thermocompression bonding with gold studs

Thermocompression bonding can be considered as a pressure welding process. Heat and pressure promote diffusion from the gold pad into the gold stud and vice versa by bringing gold stud and gold pad in close vicinity and by increasing the diffusion rate. Applied pressures and temperatures are the highest of the investigated bonding techniques. This limits the variety of applications especially when delicate devices have to be bonded. Chips can break during the bonding process or malfunction after bonding if they do not sustain the applied pressures and temperatures. MEMS devices could be rendered useless from induced stresses either by applied forces or by stresses induced by a mismatch of coefficients of thermal expansion during cooling. The advantages are obvious: Stud bumps can be placed by widely used wire bonders. Stud bumps are placed directly on aluminum pads. A whole wafer fab accommodating equipment for solder bumping becomes unnecessary: No under-bump metallisation (UBM) is required. Hence, cleaning of the aluminum pads (e.g. Ar-sputtering), sputtering/evaporation or plating of additional metal layers as well as structuring of these layers (including spin coating and photolithography of resist, etching of metals, and removal of resist) are not necessary. Furthermore, no plating bath or other equipment for solder bumping is required. Costs for a dedicated oven with control of atmosphere for a complex reflow process are saved.

Because stud bumping can be done on off-the-shelf chips without UBM processes, it is a flexible and cheap process. Manual wire bonders are low-cost. They are ideal for process development and prototyping, because single dies can be bumped. Fully automated high speed stud bumpers can bump a whole wafer in minutes. Thermocompression bonding or other bonding methods including stud bumps (e.g. ACA bonding) become a fast and flexible alternative to flip chip bonding with solder bumps.

Stud bumping allows flip chip bonding with pitches below $100\ \mu\text{m}$. The gold studs provide a compliant connection between chip and substrate, which is due to the softness of pure gold. This compliant connection can even render underfillers unnecessary. On the other hand, such a gold stud bond without underfiller is weak and needs protection from the environment.

In figure 2.14 an array of bumped gold studs can be seen. Some of them exhibit a longer tail, which is only a problem for fine-pitch applications: During bonding process the long tails are pressed down, potentially bridging two neighbouring contacts. Figure 2.15 is a magnified

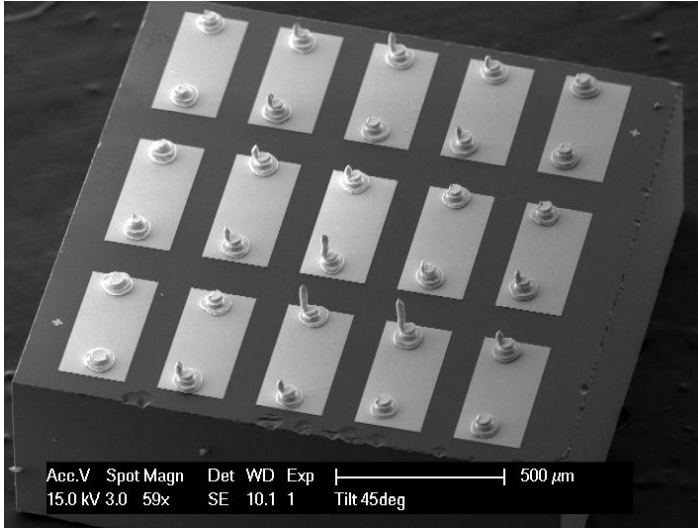


Figure 2.14: SEM micrograph of an array of stud bumps.

SEM micrograph of a stud bump with an optimal tail.

Figure 2.16 depicts the bonding process both for thermocompression with stud bumps (branch a) and for bonding with non-conductive adhesive and stud bumps (branch b). The second process is precisely spoken not a thermocompression process (because gold stud and pad are not welded). It is presented here because the electrical contact is established by a physical contact of stud bump and chip pad, in contrast to the ACA bonding process, where the electrical contact is established by conductive particles which are clamped between the *planarised* gold studs and the gold pads.

First, the gold studs are placed with the manual thermosonic wire bonder *Hybond 16* from TPT. A $25\ \mu\text{m}$ thick gold wire was utilised. In order to get stud tails with uniform lengths, the bump placement is followed by a vertical movement and a horizontal movement of the wire bonder capillary. Then the capillary moves down again to cut off the wire by squeezing the tail between capillary edge and bump.

Apart from the dispensing step (2b), the process steps for thermocompression and bonding with non-conductive adhesive are identical. Chip and substrate have to be aligned in the flip chip bonder FC150. Coplanarity of the two parts is more critical in the assembly step with non-conductive adhesive, because applied forces and temperatures are

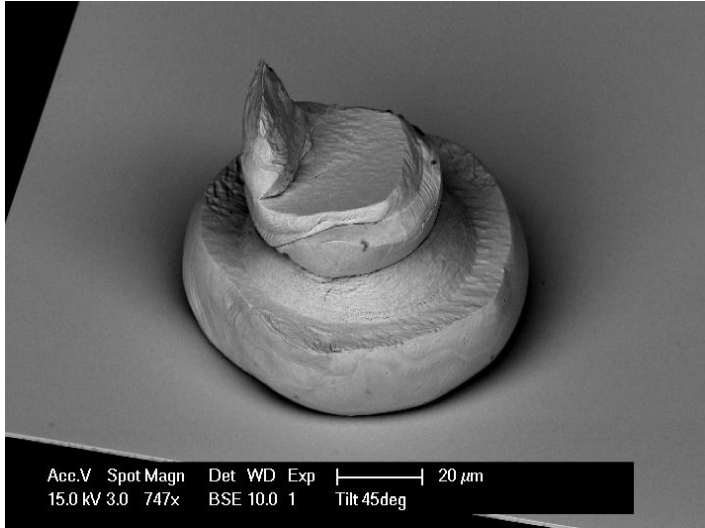


Figure 2.15: Magnified view of a stud bump.

not high enough to compensate tilts by squeezing stud bumps. It is therefore crucial to use gold studs as-bumped. The small tail allows small compensations. After alignment the chip is pressed on the substrate. The bonding parameters are listed in table 2.3.

Thermocompression	
Ramp up	in 25 seconds from 100 °C to 350 °C
Hold time	20 seconds
N_2 cooling	15 seconds
Force	60 g/bump
N_2 cooling	15 seconds
Bonding with non-conductive adhesive	
Ramp up	in 30 seconds from 25 °C to 260 °C
Hold time	10 seconds
N_2 cooling	15 seconds
Force	60 g/bump
Adhesive	Hysol FP5001, epoxy-based

Table 2.3: Bonding parameters for thermocompression developed in the thesis.

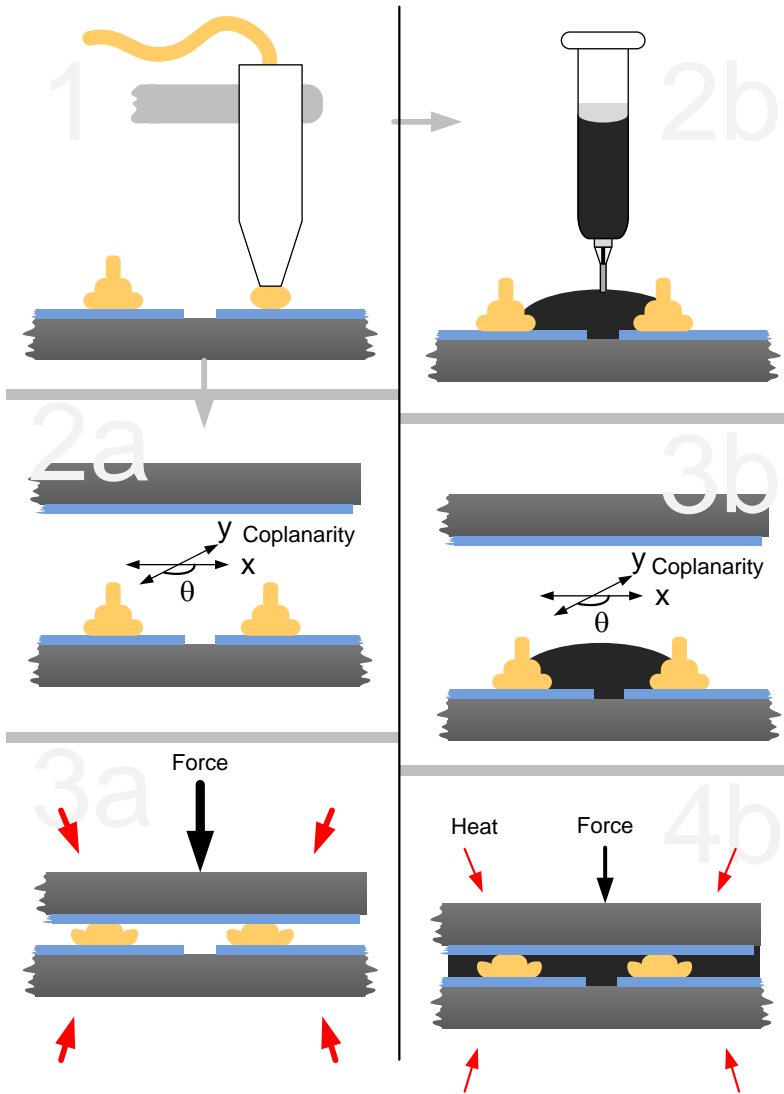


Figure 2.16: Process steps for thermocompression with gold studs. Branch a (left) depicts the standard thermocompression process. The alignment step (2a) is followed by the thermocompression process (3a). Bonding with non-conductive adhesive (branch b) first requires a dispensing step (2b). Then chip and substrate are aligned (3b) and bonded (4b).

2.4.3 Flip chip bonding with anisotropic conductive adhesives (ACA)

Even though ACA bonding is not as established as solder bumps there exists a variety of anisotropic conductive adhesives. Basically, the ACA consists of an adhesive (matrix) and conductive particles dispersed in the matrix. The matrix can either be a paste (ACA) or a film (ACF). Pastes can be dispensed, stamped, or screen printed. Films are laminated to the substrate prior to the bonding process. The matrix can be a thermoset or thermoplastic polymer. Elastomers are -to our knowledge- not practical. The cured ACA has to maintain a compressive force on the particles between gold stud and pad. These particles provide an electrical contact in vertical direction (from chip pad to substrate pad). But the ACA acts as isolator in the horizontal plane because the particle density is much lower than in isotropically conductive adhesives.

There exist varieties of conductive particles. They are available in different sizes and compositions. Most wide-spread are metal spheres and plastic spheres with a metal coating. An example are metal spheres consisting of a nickel core with a gold coating. Nickel is cheap and generally harder than the gold stud. It is partially pressed into the gold stud during the bonding process, which provides a large contact surface. The gold coating protects the nickel sphere from corroding. Although the spheres are inside the matrix, it is only a question of time until moisture and corrosive chemicals reach the particles by diffusing through the matrix.

Plastic spheres are softer than the metal pads and stud bumps. The applied force will rather squeeze the particles than the metal pads. The amount of deformation strongly influences both the electrical properties and reliability [21]. The interconnect resistance decreases with increasing deformation of the particles. Obviously, the contact surface increases with increasing bonding force. Figure 2.17 is a schematic illustration of the behaviour of hard and soft conductive particles in the bonding process, as described above.

ACAs are also used in fine-pitch applications [22]. Critical parameters are particle size and density. Large particles (compared to the gap between adjacent pads) can bridge two connections. If the particle density is too high it is possible that two or more coincidentally touching particles bridge adjacent pads even though the gap is bigger than the size of one particle. There are several possibilities to minimise this risk. One way is to coat the particles with a thin dielectric layer. This layer breaks when the particle is deformed between the pads of chip and substrate and the particle becomes electrically conductive. The uncompressed par-

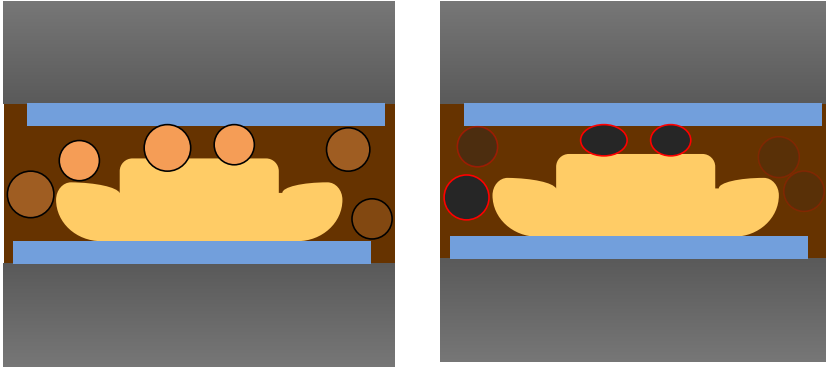


Figure 2.17: Comparison of hard (left) and soft (right) spheres. The hard spheres are pressed into the softer gold studs, whereas the soft particles deform under pressure.

ticles are isolating. Coincidentally touching particles cannot bridge two adjacent contacts, as described in [23]. Another way to formulate ACA for use in very fine-pitch interconnections (down to $40\ \mu\text{m}$) is to array the conductive particles in the matrix. This is either achieved by an anisotropic magnetic field [24] or by a special production process [25]: The metal particles are formed on a metal sheet by electroplating the metal in a photolithographically patterned resin. Then the resin is dissolved and the adhesive is formed on the sheet. Finally, the adhesive film is peeled off together with the metal particles.

In contrast to thermocompression, ACA bonding requires flat bumps with uniform heights. This was achieved by pressing the dies against a very flat and stiff ceramic plate. There are two possibilities to produce flat bumps. One way is to control the applied pressure (force/bump). Well defined weights are placed on the ceramic plate which squeezes the bumps. If the ceramic plate is stiff enough, many chips can be flattened simultaneously. Another way is to control the final bump height with interposers. These can be metallic sheets with a well defined thickness. The height is controlled by placing unbumped dies next to the bumped dies in the flattening process. Metallic sheets of $25\ \mu\text{m}$ height are placed on the unbumped dies. When the bumps are squeezed down to $25\ \mu\text{m}$, the pressure drastically decreases because the applied force is no longer acting only on the bumps, but also on the metallic sheets. Provided that the surface of the interposers is big enough, the final height of the bumps can be precisely controlled. Figure 2.18 shows an array of

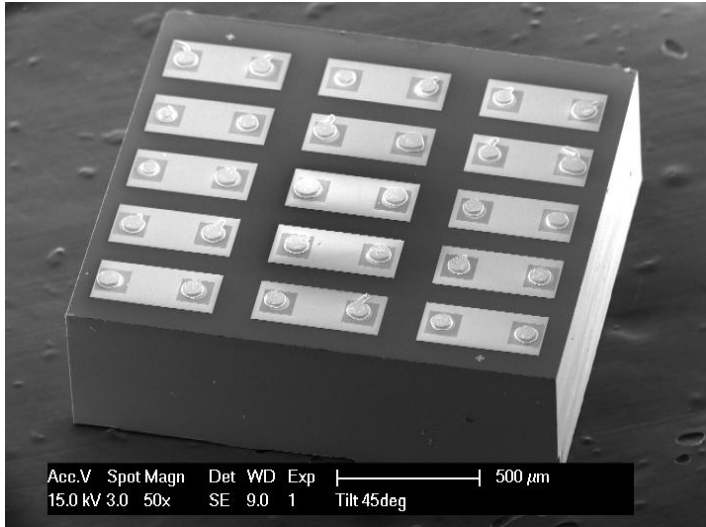


Figure 2.18: SEM micrograph of an array of flattened stud bumps. The final bump height was controlled by metallic sheets with a thickness of 25 μm .

flattened bumps where the bump height was controlled with interposers. Figure 2.19 is a close-up of a single flattened bump. The stud bumps were placed in the openings of the Si_3Ni_4 layer. It can also be seen that the tail is pushed aside. Well controlled and short tails are required in fine-pitch applications with pitches below 100 μm .

Figure 2.20 depicts the ACA-bonding process. It is similar to the bonding process with non-conductive adhesive apart from the flattening of the stud bumps. The advantage over other bonding processes is the small bonding force. 5 g–10 g per bump is sufficient. Such small forces are not strong enough to squeeze unflattened bumps in the bonding process. Reliable contacts with small and uniform electrical resistances are thus only achieved with flattened bumps. After stud bumping and flattening (1–3 in figure 2.20), the ACA is dispensed (4), chip and substrate are aligned (5) and bonded (6). The bonding parameters are listed in table 2.4.

The average particle size of the Hysol FP5300, a typical ACA, is 7 μm . The maximum particle size is 12 μm . Due to the variation in size, a certain bonding force has to be applied in order to get an acceptable electrical resistance across the connection. If the force is too small, the larger bumps define the gap between the bond pads. Smaller bumps do

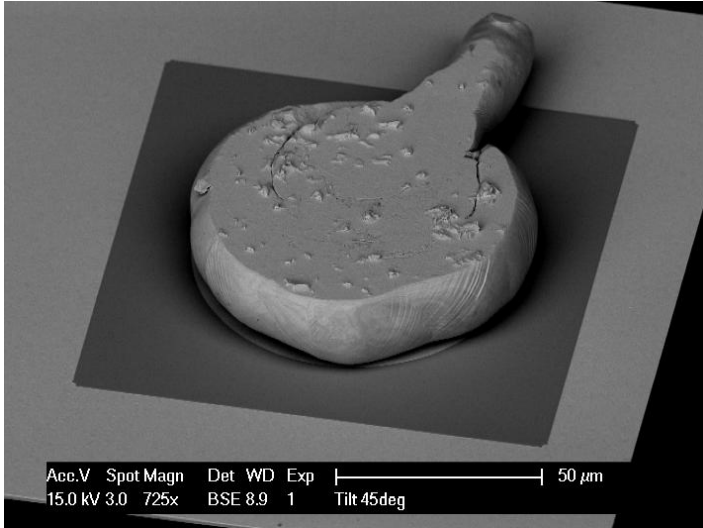


Figure 2.19: SEM micrograph of a flattened stud bump. The tail is pushed aside. Remaining tails after stud bumping can cause short circuits in fine-pitch applications.

ACA bonding	
Ramp up chip	in 15 seconds from 80 °C to 180 °C
Ramp up substrate	in 15 seconds from 50 °C to 180 °C
Hold time	12 seconds
N ₂ cooling	no active cooling
Force	10 g/bump
Adhesive	Hysol FP5300; epoxy matrix with Au-coated Ni particles with an average size of 7 μm

Table 2.4: Bonding parameters for ACA bonding developed in the thesis. Chip and substrate have different starting temperatures. The starting temperature of the substrate must not be too high to prevent early curing of the ACA.

not contribute to the conductance of the contact.

The photograph in figure 2.21 shows a cross section through an ACA interconnect. Such a cross section photograph can be misleading in two ways: The nickle particles seem to strongly vary in size. Such a conclusion is not necessarily correct because the particles are cut at random depths.

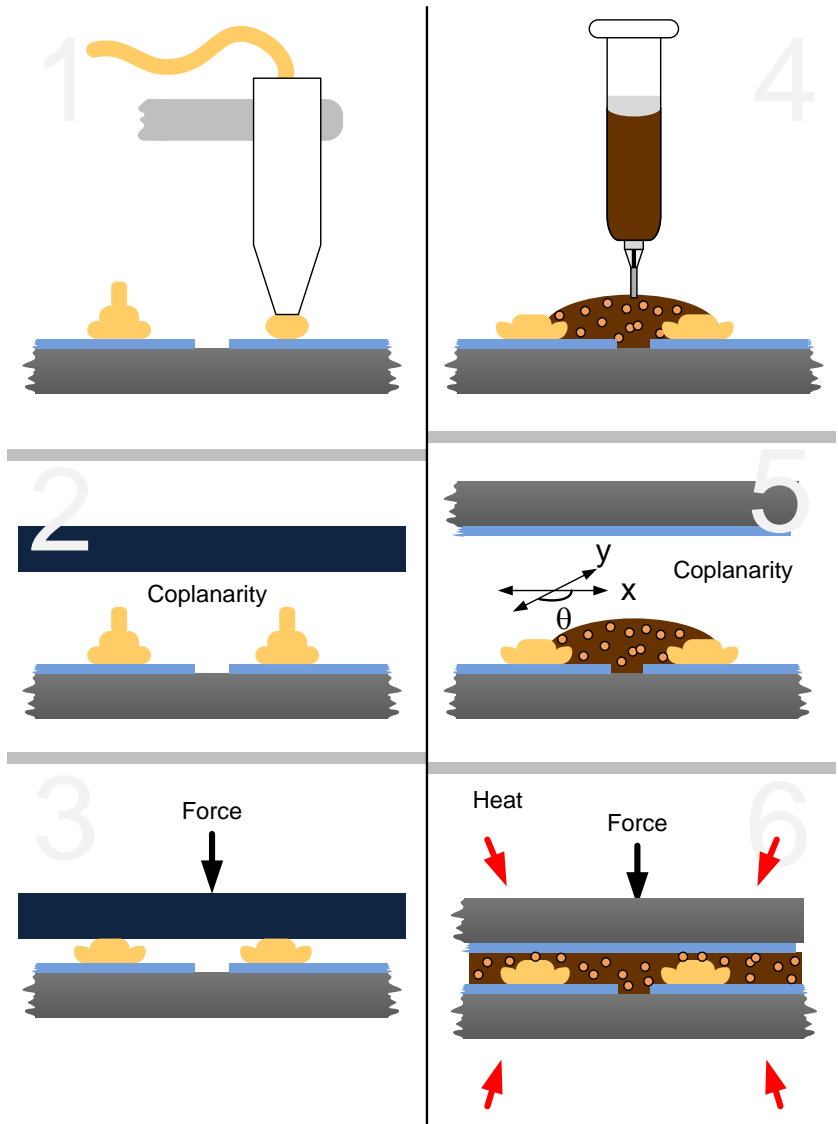


Figure 2.20: Process steps for ACA bonding. Gold studs are placed with a commercial wire bonder and flattened (1-3). Dispensing of the ACA (4), alignment of chip and substrate (5), and bonding (6) is carried out with the flip chip bonder FC150.

The random distribution of the particles is also the reason why only one particle is visible between the bond pads. No information is gained about the number of particles between the bond pads. If one wants to gain information about the average number of particles and its influence on the electrical resistance, transparent electrodes can be employed, as it is done in [25].

Valuable information is gained about the gap between the gold stud and chip pad. As explained above, the advantage of ACA is a low bonding force. If the cross section revealed that the gap between chip pad and gold stud is much thinner than the average particle size, the bonding force could be reduced. The bonding force in figure 2.21 was 50 g/bump. The resulting gap is $2.5 \mu\text{m}$. The particle is deeply pressed into the gold stud.

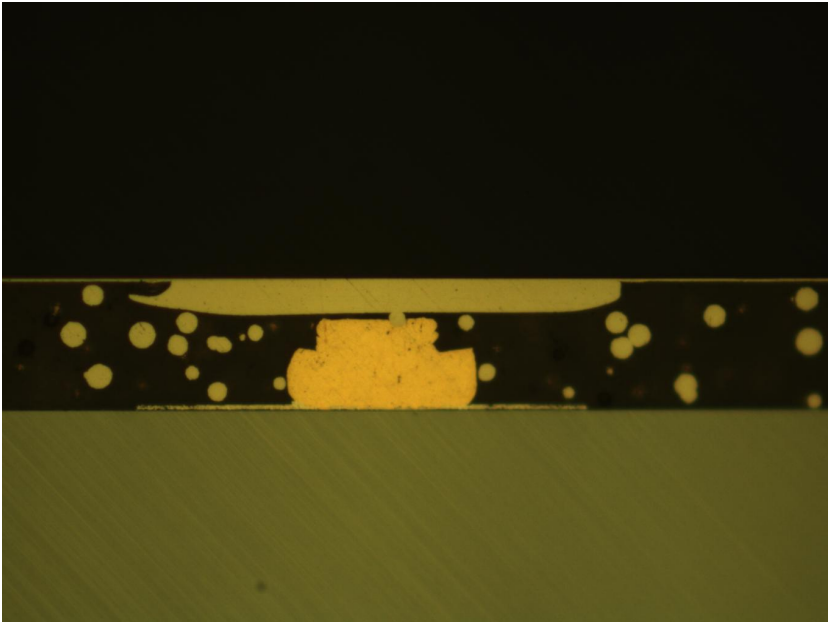


Figure 2.21: Photograph of a cross section through an ACA contact. The particle is partially pressed into the gold stud. The top electrode is a $10 \mu\text{m}$ thick electroplated nickel bump.

2.5 Results and discussion

For each flip chip bonding procedure at least eight devices with 6 (of which 4 can be measured) bumps were assembled. 10 devices were assembled with ACA. Each bump was measured as described in section 2.3. The values are graphically presented in figure 2.22. One column is the averaged resistance value of one bonding site for a specific bonding procedure. The values were not averaged over all bonding sites because site three shows a significantly lower contact resistance than the other sites. We believe it is related to the design of the metal lines on substrate and chip. Even though a 4-point measurement was done, the resistance of site three is by a factor of 2 lower than the resistances of the other three sites.

The metal structure and the measurement geometry most probably influence the measurement, as depicted in figure 2.23. In the upper drawing the electrical current flows through the right side of the top electrode, down the bump, and through the bottom electrode on the right side. In the bottom drawing the current flows through the bottom electrode on the left side. It can be seen that in the upper case the current crowds along the right edge of the bump, whereas in the lower case the current density is lower. The upper case is known to cause current crowding effects at the electrode-bump interface [76]. Current crowding

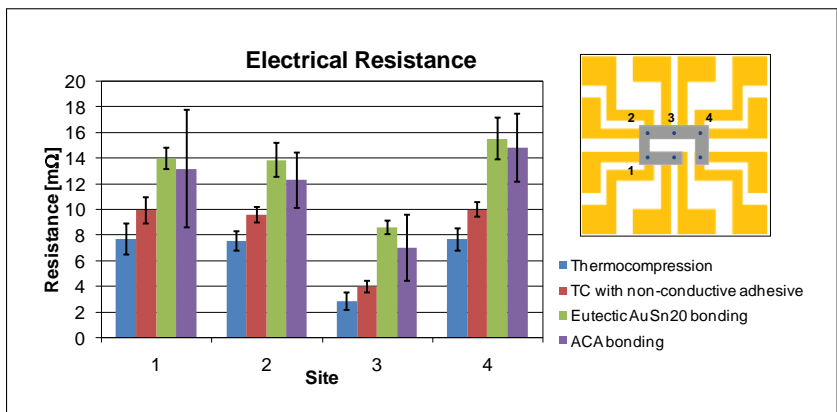


Figure 2.22: Electrical resistance for the investigated flip chip bonding processes. The averaged resistance for each site is measured and plotted with the standard deviation. Site 3 shows a significantly lower contact resistance than the other three sites.

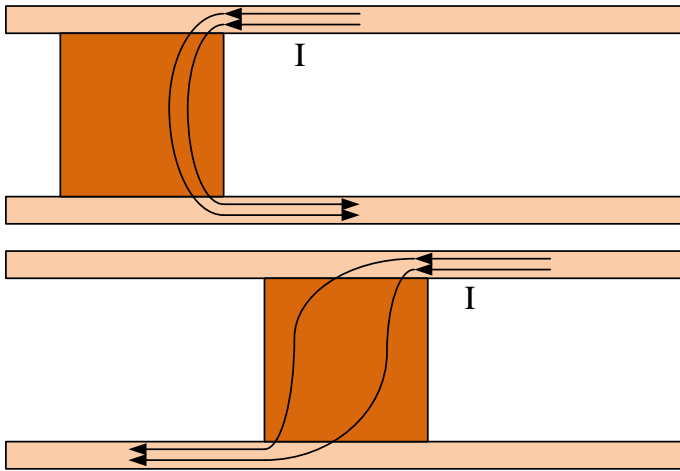


Figure 2.23: Influence of measurement geometry on measured resistance value of a flip chip interconnection.

strongly depends on the geometry of the flip chip interconnections (e.g. electrode thickness, bump geometry and microstructure). It is probably the reason for the differences of the contact resistances of the bonding sites because the current is restricted to a small portion of the cross section of the bump. According to Ohm's law, the resistance is inversely proportional to the cross-sectional area of a conductor.

It can be seen from figure 2.22 that thermocompression with gold studs provides the lowest contact resistance, and soldering with eutectic AuSn20 the highest contact resistance. But it is important to understand that the resistance values for the different flip chip bonding techniques are to be compared with care, because each bonding technique depends on many parameters. Some of them are important for all procedures, others are only crucial for a specific procedure. The important bonding parameters are listed in table 2.5 on page 39. The bonding parameters are again dependent on more basic parameters which are listed in the same table in *italic* style text.

Specifically the solder process and the processes with gold stud bumps depend on different parameters. The latter processes mainly depend on the size and mechanical properties of the gold stud. The gold stud, in turn, depends on the stud bumping parameters. The final bump height and width is crucial. The final height of the solder bumps (after bonding) is in the range of $40\ \mu\text{m}$, whereas the final height for gold studs

Eutectic AuSn20 solder
-Initial bump size
-Final bump height (and width) <i>initial bump size</i> <i>bonding force</i>
-Intermetallic phases <i>bonding temperature and time</i>
-Wetting <i>bonding force, temperature, and time</i>
Thermocompression
-Initial gold stud bump size <i>gold stud bumping process parameters and wire properties [16]</i>
-Final bump size (height and width) <i>initial gold stud bump size</i> <i>bonding force, temperature, and time</i> <i>gold wire properties</i>
-Weld quality <i>bonding force, temperature, and time</i>
Bonding with non-conductive adhesive
-Initial gold stud bump size <i>gold stud bumping process parameters and wire properties</i>
-Final bump height and width <i>initial gold stud bump size</i> <i>bonding force, temperature, and time</i> <i>gold wire properties</i> <i>properties of adhesive</i>
-Quality of mechanical contact between stud bump and chip pad <i>all before mentioned parameters</i>
ACA bonding
-Initial gold stud bump size <i>gold stud bumping process parameters and wire properties</i>
-Final bump height and width <i>initial gold stud bump size</i> <i>Force per bump in flattening process</i> <i>gold wire properties</i>
-Contact surface <i>Particle size, density, distribution in ACA, materials</i> <i>bonding force, temperature, and time</i>

Table 2.5: Most important bonding parameters for the investigated flip chip bonding procedures.

in a thermocompression process is in the range of $20\ \mu\text{m}$.

Gold studs in devices bonded with non-conductive adhesive and ACA are slightly higher, because the applied bonding parameters are moderate compared to thermocompression.

Flip chip bonding with eutectic AuSn20 solder

The higher resistance of solder bumps is also explained by the different interconnect materials. Gold studs are made of pure Au (with an electrical resistivity of $2.2 \cdot 10^{-8}\ \Omega\text{m}$). The solder bump consists of different layers of pure Au and AuSn alloys, which have a higher resistivity than pure Au. Intermetallic phases and the microstructure of the bump are well known to influence the resistance [26]. The higher value is not due to incomplete wetting, as shear tests revealed (see below).

Since the introduction of the C4 (controlled collapse chip connect) process by IBM in the early 1960, a lot of money and time was spent to investigate solder-bumped flip chip bonding. Pb containing solders are probably the best characterised and most widespread material in interconnect technology. With the transition to Pb free solder processes in electronics over the past years, research in reliability and life prediction has seen a revival. Reliability tests are again defined and carried out [17], life prediction models are set up [27, 28], and simulations are carried out [29]. The focus is now on Sn-Ag based solders like SAC305.

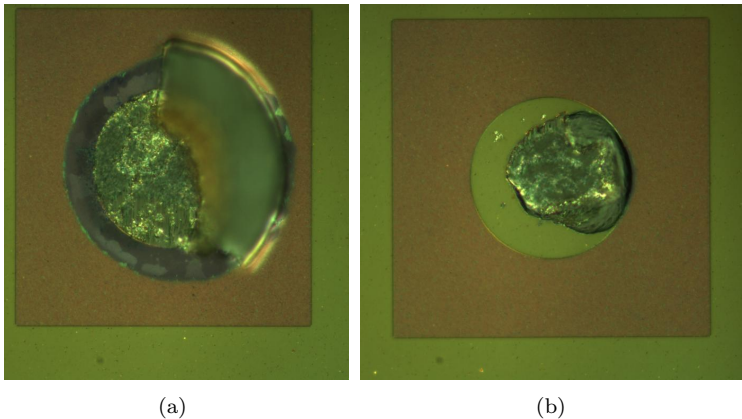


Figure 2.24: Photographs of complete (a) and partial (b) wetting on the chip side. The opening in the brownish, rectangular shaped Si₃N₄ layer defines the bond area.

AuSn solders are less frequently used. Applications are mainly found in optoelectronics [30], where the superior characteristics outweigh the higher costs.

The resistance values for the solder bump contacts presented in figure 2.22 show small variation. The standard deviation is in the range of 1 mΩ (compare the error bars). We believe that this is due to variations in the microstructure in the bump. Wetting problems may be another source of variation [31], but was ruled out by shear tests and visual inspection of all bonding sites on the chip with a reflected-light microscope. Figure 2.24 shows a completely wetted bond pad. For comparison, a bond pad which is only partially wetted is shown in 2.24(b). All eight devices (each with four bonding sites) were visually inspected. All bond pads were completely wetted.

ACA bonding

The particles of one contact are considered to be in parallel arrangement [32]. The resistance is hence inversely proportional to the number of contributing particles, provided that all spheres have identical resistances. Of course, this is only true if all spheres have the same size. If the spheres are homogeneously distributed, the number of spheres of a contact is proportional to the contact surface. Hence the contact resistance is inversely proportional to the contact surface:

$$\frac{1}{R_C} = n \cdot \frac{1}{R_s} \Leftrightarrow R_C = \frac{R_s}{n} = \frac{R_s}{\rho \cdot A} = \frac{R_s}{\rho} \cdot \frac{1}{A} =: C \cdot \frac{1}{A}. \quad (2.7)$$

R_C and R_s are the total contact resistance and the resistance of a single sphere, respectively. n is the number of spheres within the contact surface A . ρ is the average number of particles per contact surface. ρ is not necessarily the number of particles ρ_A per surface when the ACA is squeezed on the substrate (see appendix B).

Figure 2.25 shows the correlation of contact surface and contact resistance. The graph was derived as follows: The contact surfaces of six flattened stud bumps were photographed. The number of pixels of the contact surface was counted and, since the corresponding length of a pixel is known, converted into μm^2 . After bonding, the resistances of the six contacts were measured. The vertical error bars are an estimation of the accuracy of the resistance measurement. The horizontal error bars are due to the uncertainty in pixel counting.

According to equation (2.7), the resistance is inversely proportional to the contact surface. The red curve models this relation with C as the

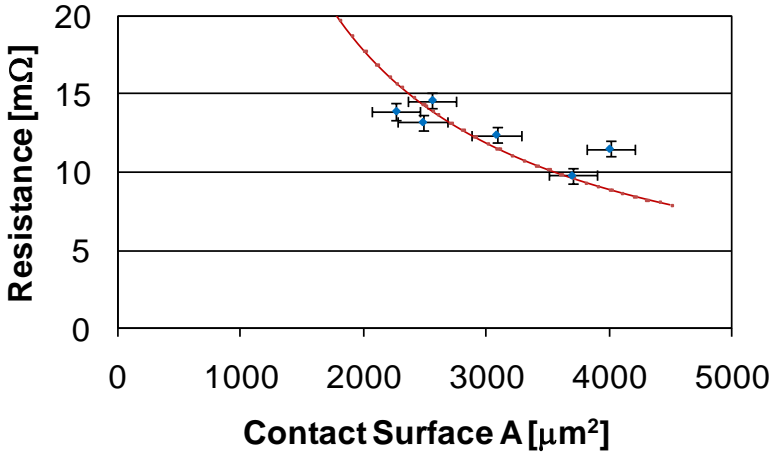


Figure 2.25: Correlation between contact surface and contact resistance in a ACA joint. The scattering implies that the spheres are inhomogeneously distributed.

fitting parameter. The data points (in blue) scatter randomly around the red curve. The strong scattering implies that the afore expressed assumptions (homogeneously distributed spheres with identical sizes) are not fulfilled. The distribution of the spheres is inhomogeneous in the range of the bump size. Figure 2.26 confirms the conclusion. Apart from variation in contact surface, the number of spheres varies strongly. Due to a random distribution of the spheres in the ACA matrix, it happens that only a few spheres provide the contact. This is the reason for the large standard deviation of contact resistances. Our investigation indicates that the average bump contact surface should not be smaller than $50 \mu\text{m}$ – $60 \mu\text{m}$ in diameter, which is the average diameter of the contact surface in the here presented experiments.

Thermocompression and bonding with non-conductive adhesive

Variations in the contact resistance of thermocompression bonded devices and devices bonded with non-conductive adhesive are in the same range as contact resistances of solder bumps. Therefore no additional discussion is needed.

The variations are attributed to the original bump size.

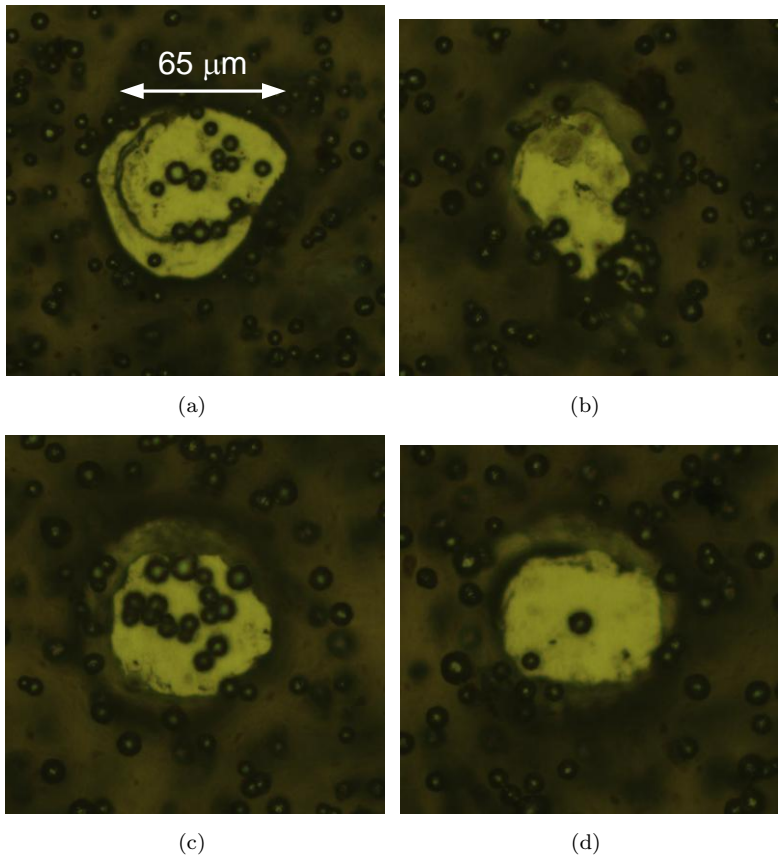


Figure 2.26: Top view on gold stud with ACA-spheres. Both the contact surface of the stud bump and the particle density vary. All photographs are taken with the same magnification.

2.6 Conclusions and outlook

In this chapter a thorough evaluation of four different flip chip bonding techniques was given. These are *flip chip bonding with eutectic AuSn20 solder*, *thermocompression bonding with gold studs*, *bonding with non-conductive adhesives*, and *flip chip bonding with ACA*.

All four investigated bonding techniques provide electrical resistances below 20 mΩ with a standard deviation in the range of 1 mΩ. Only the contact resistances in the ACA process are wider scattered, which is due

to a variation both in gold stud contact surface and particle distribution and size.

The flip chip bonding process with eutectic AuSn20 solder was carried out in air. Neither forming gas nor flux was used to promote wetting. Nevertheless, complete wetting was achieved.

The bonding processes with gold stud bumps (thermocompression and bonding with non-conductive adhesive) provide very low contact resistances. In the case of thermocompression, diffusion processes provide a welded joint. This process requires the highest temperatures and forces of all investigated bonding techniques and is therefore not an option for applications with delicate devices.

Non-conductive adhesive bonding requires lower temperatures than thermocompression but equally high forces. This is not a widespread process and only little is known about reliability and lifetime of such joints. The advantage is that no underfiller process has to be carried out. The adhesive provides electrical and mechanical contact and protection from the environment.

ACA-bonding offers the same advantages as bonding with non - conductive adhesives. Furthermore, it is the flip chip process with the lowest bonding temperature and force.

It was found that the measurement of the contact resistance in a 4-point configuration depends on which bonding site was measured (see figures 2.3 and 2.8). This variation depends on the design of the metal structures on chip and substrate. The flip chip interconnection cannot be considered as a discrete resistor element with a certain resistance.

Chapter 3 will give an introduction to state-of-the-art bonding of diaphragm -based differential pressure sensors. Chapter 4 goes beyond state-of-the-art technology by employing flip chip bonding with ACA in MEMS packaging: MEMS devices with connection pads at the peripherals and a sensitive area in the centre (e.g. diaphragm of a pressure sensor) can be flip chip bonded. The ACA is dispensed in a rectangle with an opening in the centre. In such a configuration the ACA does not only provide mechanical and electrical connection but also fluid-tight sealing of the space below the sensitive area of the MEMS device.

Chapter 5 is devoted to an application based on the development described in chapter 4.

CASE I: Pressure Strip

This novel concept of a pressure strip allows remote measurement of pressures. It provides a non-invasive and easy way of measuring flows and pressures on arbitrarily shaped aerodynamic bodies.

A flexible and thin strip comprises micro channels (left side in upper figure of 3.1), directing the pressure signal from far-off openings to the measurement unit. The measurement unit consists of an array of an arbitrary number of commercially available differential pressure sensors, transforming the pressure at the openings into voltage signals. A flexible and thin electronic board (right side in upper figure of 3.1) comprises metal lines, directing the voltage signal to far-off data processing components. The assembly configuration prevents a disturbance of the ambient air around the openings, which is crucial when air flow measurements are targeted.

Figure 3.1 shows a possible application. The flexible pressure strip can be closely attached to a wing. The pressure is detected at the top side of the wing and transmitted through the fluidic channels to the pressure measurement module at the bottom side. The far-off measurement module does not influence the top side air flow ([33], [34]).

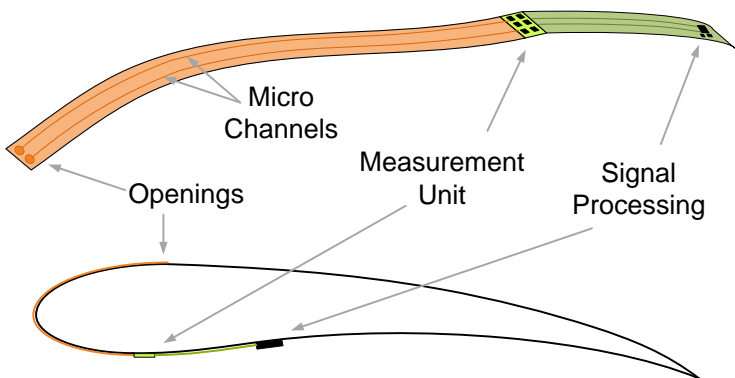


Figure 3.1: Pressure strip attached to an arbitrarily shaped wing.

3.1 Introduction

Aerodynamic pressure measurements for e.g. airplanes and cars are invasive and time-consuming due to preparation of the body (to be characterised) and the measurement setup. Today's systems employ sensor islands (i.e. transducer arrays) with a number of pressure sensors and a fluidic plug per sensor [35]. The measurement is destructive: Holes have to be drilled in the body. Tubes (attached to the holes from inside the body) connect the measurement sites with the plugs of the transducer array (see figure 3.2). Setting up such a system is time consuming and costly and on thin profiles or brittle materials it is not even an option (e.g. sails, glass). Obviously, such a measurement is carried out on bodies which do not move. These conditions are only satisfied in a controlled environment like a wind tunnel. Tests under real conditions (e.g. a flying airplane) are not possible.

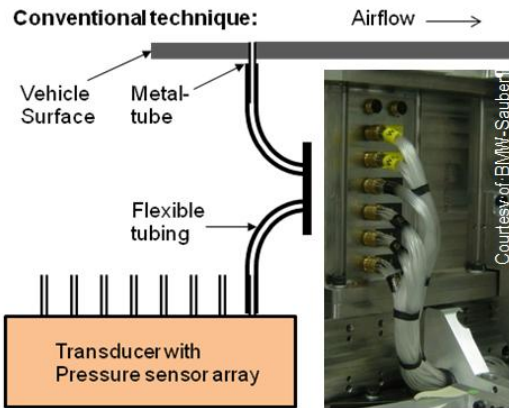


Figure 3.2: Conventional technique to measure pressure profiles.

Recently, a system was presented for non-invasive aerodynamic pressure measurement [36]. It is based on capacitive elements integrated in a structure composed of flexible polyimide and rigid FR4. The measuring elements are not remote, but located where the pressure has to be measured. Due to the size of one element, the number of measurement points per area is limited. The rigidity of the structure makes it impossible to measure the pressure distribution on strongly curved shapes.

The here presented pressure strip allows such measurements [33]. The sensors are contained in a small FR4-board which is attached to a

mechanically flexible foil. This foil, in turn, can be easily attached to arbitrarily shaped bodies. The foil contains hollow micro channels with openings to the upper side at one end and connection to the pressure sensor at the other end. The pressures at the openings are transmitted through the channels to the sensors. The flexible foil is like a skin on the body, not disturbing the air flow.

The channels and openings in the pressure strip can be as small as $50\ \mu\text{m}$. The arrangement of the measurement sites is arbitrary. Furthermore, the flexible foil smoothly adapts itself to any curved surfaces.

A higher level of integration is achieved by employing polyimide films which comprise both fluidic channels and metal structures. The metal structures may be designed to accommodate the sensors and the electrical components.

The pressure strip is an application of MEMS packaging. This chapter can be considered as an introduction to hybrid integration. It explores face-up bonding of piezoresistive differential-pressure sensors on FR4-carriers with different adhesives. Subsequent chapters deal with novel concepts of MEMS packaging: Pressure sensors are face-down bonded onto adequate carrier materials. Such a face-down bonding process is usually called *flip chip* bonding.

3.2 System design

The pressure strip can be considered as an assembly of three components (see figure 3.3): The FR4-board with the pressure sensors, the flexible strip with fluidic channels (hereafter called *fluidic strip*), and the part with the electronic components for signal processing (hereafter called *electronic strip*). This can be a flexible circuit board. Figure 3.6 is a photograph of an assembled pressure strip. The FR4-board is covered by a foil which protects the pressure sensors.

The FR4-board comprises an array of 4×4 commercially available differential pressure sensors. Each sensor is embedded in a recess in the FR4-board (figure 3.4), providing protection from the environment. The recess can be filled with a silicone gel, which keeps the moisture off the sensor and its electrical contact pads. The pressure sensors comprise a thin membrane at the top side of the sensor die which is accessible from both sides. If a pressure difference establishes between the two sides, the membrane deforms. Piezoresistive elements in the membrane transform the deflection into a voltage signal. These kind of pressure sensors are sensitive to external stresses by nature. It is therefore crucial to min-

imise the influence of the package and the impact of the environment to the sensors. Namely temperature variations and mechanical load of the package are critical. Temperature changes let the package expand or shrink. The amount of expansion/shrinkage is a material parameter (called *Coefficient of Thermal Expansion CTE*). Mismatches of CTE between two or more components in the package let the components expand differently. Hence, components which are mechanically coupled will experience stress and deformation [37, 38, 39, 40]. Mechanical loading of the package may induce stress in the pressure sensors too. The sensors have to be packaged in the way that external influences are minimised. This is described in section 3.3.

The fluidic strip is a foil of arbitrary shape. The shape and the position of the openings (where the pressure is detected) can be adapted to any body. Apart from the size of available foils and the working area of the machines for preparation of the foils, there is no limitation in shaping the fluidic strip. The positions of the openings is arbitrary. Hollow channels inside the strip connect the openings with the pressure sensors. Figure 3.5 shows a possible application: The openings in the fluidic strip are arranged in a row. If such a strip is attached to a wing in the way that the row of the openings coincides with the wing profile, than the

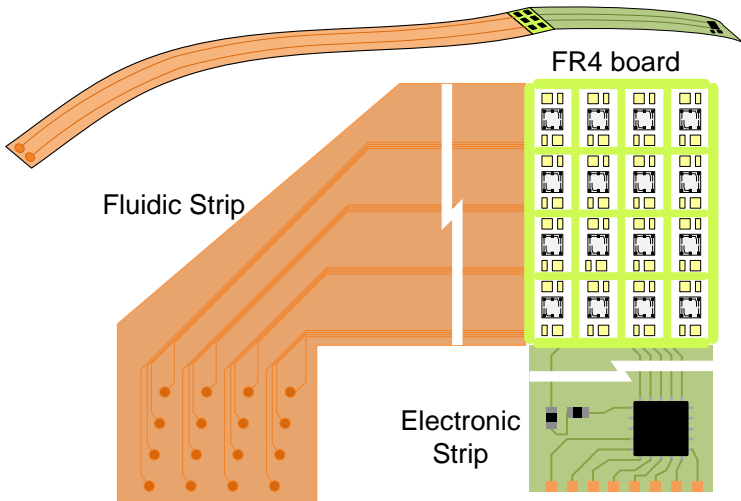


Figure 3.3: Pressure strip concept. It can be considered as an assembly of three components; the FR4-board, the fluidic strip, and the electronic strip.

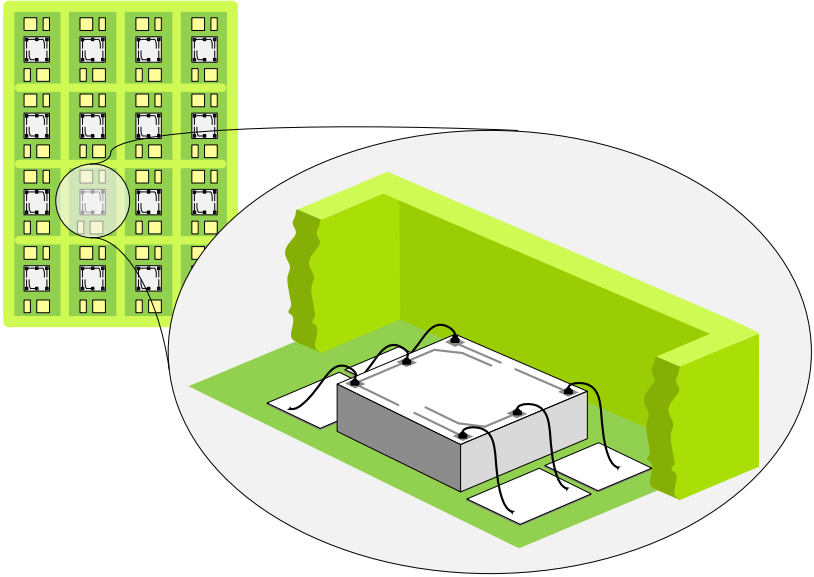


Figure 3.4: Close look at a differential pressure sensor attached to a PCB. Wire bonds provide the electrical contacts.

pressure distribution along the profile can be determined. Furthermore, the *separation point* can be detected. At this point, the laminar air flow becomes detached from the surface. Behind the separation point air flow becomes turbulent.

3.3 Bonding procedure

The pressure strip comprises an array of 4×4 differential pressure sensors attached with a silicone adhesive to a metallised FR4-board [41]. The sensors are placed in cavities, providing protection against environment. The compliant silicone is a soft mechanical connection between silicon sensor and FR4-board. Thermally induced expansion or contraction of the board and mechanical loads acting on the board are absorbed by the silicone. The differential pressure sensor has contact pads at the top surface. Gold wire bonds provide electrical contact from these pads to the board. The $25 \mu\text{m}$ thick wires do not add stiffness to the package. The sensors can be further protected by filling the cavities with a soft silicone gel (figure 3.7(a)). Through-holes in the FR4 allow connection

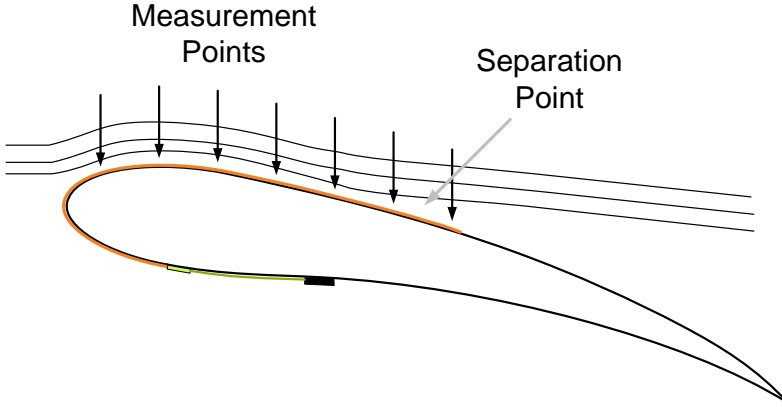


Figure 3.5: Possible application of the pressure strip. If the openings in the fluidic strip are arranged in the way that the pressure signal is detected along the wing profile, then the separation point can be easily detected.

of the sensor's back side to a flexible strip with micro channels. These channels guide the pressures from remote openings to the pressure sensors.

Preliminary simulations

Finite element simulations with the software package COMSOL were carried out to estimate the mechanical influence of the adhesive on the pressure sensor. It was the aim to obtain an understanding of the behaviour of adhesively bonded pressure sensors and the influence of the adhesive on the sensors during *temperature changes*. A temperature change lets the components shrink or expand differently. Strain and stress are induced because the bonded components hinder themselves shrinking or expanding. We expected to see a membrane deflection due to mismatches in the coefficients of thermal expansion of silicon die, adhesive and substrate.

A simple sensor geometry was chosen: A $500\ \mu\text{m}$ thick silicon die with a square membrane of $10\ \mu\text{m}$ thickness was modeled (figure 3.8). To minimise the complexity and the size of the model, the silicon die was assumed to have isotropic elastic properties. Two parameters are necessary to correctly describe mechanical behaviour of isotropic materials. We chose Young's Modulus E and Poisson's Ratio ν . The silicon die is attached to a FR4 board at the peripherals by the adhesive.

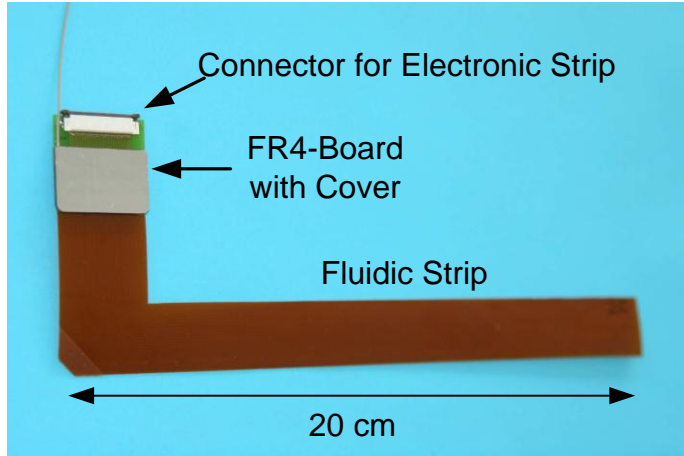
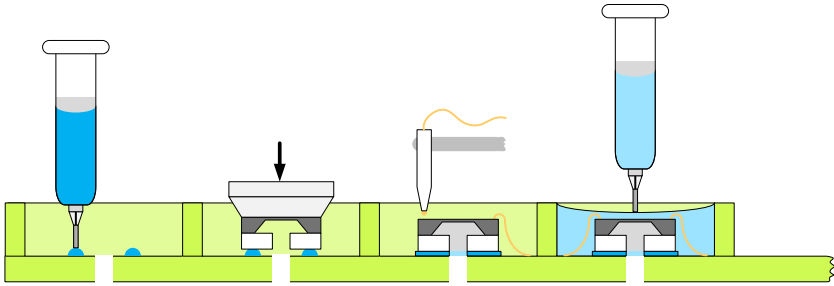


Figure 3.6: Photograph of an assembled pressure strip. The pressure sensors are protected by a silvery cover.

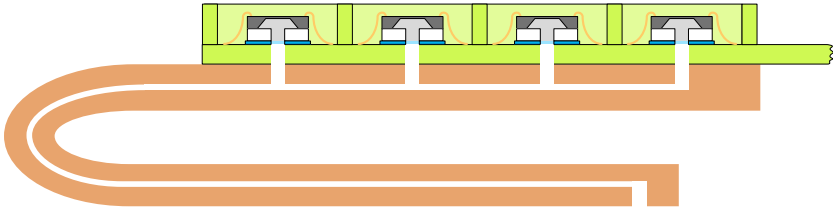
A soft silicone glue was compared with a thermosetting epoxy glue. The relevant parameters are listed in table 3.1. A temperature decrease from $40\text{ }^{\circ}\text{C}$ to $15\text{ }^{\circ}\text{C}$ was simulated with $40\text{ }^{\circ}\text{C}$ being stress free temperature. The maximum z-displacement (perpendicular to membrane) was determined for silicone-bonded and epoxy-bonded sensors subject to temperature load. For comparison, a silicon sensor was subject to a pressure of 60 mbar. The pressure acted only on the bottom surface of the membrane, which was bent upward. The results are presented in the bar chart of figure 3.9.

As expected, the membrane of the silicone-bonded device is not affected by the temperature change, whereas the epoxy-bonded sensors show a strong membrane deflection, which is comparable or even higher than the deflection induced by 60 mbar overpressure. As can also be seen from figure 3.9, that the bondline thickness influences the deflection of epoxy-bonded sensors. A thicker bondline reduces the deflection. A reasonable explanation is that a thicker adhesive layer can better compensate the shrinkage of the FR4 substrate.

The simulations show that the choice of the adhesive is a key issue in pressure sensor packaging. But the simulation results are limited. The model is strongly simplified. Piezoresistive pressure sensors have integrated piezoresistive elements in the membrane. The maximum deflection is not the only parameter. The shape of the deformed membrane



(a) From left to right: Silicone adhesive dispensing, die attachment, wire bonding, encapsulation with silicone gel.



(b) The flexible strip with the micro channels is attached to the FR4-board comprising the pressure sensors.

Figure 3.7: Bonding procedure for the pressure strip. The electronic components are not depicted.

Temperature load			-25 °C
	Young's Modulus	Poisson's Ratio	CTE
Silicone	1 MPa	0.3	315 ppm/K
Epoxy	3.5 GPa	0.4	54 ppm/K
FR4	17 GPa	0.2	12 ppm/K
Silicon	170 GPa	0.28	2.5 ppm/K

Table 3.1: Relevant simulation parameters.

is equally important. Such simple simulations do not allow precise estimation of the temperature behaviour of bonded pressure sensors. Nevertheless, finite element mechanical simulations can be a powerful tool in product development:

- Simplified models are set up quickly. Nevertheless, they can provide useful information that help make basic decisions in the first phase of product development. For example, the above presented

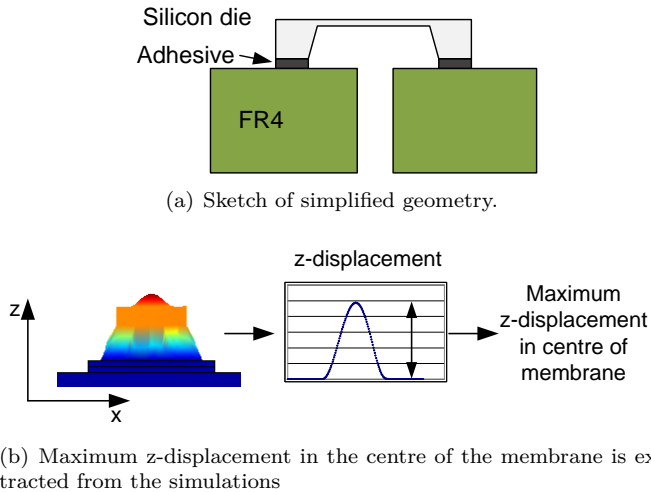


Figure 3.8: Simulation model and description.

simulations do not provide precise information on the performance of a packaged pressure sensor which is subject to temperature. But it clearly points out the different temperature behaviour of silicone-bonded and epoxy-bonded sensors.

- Large and detailed models of microsystems provide a better understanding of the long-term behaviour and the reliability of packages. For example, a detailed model of flip chip bonded solder joints can help understand different failure mechanisms (e.g. fatigue and crack propagation) and under which conditions they occur. Such simulations allow *parametric* investigations. It is much cheaper to simulate e.g. the influence of solder bump outline shapes on creep than to start a trial with real samples [42].

3.4 Characterisation

In section 3.2 it was claimed that pressure sensor packaging is crucial regarding functionality. Different CTE's of sensor and carrier material are assumed to induce stress and deformation in the sensor membrane. Furthermore, mechanical loading of the carrier board is supposed to influence the sensor. In order to verify these statements, different bonding procedures were developed and analysed. They are listed in table 3.2

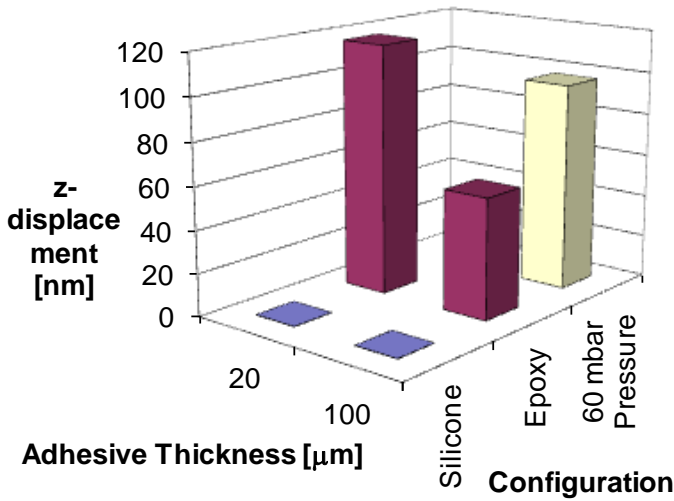


Figure 3.9: Simulation of membrane deflection due to a temperature change of $-25\text{ }^{\circ}\text{C}$. Silicone-bonded sensors show virtually no membrane deflection.

Test #	Adhesive	Young's modulus	Curing conditions
1	Silicone	$\sim 1\text{ MPa}$	$\geq 8\text{ hours @ }25\text{ }^{\circ}\text{C}$
2	Epoxy	$\sim 4\text{ GPa}$	$10\text{ min @ }120\text{ }^{\circ}\text{C}$
3	Epoxy	$\sim 4\text{ GPa}$	$4\text{ hours @ }60\text{ }^{\circ}\text{C}$

Table 3.2: Bonding procedure. The bonding adhesives and curing conditions for the 3 different bonding procedures are listed.

together with the most important material parameter of the adhesive; the Young's modulus¹. Epoxy-bonded sensors were cured at $120\text{ }^{\circ}\text{C}$ and $60\text{ }^{\circ}\text{C}$. It is expected that the curing temperature will influence the performance of the sensors. The stresses in the device are induced by cooling down from stress-free bonding temperature to room temperature. The sensors, which are bonded at $60\text{ }^{\circ}\text{C}$, are therefore expected to show a

¹In fact, two parameters are required to correctly describe the behaviour of an isotropic material under mechanical load, e.g. Young's modulus E and Poisson's ratio ν . Unfortunately, data sheets of adhesives often provide a value for Young's modulus but not for Poisson's ratio.

better performance than the sensors cured at 120 °C.

A differential pressure sensor (MS7305D from Intersema [43]) was employed. It comprises a thin diaphragm (membrane) with 4 integrated piezoresistive elements, forming a wheatstone bridge. A pressure change on one side will deform the membrane and, hence, stretch or compress the piezoresistive elements. The voltage drop across the bridge is linearly responding to the change of pressure difference on both sides of the diaphragm. According to the data sheet, the full scale range (span) of the output signal is $(\pm 110 \pm 20)$ mV, corresponding to a pressure range of ± 50 mbar. The sensitivity is the ratio of output signal (within linear full scale range) and pressure change, and equals (2.2 ± 0.4) mV/mbar. The offset value is specified to be (0 ± 40) mV. It is the output signal corresponding to zero pressure difference. Sensitivity and offset data correspond to a supply voltage of 5 V. Both terms are linearly dependent on the temperature. The relations are described by the *temperature coefficients of span and offset TCS and TCO*, respectively. The specified values are (-1900 ± 300) ppm/°C and (-40 ± 40) μ V/°C. The sensor parameters are listed in table 3.3. The performance of the packaged pressure sensors has to be compared with these parameters. A good package will neither reduce the sensitivity nor change the offset. Furthermore, the temperature dependence of sensitivity and offset should not deviate from the values of TCS and TCO.

Parameters MS7305D	Value
Chip configuration	silicon sensor with pyrex support
Chip dimensions	2.45 mm \times 2.45 mm
Chip thickness: Silicon and pyrex	0.895 mm
Sensitivity ^a	(2.2 ± 0.4) mV/mbar
Offset ^a	(0 ± 40) mV
Temperature coefficient of span ^b	(-1900 ± 300) ppm/°C
Temperature coefficient of offset ^b	(-40 ± 40) μ V/°C

^afor a supply voltage of 5 Volt.

^bAccording to the data sheet, the slope of the endpoint straight line from 25 °C to 60 °C is used to determine TCS and TCO.

Table 3.3: Pressure sensor parameters. The performance of the packaged pressure sensor has to be compared with the values for Sensitivity, Offset, TCS, and TCO in the data sheet.

3.4.1 Measurement method and setup

In order to measure the sensor's response to pressure for different temperatures, the FR4-board with the sensors (hereafter called device) was placed in an environmental chamber, which controls the temperature (see figure 3.10). The device was clamped on a metal support with fluidic channels. The metal support, in turn, was connected to a pumping system (a syringe) and the reference pressure sensor (differential pressure sensor 113LP50D-PCB from sensortechincs [44]), which was placed outside the chamber to keep it at constant temperature. Supply voltage was 5 V.

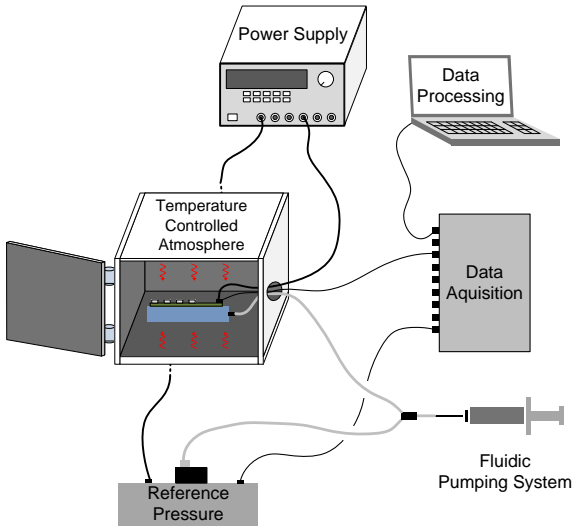


Figure 3.10: Measurement setup. The device (FR4-board with mounted sensors) is placed in an environmental chamber, which controls the temperature. The reference pressure sensor is placed outside the chamber. The raw voltage output signal is collected by a data acquisition card and displayed on a computer.

The pumping system was connected only to one side of the pressure sensor's membrane, while the other side was kept at ambient pressure. The reference pressure sensor was used to measure the applied pressure difference. It is therefore possible to relate the output signals of the device with the applied pressure.

For each bonding procedure in table 3.2 seven packaged pressure sensors were characterised. This limitation is given by the number of analog

inputs of the data acquisition card. The output signal of each sensor was monitored for varying pressures and modeled with a regression line. Sensitivity and offset are the model parameters. They were estimated by applying the 'least square'-method. The measurement was repeated for different temperatures between $-25\text{ }^{\circ}\text{C}$ and $85\text{ }^{\circ}\text{C}$. These curves are plotted in subsection 3.4.2. The estimated values for sensitivity and offset were then plotted as a function of temperature. The temperature coefficients of span and offset were derived from these graphs.

3.4.2 Response to pressure and temperature

All sensors were characterised regarding response to pressure and temperature. The response to pressure was measured within a pressure range of ± 50 mbar for a series of temperatures. For demonstration purposes, for each bonding procedure a complete measurement of one sensor is shown in figures 3.11, 3.12, and 3.13. It can already be deduced from figure 3.11, that the characteristic values of silicone-bonded pressure sensors are within the specified ranges (see table 3.3) of the sensor die.

Both types of epoxy-bonded sensors show a performance which strongly deviates from the silicone-bonded ones. The packaging influences both the sensitivity and the offset but, interestingly, the epoxy-bonded sensors responde linearly to pressure changes. A detailed discussion both on sensitivity and offset is given in the following subsections.

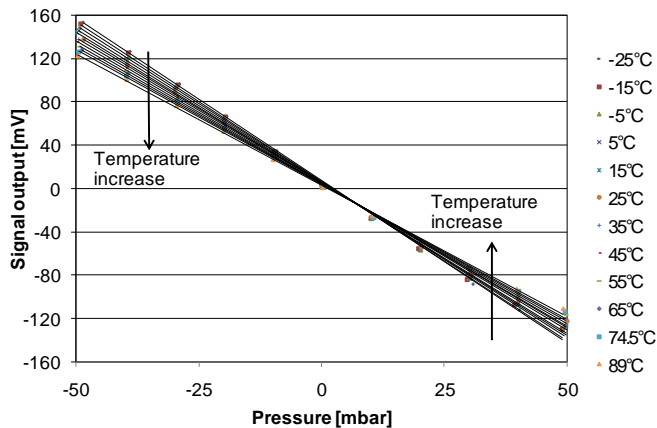


Figure 3.11: Characteristic curves for a silicone-bonded sensor. Output signal is linearly dependent on the applied pressure between ± 50 mbar. The slope of the curve (i.e. sensitivity) decreases with increasing temperature.

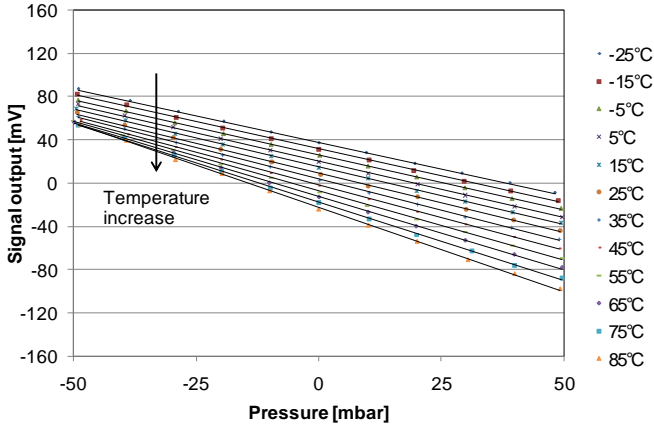


Figure 3.12: Characteristic curve for an epoxy-bonded sensor at 120 °C. Output signal is linearly dependent on the applied pressure between ± 50 mbar. The slope of the curve (i.e. sensitivity) decreases with increasing temperature.

3.4.3 Sensitivity and TCS

According to the specifications, the sensitivity (two times Span divided by 100 mbar) is (2.2 ± 0.4) mV/mbar. It decreases with increasing temperature. The temperature coefficient of span is specified by using the slope of the endpoint straight line from 25 °C to 60 °C: The difference of the sensitivities at 25 °C and 60 °C is divided by the temperature difference (35 °C). The ratio of this value and the sensitivity at 25 °C yield the temperature coefficient of span:

$$TCS = \frac{\text{Sensitivity}_{60^{\circ}\text{C}} - \text{Sensitivity}_{25^{\circ}\text{C}}}{60^{\circ}\text{C} - 25^{\circ}\text{C}} \cdot \text{Sensitivity}_{25^{\circ}\text{C}}. \quad (3.1)$$

Figure 3.14 shows the temperature dependence of the sensitivity of seven silicone-bonded pressure sensors. The sensitivity decreases with increasing temperature, in agreement with the specifications. Figure 3.14(b) shows the sensitivity of silicone-bonded sensors averaged over seven sensors. The error bars depict the standard deviation of the sensitivity. Additionally, a regression line and the associated coefficient of determination R^2 is shown. A value of R^2 close to one indicates that the regression line approximates well the data points. However, it says nothing about the causality between the measured output signal and the pressure. It

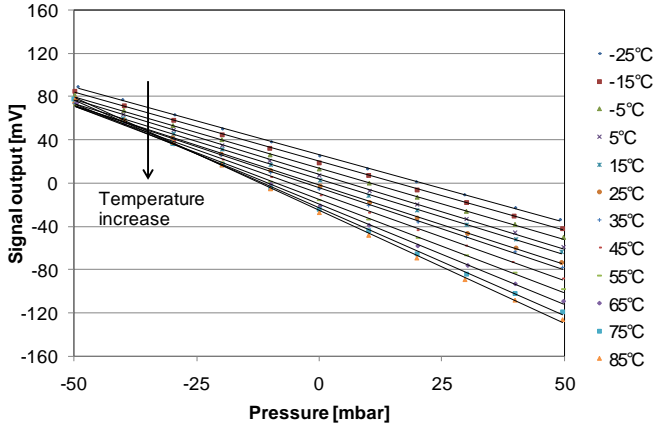


Figure 3.13: Characteristic curve for an epoxy-bonded sensor at 60 °C. Output signal is linearly dependent on the applied pressure between ± 50 mbar. The slope of the curve (i.e. sensitivity) decreases with increasing temperature.

is not possible to predict the behaviour of the output signal beyond the measured range. For the silicone-bonded sensors we find a value for R^2 of 0.9985. This value and the graph 3.14(b) indicate that it is reasonable to approximate the data points with a regression line within the measured range of ± 50 mbar.

Figures 3.15 and 3.16 show the results of identical measurements for epoxy bonded pressure sensor dies. Remarkably, the epoxy-bonded sensors show a completely different behaviour. For both types of epoxy-bonded sensors (cured at 120 °C and 60 °C) the sensitivity increases with increasing temperature. The coefficient of determination for both types of epoxy-bonded sensors is lower than the value for silicone-bonded ones. The graphs 3.15(b) and 3.16(b) indicate that the regression line is not adequate to describe the behaviour of the sensitivity in the range of ± 50 mbar.

It should be noted that the sensitivity for epoxy-bonded sensors is always lower than the sensitivity for silicone-bonded sensors. Figure 3.17 shows the temperature-dependent sensitivity of all bonding types. We recognise that the sensitivities for the epoxy-bonded sensors show similar behaviour, but the sensitivity of the sensors which were cured at 60 °C is higher. Obviously, lower curing temperatures induce less stress in the device. With increasing temperature the device approaches stress-free condition. The sensitivity of '60 °C'-bonded sensors does not reach

the value of sensitivity of silicone-bonded sensors when the temperature reaches 60 °C. There must be additional stresses in the device which cannot be attributed to temperature induced shrinkage of the components (i.e. sensor, glue, and FR4-board). It seems that the epoxy shrinks during the curing process [45], possibly due to mass loss (outgassing) or volume loss due to chemical reactions. This issue was not further investigated.

Theoretically, the temperature coefficient of span could be calculated by using measured sensitivities at any two temperatures, because, as long as the sensitivity is linearly dependent on temperature, the TCS is a constant. Using the sensitivities of two adjacent measurement points allows for determination of the temperature dependence of the TCS.

Practically, the calculation of the TCS includes the ratio of differences. Since the difference in sensitivity of two adjacent points can be a very small number, the calculation of the TCS with adjacent points yields useless values. Figure 3.18 illustrates this fact. Instead, the temperature coefficient of span was calculated by using the sensitivities at 25 °C and 65 °C. These values are listed in table 3.4, together with the values in the data sheet of the pressure sensor MS7305D. The TCS for the measured values was deduced by applying equation (3.1) to the sensitivities at 25 °C and 65 °C.

The silicone-bonded devices perform according to the specifications. In contrast, the epoxy-bonded sensors show a different behaviour. Both the sensitivity and the TCS are strongly influenced by the packaging. Nevertheless, the output signal responds linearly to the applied pressure.

TCS: slope of line from 25 °C to 60 °C

Bonding type	Value [$ppm/^\circ C$]
Data sheet	-1900 ± 300

Averaged TCS: Slope of line from 25 °C to 65 °C

Silicone-bonded at 25 °C	-1811 ± 30
Epoxy-bonded at 120 °C	5972 ± 460
Epoxy-bonded at 60 °C	6248 ± 380

Table 3.4: Temperature coefficient of span TCS for the three bonding types. The values were deduced by applying equation (3.1) to the measured sensitivities.

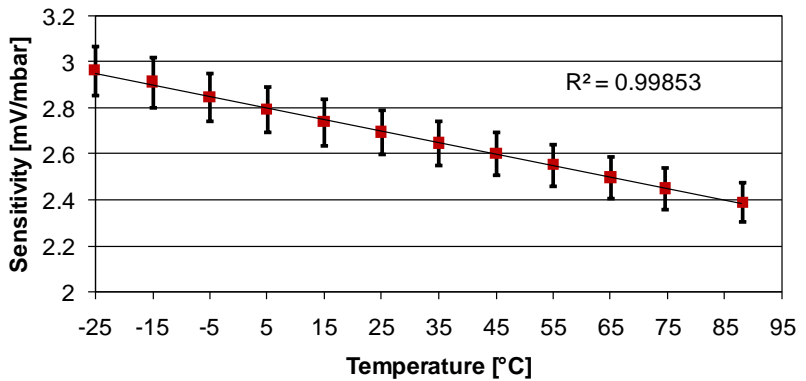
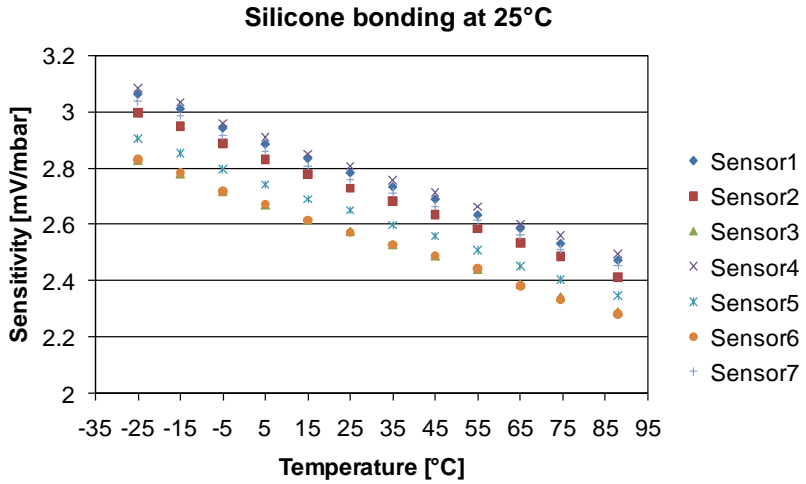


Figure 3.14: Temperature-dependent sensitivity of seven silicone-bonded pressure sensors (a) and the averaged sensitivity with standard deviation (b). The sensitivity decreases with increasing temperature, in agreement with the specifications.

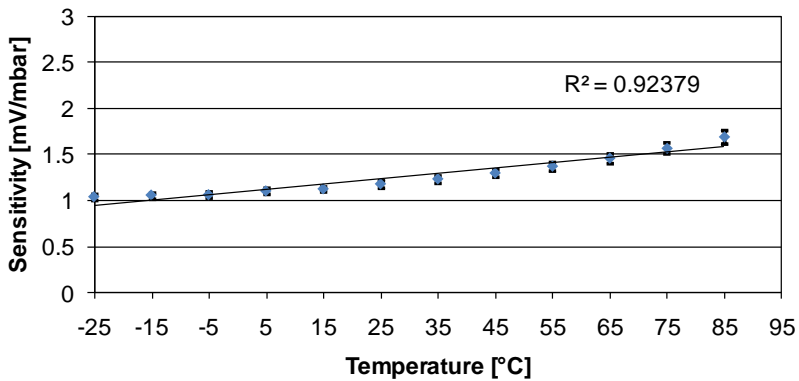
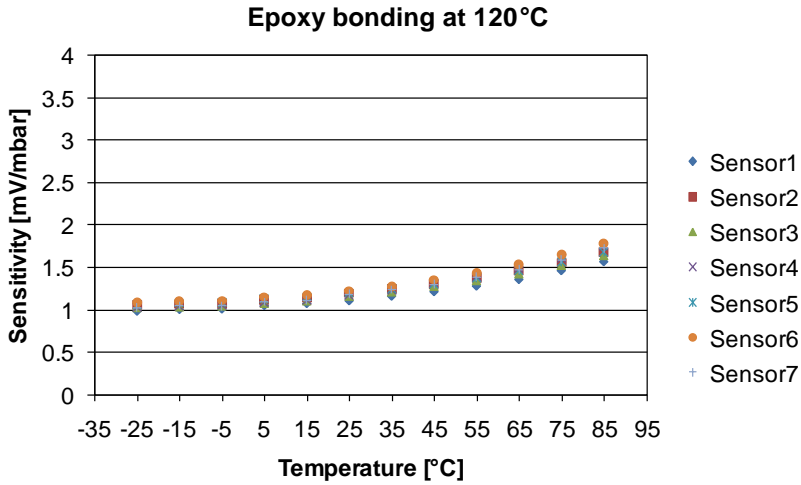
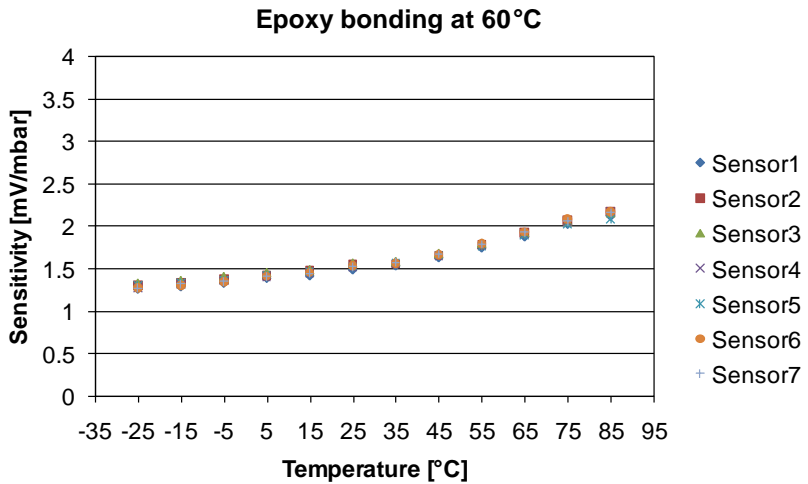
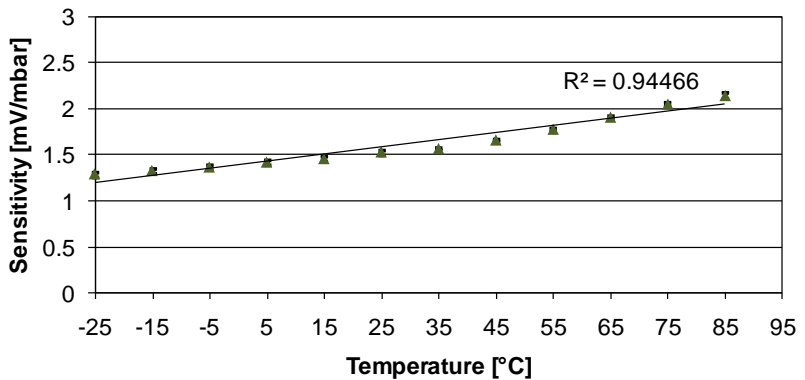


Figure 3.15: Temperature-dependent sensitivity of epoxy-bonded pressure sensors at 120 °C (a) and the averaged sensitivity with standard deviation (b). In contrast to the specifications, the sensitivity increases with increasing temperature.



(a)



(b)

Figure 3.16: Temperature-dependent sensitivity of epoxy-bonded pressure sensors at 60 °C (a) and the averaged sensitivity with standard deviation (b). In contrast to the specifications, the sensitivity increases with increasing temperature.

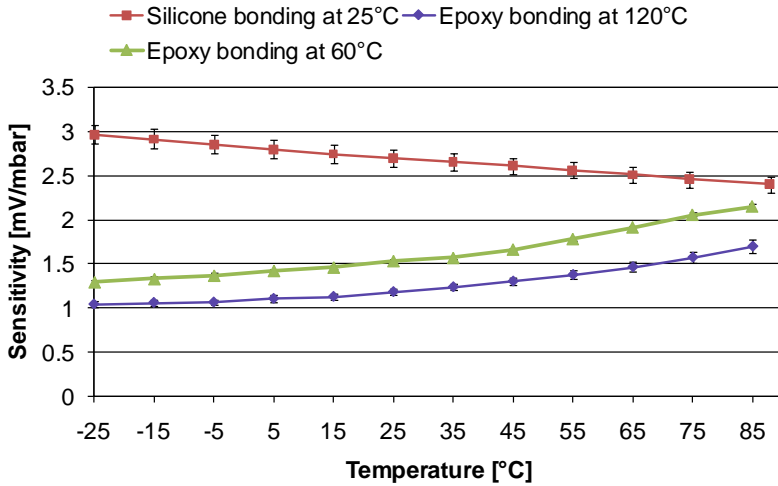


Figure 3.17: Comparison of sensitivity of silicone- and epoxy-bonded sensor dies.

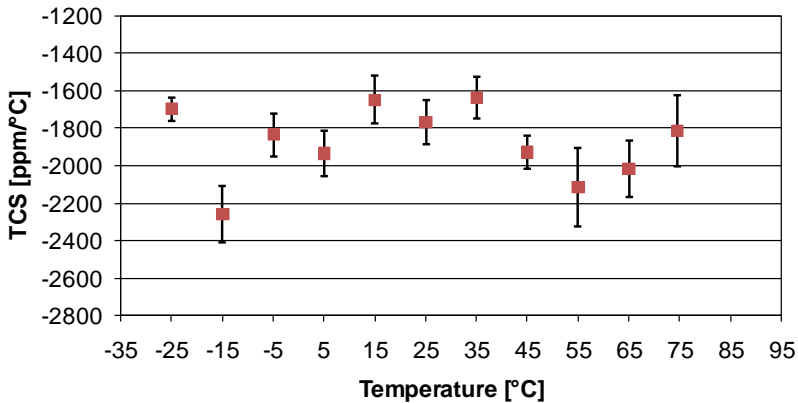


Figure 3.18: TCS as a function of temperature for silicone-bonded sensors, which was calculated using adjacent measurement points in figure 3.14(a). Even though the sensitivity for silicone-bonded sensors shows a linear dependency on temperature, there is a huge spread in the distribution of the values.

3.4.4 Offset and TCO

The data sheet of the pressure sensor MS7305D specifies for the zero pressure offset a value of (0 ± 40) mV and a temperature coefficient of offset TCO of (-40 ± 40) $\mu\text{V}/^\circ\text{C}$. The offset decreases with increasing temperature, according to the negative TCO. The temperature coefficient of offset is specified by using the slope of the endpoint straight line from 25°C to 60°C : The difference of the offsets at 25°C and 60°C is divided by the temperature difference (35°C):

$$TCO = \frac{\text{Offset}_{60^\circ\text{C}} - \text{Offset}_{25^\circ\text{C}}}{60^\circ\text{C} - 25^\circ\text{C}}. \quad (3.2)$$

The temperature dependence of the offset of seven silicone-bonded pressure sensors is shown in figure 3.19. The offset decreases with increasing temperature, in agreement with the specifications. Figure 3.19(b) shows the offset of silicone-bonded sensors averaged over seven sensors. The error bars depict the standard deviation of the offset.

Figures 3.20 and 3.21 show the results of identical measurements for epoxy-bonded pressure sensor dies. The offset strongly decreases with increasing temperature. The slope is much steeper than the listed TCO in the data sheet. Figure 3.22 shows a comparison of the temperature dependence of the offset for all types of bonding. The large values for the standard deviations indicate that the offset varies strongly from die to die. It is therefore not advisable to compare the absolute offset values of the different bonding types, because the mean values are averaged over only 7 sensors. Nevertheless, a trend of the offset can be clearly seen in the graph. These slopes can be compared to each other, since the offset measurements for different temperatures were done with the same sensors (but different sensors for each bonding type).

In table 3.5 the TCO values for the three bonding types are listed. Again, the values are calculated by using the offset values at 25°C and 65°C . Apparently, the strong temperature dependence of the epoxy-bonded sensors make it impossible to use these devices for precise measurement over a wide temperature range. To demonstrate this, let's make the following assumption: The output signal response of a device with epoxy-bonded sensors cured at 120°C was measured at 15°C for a pressure range of ± 50 mbar (see figure 3.23). This curve is stored. Each time a measurement is done with the device, the stored data allow the transformation of the output signal into pressure. First, a measurement is done at 15°C . The operator reads an output signal of -5 mV, which corresponds to an applied pressure of 18 mbar. Let's assume now that the temperature of the device rises to 55°C . This can either be achieved

by raising the ambient temperature or by exposing the device to sunlight. The output signal changes now from -5 mV to -25 mV, even though the applied pressure has not changed. The operator reads now an output signal of -25 mV. It corresponds to an ambient pressure of 40 mbar. The error is due to both the temperature dependence of offset and sensitivity. Each sensor has to be calibrated by measuring the sensitivity and offset for at least two different temperatures. The sensitivity and offset are then assumed to be linearly dependent on temperature (which is a good assumption only for silicone-bonded sensors). But even so the resolution is not as good as with silicone-bonded sensors, because the sensitivity is strongly reduced (figure 3.17).

For silicone-bonded sensors the situation is different. A temperature change will also induce an error in the calculated pressure. But this error is mainly due to the temperature-dependent sensitivity, as can be seen in figure 3.11. We also recognise that the higher the absolute value of the applied pressure, the larger the error becomes. Consequently, a precisely calibrated silicone-bonded pressure sensor also requires to be measured at two different temperatures.

TCO: slope of line from 25 °C to 60 °C

Bonding type	Value [$\mu V/^\circ C$]
Data sheet	-40 ± 40

Averaged TCO: Slope of line from 25 °C to 65 °C

Silicone-bonded at 25 °C	-24 ± 10
Epoxy-bonded at 120 °C	-610 ± 50
Epoxy-bonded at 60 °C	-430 ± 15

Table 3.5: Temperature coefficient of offset TCO for the three bonding types. The values were deduced by applying equation (3.2) to the measured offsets.

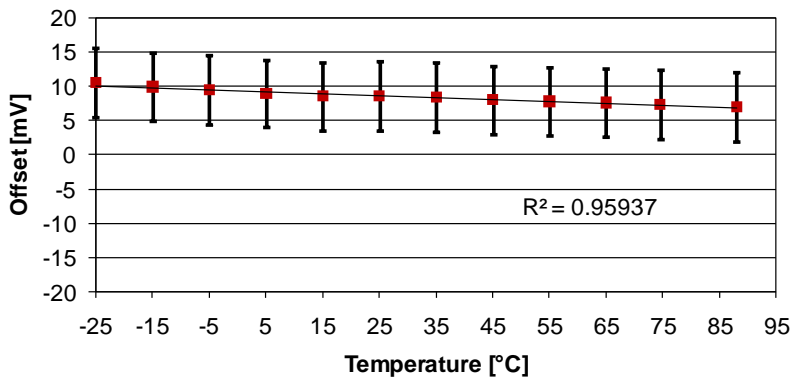
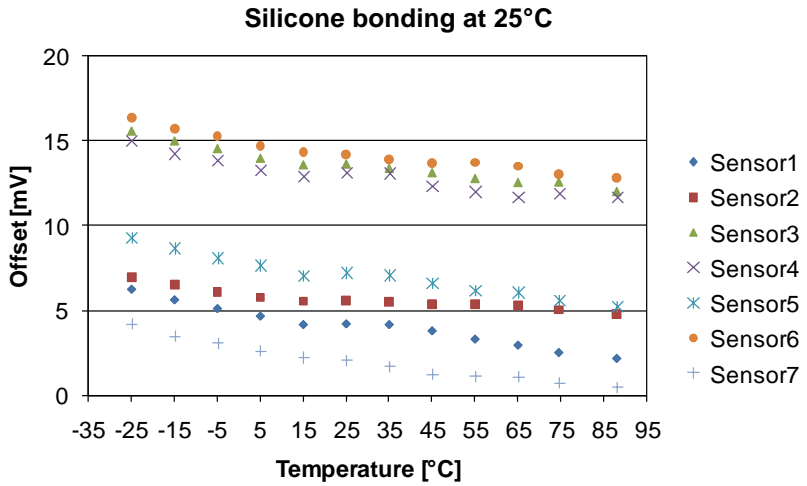


Figure 3.19: Temperature dependence of offset for seven silicone-bonded pressure sensors (a) and the averaged offset with standard deviation (b). The offset slightly decreases with increasing temperature, in agreement with the specifications.

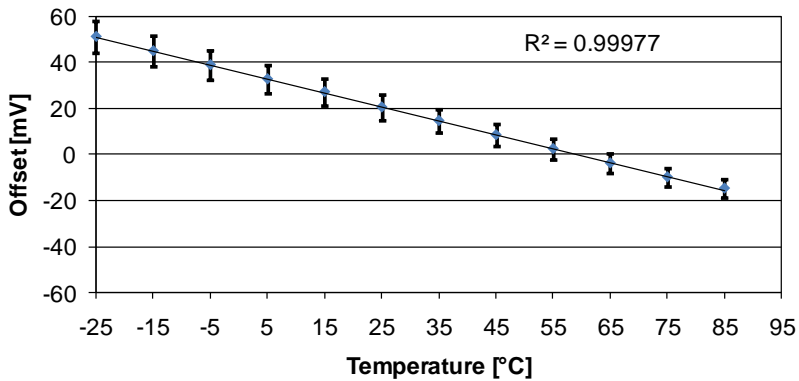
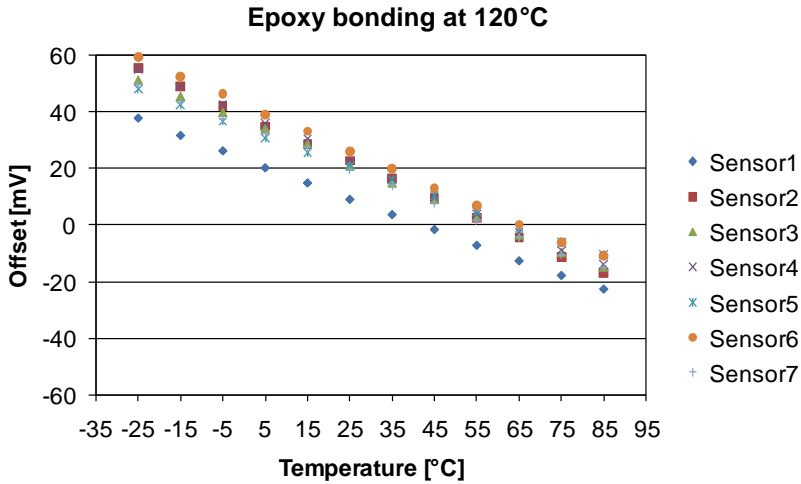
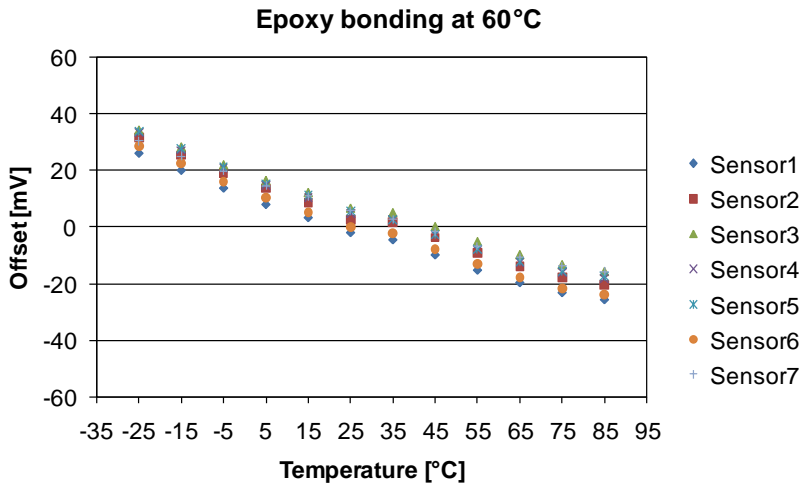
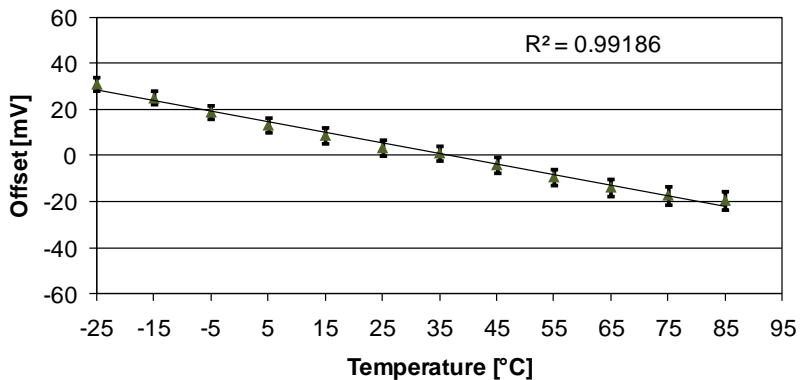


Figure 3.20: Temperature dependence of offset for epoxy-bonded pressure sensors at 120 °C (a) and the averaged offset with standard deviation (b). In contrast to the specifications, the offset strongly decreases with increasing temperature.



(a)



(b)

Figure 3.21: Temperature dependence of offset for epoxy-bonded pressure sensors at 60 °C (a) and the averaged offset with standard deviation (b). In contrast to the specifications, the offset strongly decreases with increasing temperature .

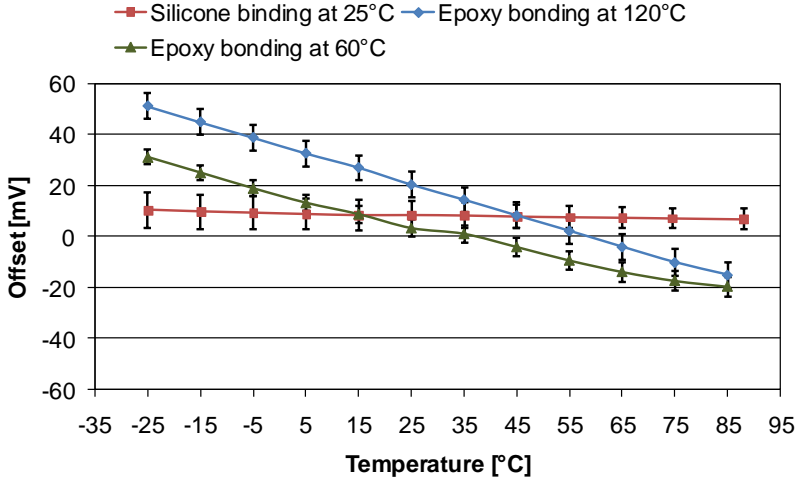


Figure 3.22: Comparison of offset of silicone- and epoxy-bonded sensor dies.

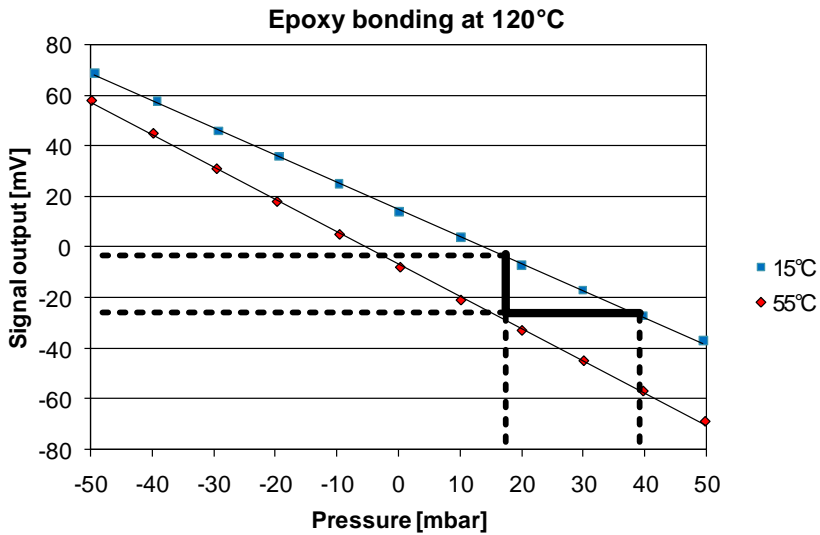


Figure 3.23: Temperature-induced error in pressure measurement with epoxy-bonded sensors.

3.5 Wind tunnel tests[†]

The performance of the pressure strip was validated through a wind tunnel test performed at the Institute of Fluid Dynamics (IFD) of the Federal Institute of Technology in Zürich (ETH Zürich). The tests were carried out by RUAG Aerospace, a specialist in Aviation and Space.

During the wind tunnel test session the pressure strip proved to be reliable and provided results which are in good agreement (both in absolute values and uncertainty) to those obtained by conventional methods. Figure 3.24 shows the measured pressures along a wing profile of the pressure strip and conventional tap reading.

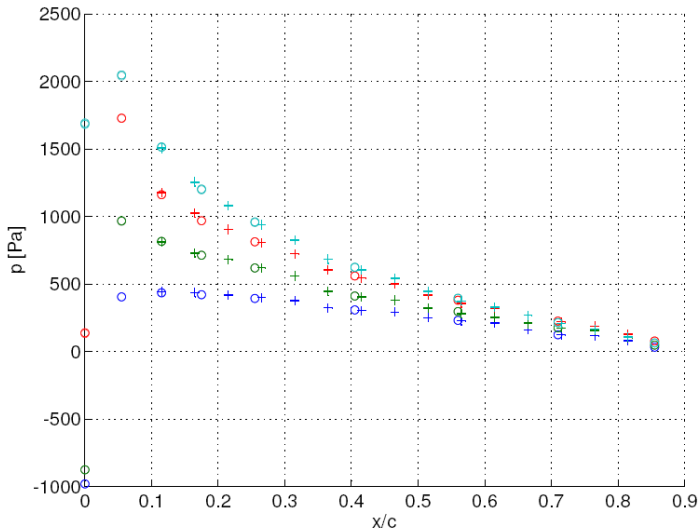


Figure 3.24: Comparison of standard pressure tap readings (o) and pressure strip measurements (+) for different angles of attack (α : 0° , 4° , 8° , 12°).

3.6 Highly-integrated pressure strip

A higher level of integration is achieved by employing flexible and thin polyimide foils, which comprise micro-channels, bonding sites for the

[†]This section is based on an article presented at the SMART SYSTEM INTEGRATION 2009 [46]

pressure sensors, and metal structures to accommodate electronic components. Such a pressure strip is shown in figure 3.25. The $200\ \mu\text{m}$ thick polyimide foil was manufactured by Epigem². The foil can be 30 cm wide and arbitrarily long. The minimal thickness is $150\ \mu\text{m}$. The micro-channels can be of arbitrary shape and as small as $50\ \mu\text{m}$. The minimal metal line width is $5\ \mu\text{m}$, and such is the space between two adjacent lines. Available metal combinations are Ni/Au, Cu/Ni/Au, and Cu/Ag.

The pressure sensor foil was realised with the silicone bonding process described above. Functionality was demonstrated with a little wind tunnel: The foil was attached to a model of a wing. The wing, in turn, was placed in the wind tunnel such way that the two openings were exposed to the flow, whereas the pressure sensor dies were separated from the air flow. The output signal of the sensors were sensitive to the air stream velocity and to the angle of attack of the air stream as expected for the surface of a wing-shaped body.

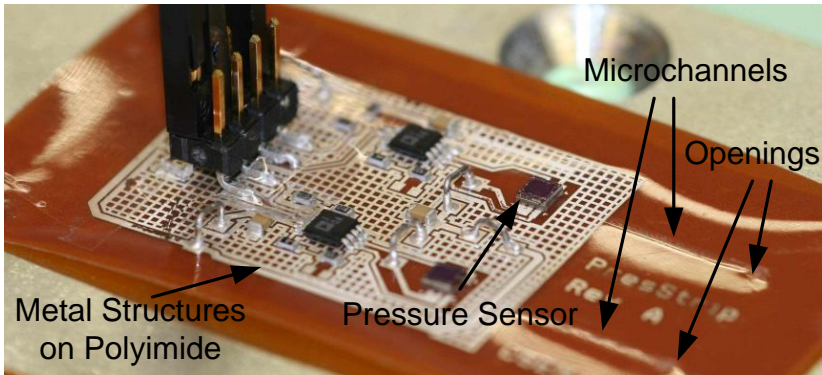


Figure 3.25: Thin polyimide film with fluidic channels and metal structures. The flexible strip accommodates the pressure sensors, the micro-channels and the electronic components.

In a next step of integration the pressure sensors and the electronic components could be completely buried in the polyimide foil. Nowadays, it is possible to thin silicon dies below $100\ \mu\text{m}$. A sandwich-structure (polyimide foil – embedded sensors and electronic components – polyimide foil) provides protection of the sensors and mechanical flexibility of the film.

²Epigem Limited, Redcar, UK.

3.7 Conclusions and outlook

Conclusions

The pressure strip concept is based on remote pressure measurement with diaphragm-based differential pressure sensors. The pressure signal is guided by channels through a thin and mechanically flexible strip, which accommodates to any shape. The concept allows a non-invasive aerodynamic pressure measurement on arbitrarily shaped bodies such as airplane wings and car bodies. The pressure strip also operates in other media like water. Capillary forces prevent the water from penetrating the micro channels in the fluidic strip. Only the pressure is transmitted to the sensor dies.

The advantage over other sensor strips [36] is the modularity. The fluidic strip, which guides the pressure signals, is a cheap flexible film. Arbitrary shapes and channel structures are easily manufactured. The FR4-board, which accommodates the sensor dies, does not have to be adapted to the body. It can be reused with differently shaped fluidic strips.

The standard bonding procedure for diaphragm-based pressure sensors is face-up attachment [47]. Any thermal stresses caused by mismatched coefficients of thermal expansion of the constituents are absorbed by the compliant silicone adhesive. Electrical connections are provided by (gold-) wire bonds. These wires are usually so thin ($17 - 30 \mu\text{m}$), that no stresses from the package are induced in the sensor diaphragm [41, 45].

Silicone-bonded pressure sensors perform according to the specifications of the bare sensor dies. This was shown for sensitivity, offset, temperature coefficient of span, and temperature coefficient of offset.

A higher level of integration can be achieved by utilising polyimide films which comprise fluidic channels and metal structures. The metal structures accommodate both pressure sensors and electronic components for signal processing.

Outlook

The characterisation of the pressure strip has to include electronic components, since they will add noise to the measurement. The resolution of a pressure measurement is hence limited by the electronic components. The presented results are based on static pressures. But it is also important to know the behaviour of the strip when dynamic pressures are applied. Pressure signals are transmitted by speed of sound. Will the

pressure signals suffer from dispersion (i.e. broadening of a pressure peak during propagation through the channels)? This dispersion will limit the minimum distance in time of two subsequent peaks, which can be resolved.

As explained before, silicone bonding of diaphragm-based pressure sensors has no influence on the performance of the sensor dies. But there are numerous drawbacks associated with face-up bonding. Electrical contacts have to be provided by so-called (gold-) wire bonds. Apart from additional costs in manufacture (wire bond equipment, skilled operator, time...), the wire bonds require a lot of space both in horizontal and vertical dimensions, as figure 3.7(a) shows. The wires provide a connection from the sensor pads to metal pads on the FR4-board. The additional space occupied by these pads drastically increases the size of the board. Moreover, the wires have to be protected against both mechanical load (e.g. when touching the wires) and moisture and other elements promoting corrosion, because it is often not possible to avoid the usage of corrosive metals.

Flip chip bonding eliminates these drawbacks. Cost in manufacture are potentially reduced, because additional steps for wire bonding and application of a protection gel are avoided. The metal pads on the carrier board do not require more space than already occupied by the sensor die. Such a flip chip approach is presented in chapter 4. An application is presented in chapter 5.

Novel Approaches to Sensor Packaging

4

4.1 Introduction

We present below a bonding process for silicon chips on PMMA platforms for microfluidic applications. The bonding process is based on ACA bonding. Furthermore, we developed a flip chip ACA bonding process suited for MEMS devices like diaphragm-based pressure sensors.

Silicon/plastic convergence: ACA bonding on low T_g substrates

In the frame of the European Project INTEGRAM*plus* we developed a fast and cheap bonding process for silicon sensors on low T_g substrates. An ACA flip chip process was demonstrated on PMMA (Poly[methyl methacrylate]). As a low cost thermoplastic material PMMA is especially suited for microfluidic applications for disposable devices. Often a sample to be analysed must be guided to the appropriate sensor [48] or actuator [49] element through a fluidic channel or network. Hence, flip chip bonding of the active element on a PMMA platform is a suitable integration approach. Two tasks arise: Flip chip bonding must provide electrical and mechanical contacts, and the sensing area of the chip must be sealed against the outside world. Both can be achieved by the use of ACA, as it is depicted in figure 4.1.

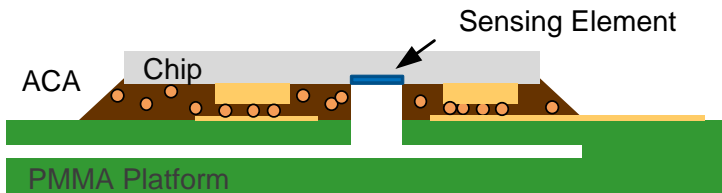


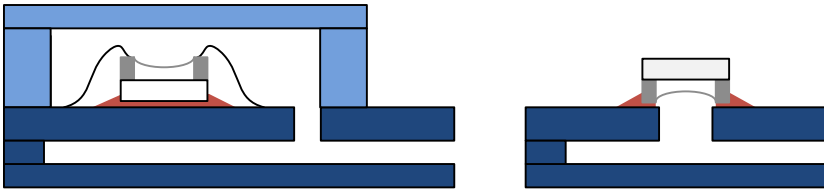
Figure 4.1: Flip chip with ACA on PMMA for microfluidic applications. The ACA ring provides electrical and mechanical contact as well as sealing of the microfluidic channel and the sensing element of the sensor.

Flip chip packaging of MEMS devices

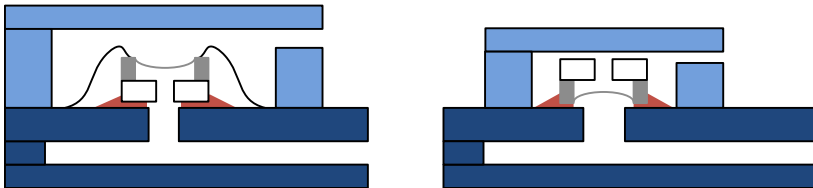
Diaphragm-based (i.e. membrane) pressure sensors are sensitive to stress and strain by nature. A flip chip process which does not degrade the performance of a pressure sensor is hence a *generic approach* for flip chip packaging of MEMS devices. Specifically, the bonding process and temperature variations of the package must not influence the behaviour of the sensor.

Flip chip bonding offers several advantages over standard bonding (i.e. face-up bonding with wire bonds) regarding size and complexity of the package, as figure 4.2 depicts. Wire bonded chips have a larger footprint than flip chip bonded devices. Furthermore, they require additional space in vertical dimension due to a protective cover for the wire loops.

Differential pressure sensors need fluidic connection to both sides of the membrane (figure 4.2(b)). The pressure sensor is preferably placed in a cavity with a fluidic inlet/outlet. The advantage of the flip chip approach is a small dead volume because the cavity can be virtually as small as the sensor die.



(a) Comparison of standard bonding (left) and flip chip bonding (right) of an absolute pressure sensor.



(b) Comparison of standard bonding (left) and flip chip bonding (right) of a differential pressure sensor.

Figure 4.2: Flip chip bonding of pressure sensors offers reduction in size and complexity of the package. The size reduction scales linearly with the number of assembled pressure sensors.

Flip chip packaging of diaphragm based pressure sensors was first addressed in the medical field of minimally invasive interventions. Very small pressure sensor packages are required in order to use them in catheters [50]. Unprotected and protruding wire bonds must be avoided. Different flip chip approaches were developed in the past few years. The most advanced and promising interconnection techniques for MEMS devices are solder bumps, ACA/ACF, and isotropically conductive polymer bumps [51, 52]. Each technique has advantages and drawbacks: Solder bumps provide a mechanically strong but also stiff interconnection. An additional underfilling step is required. The underfill must be prevented from filling the gap under the diaphragm. This can be accomplished by the means of e.g. flowstops [53]. Mechanical load and thermally induced stresses and strains were not addressed in this investigation. A stiff flip chip interconnection cannot provide mechanical decoupling of the sensor from the substrate. More recently, this was shown in [54]: “Flip chip soldering on common PCB substrates has a deleterious effect on the performance of the devices in terms of their dependence on temperature”. This is due to a CTE mismatch between silicon and FR4 (PCB).

Another technique employs electrically conductive adhesives for flip chip bonding. Limitations and drawbacks are described in [55]. In order to use conductive polymer bumps as a solder replacement, micromachined conductive polymer bumps were developed. A flip chip process with thermoplastic conductive polymer bumps is described in [56, 57]. Compared to solder bumps, thermoplastic polymer bumps are softer, making them possible candidates for flip chip packaging of stress sensitive MEMS devices. Thermally induced displacements, due to CTE mismatches, are potentially absorbed by the compliant polymer bumps.

Recently, ACF was employed as a flip chip interconnect technology for a diaphragm based pressure sensor [58]. The sensor was attached to a PCB. In order to avoid the CTE mismatch-induced degradation of the sensor characteristics, the pressure sensor was physically anchored (i.e. attached) with the ACF to the PCB only at one edge. Temperature stability was achieved. But the ACF bonding process did not provide air- or fluid-tight sealing of the diaphragm.

Above presented flip chip packages approach the CTE mismatch problem with novel flip chip techniques. Alternatively, it is possible to adapt the substrate to the sensor. There are two ways to do this: First, substrates can be compliant or flexible. CTE mismatches rather cause a deflection of the substrate than the sensor’s diaphragm [59]. Second, the substrate’s CTE matches the CTE of the sensor. We here present such an approach

with a borofloat glass substrate. The flip chip technique is ACA-bonding with gold studs.

4.2 ACA bonding on low T_g substrates for low-cost microfluidic applications

In order to prove both reliable electrical connection and fluid-tight sealing of flip chip ACA-bonded sensors on PMMA, two kinds of experiments are carried out. First, dummy-silicon chips are bonded with ACA to a PMMA base piece for electrical testing. The metal structures on chip and PMMA are identical to those presented in chapter 2. The metallisation on the surface of the PMMA substrate is laterally embedded in a dielectric so that it is co-planar with the surface of the base piece. The base piece was manufactured by Epigem Ltd.

Second, in order to test the fluid-tightness of the ACA, $5 \times 5 \text{ mm}^2$ small PMMA dies are flip chip bonded to a silicon platform. The ACA is dispensed in a rectangle with a hole in the centre to produce a cavity between PMMA die and silicon platform. Vertical holes are drilled through the PMMA to access the cavity (see also figure 4.6(b)).

The bonding process is almost identical to the process described in subsection 2.4.3. Only the bonding temperature profile had to be adjusted to account for the glass transition temperature T_g of PMMA around $100 \text{ }^\circ\text{C}$ and the force was reduced to 5 g/bump . The employed ACA is *Hysol FP5300* with a T_g of $125 \text{ }^\circ\text{C}$.

4.2.1 Characterisation of electrical and mechanical contact[†]

Experimental procedure

A PMMA platform with several bonding sits (see figure 4.3) of design (a) and (b) was used (see section 2.2 on page 10). Three silicon chips of each design were flip chip bonded on the PMMA platform with gold studs and ACA.

Design (a) allows the determination of the electrical resistance of a contact. Contacts of design (b) samples form a daisy-chain of 30 interconnections. Three chips of each type were bonded on the PMMA strip. The measurement method is identical to the one described in section 2.3.

[†]The results of this subsection have been presented at the 1st European Conference on Microfluidics 2008 [60].

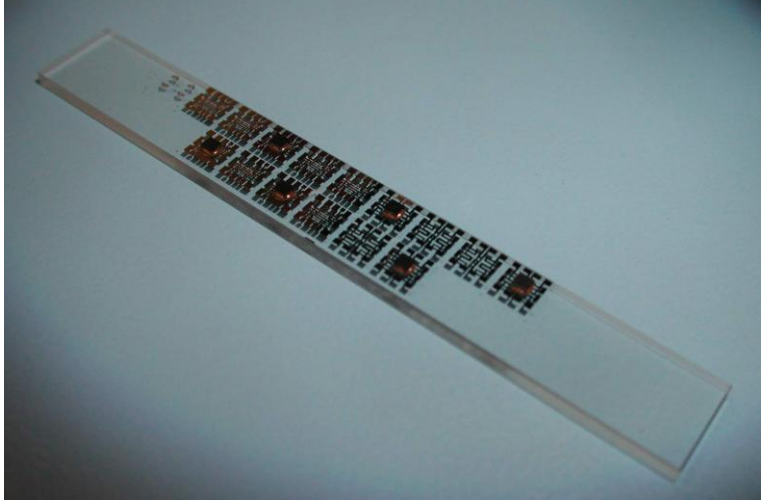


Figure 4.3: PMMA platform with several flip chip bonding sites. Three chips of each design (a) and (b) are flip chip bonded with ACA.

Results and discussion

The ACA-on-PMMA process provides the highest averaged resistance and standard deviation of the compared flip chip bonding techniques in chapter 2. This is due to the low T_g of the PMMA. Even though heat was only applied through the chip during the bonding process, the PMMA deforms underneath the gold studs. Bending of the substrate metallisation is assumed to reduce the number of contacting spheres in the contact surface. Figure 4.4 is a photograph of a cross section through an ACA contact. It can be clearly seen that the metallisation of the PMMA (bottom) is deformed. This photograph was taken from a device of the first trials. They had contact resistances in the range of 1Ω . Next generation devices had an improved metallisation of $5 \mu\text{m}$ Ni coated with a thin Au layer. Even though the PMMA deforms during the bonding process, the hard Ni pads do not deform.

The measured bump resistances of the four sites of design (a) devices (a1, a2, and a3) and the serial resistances of 30 bumps of the three design (b) devices (b4, b5, and b6) are listed in table 4.1. The averaged bump resistances of the twelve measured contacts is $21.5 \text{ m}\Omega$. The standard deviation is $5.2 \text{ m}\Omega$. For comparison, chart 2.22 is again plotted in figure 4.5 with the values for the ACA process on PMMA substrates.

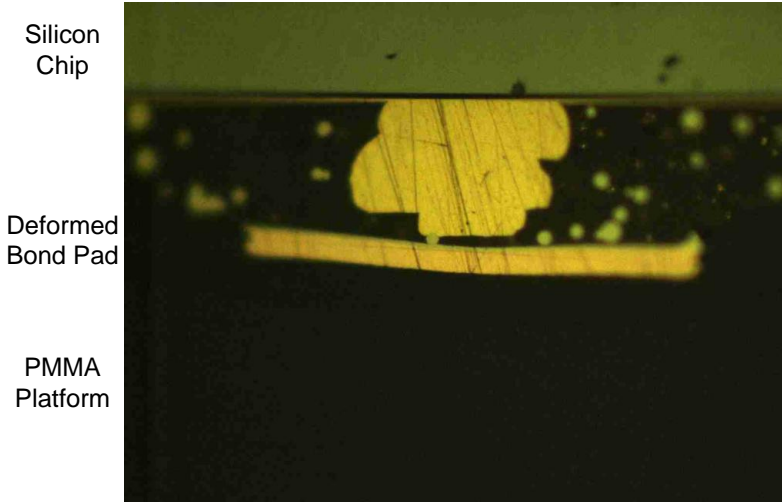


Figure 4.4: Photograph of a cross section through an ACA-on-PMMA contact.

The serial resistances of the devices b4 to b6 are also listed in table 4.1. All three devices have finite resistance values, implying that all 30 contacts were bonded. The average resistance is $1397\text{ m}\Omega$, and the standard deviation is $42\text{ m}\Omega$. The serial resistance is higher than 30 times the average contact resistance because the metal lines between the contacts contribute to the measured serial resistance.

The finite serial resistances show that the bonding process is repeatable. But the large standard deviations both for single and serial contacts imply that there is another source of variation apart from variation in gold stud size, variation in local particle density and particle flow (compare with chapter 2). It is assumed that the surface roughness and the planarity of the PMMA platform also influence the number of conducting spheres in the ACA contact.

4.2.2 Characterisation of sealing properties[†]

Experimental procedure

Several PMMA dies with a size of $5 \times 5\text{ mm}^2$ are bonded face-down with ACA to a silicon platform (figure 4.6). Gold studs were placed on the

[†]The results of this subsection have been presented at the 1st European Conference on Microfluidics 2008 [60].

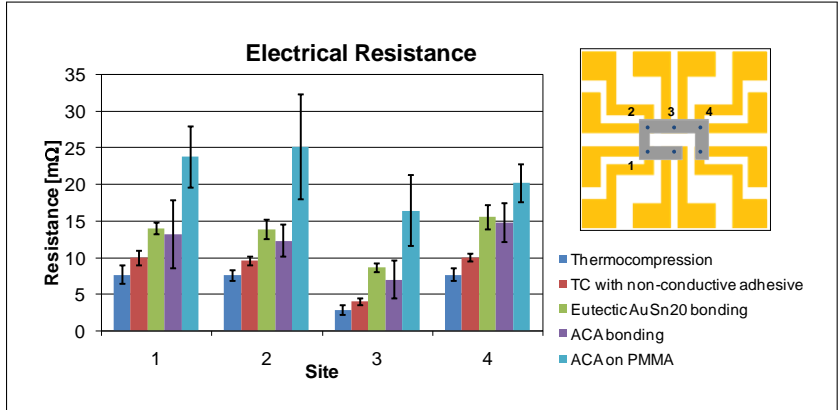


Figure 4.5: Electrical resistance for the investigated flip chip bonding processes including the ACA-on-PMMA-process.

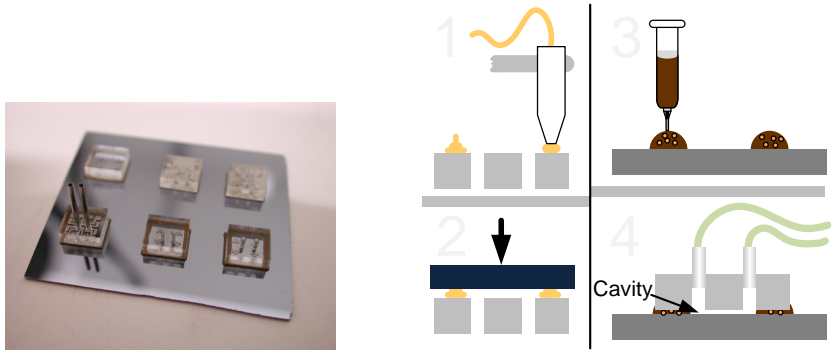


Figure 4.6: Silicon platform with ACA-bonded PMMA dies. Vertical holes provide access to the cavity. Bonding process: Gold studs are placed on the PMMA dies (1) and flattened (2). Then the ACA-ring is dispensed on the silicon platform (3) and the PMMA die is bonded onto the platform. Fluidic plugs provide connection to the cavity (4).

PMMA metallisation to create a gap between die and platform. The ACA was dispensed in a rectangle with an opening in the centre to form a closed cavity. Two vertical holes (inlet and outlet) are drilled through the PMMA dies to provide fluidic access to the cavity.

The following experiments were carried out to test the sealing prop-

Design a		
Device	Site	Resistance [$\text{m}\Omega$], $\pm 1 \text{ m}\Omega$
a1	1	25
	2	19
	3	21
	4	18
a2	1	22
	2	26
	3	24
	4	19
a3	1	19
	2	33
	3	12
	4	20
Design b		
Device	Site	Resistance [$\text{m}\Omega$], $\pm 10 \text{ m}\Omega$
b4	(30 serial bumps)	1410
b5		1430
b6		1350

Table 4.1: Contact resistance (design a) and serial resistance of 30 bumps (design b).

erties and the bond strength of the ACA bonding process:

- A peristaltic pump was used to test the fluid tightness of the cavity. Three devices were connected to the pump and water was pumped through the cavity for 90 min at a flow rate of 3 ml/min. Visual inspection should reveal leaks.
- The bond strength was tested by applying an overpressure of up to 6 bar.

Results and discussion

All three tested devices proved to be fluid-tight. Visual inspection revealed no leak in the ACA ring.

Usually, the required flow rates in liquid handling are much smaller than the flow rates in this experiment. Since lower flows reduce the probability of leaks due to smaller pressures in the microchannels, these tests qualify the bonding method also for smaller liquid flows.

In the second experiment, the pressure in the cavity was increased by 2 bar every two hours. The ACA sealing showed no leak or degradation up to 6 bar. At this pressure a leak occurred at the connection between PMMA die and tubing system, but there was no leak in the ACA bond.

These experiments showed that ACA bonding on PMMA is suited for sensor dies too small for a standard micro-gasket approach.

4.2.3 Reliability: temperature cycling tests[†]

Reliability problems often arise from a combination of different materials in a package. Especially mismatches in the coefficients of thermal expansion cause stress and strain. Polymers (e.g. PMMA) have much higher CTEs than metals, ceramics, or semiconductor materials. There are ways to alter the CTE of polymers. Widespread is the addition of fillers. Underfiller materials for flip chip bonds are sometimes filled with silica beads to reduce the CTE, as FR4 consists of an epoxy matrix with glass fibers. Furthermore, formulations of polymer materials employed in microtechnology are constantly improved. Unfortunately, production and material cost increase with improved products.

PMMA has a CTE in the range of 90 ppm/K – 160 ppm/K [19], whereas ceramics, metals and semiconductors have a much lower CTE. CTEs of a few common materials in microelectronics are listed in table 4.2. The values are taken from [19], unless otherwise noted.

Another issue in bonding technology is that polymers are subject to moisture/water uptake. Water can form inside the package. Adhesion loss between polymers and silicon/metals [61], delamination, corrosion of the flip chip joints, popcorn effects, and hygro swelling [62, 63] are reasons for device failure. Hygro swelling is treated in section 4.4.

Temperature cycling tests reveal information on *thermal fatigue* which is defined as the premature fracture resulting from cyclic stresses due to temperature changes. It is considered to significantly affect the performance and the life time of a flip chip device. Often *Accelerated lifetime tests* are carried out to predict the life time of an assembly because it is not feasible to test a device under real conditions. Accelerated temperature cycling is a widespread lifetime test. The device is alternately subject to hot and cold temperatures. The CTE mismatches between the components of the device impose displacements which produce mechanical stresses in the flip chip joint.

[†]The here presented tests were carried out in collaboration with R. Ziltener from Injector Solutions

Material	CTE (linear) [ppm/K]
Si	2.5
Si ₃ Ni ₄	2.7 – 3.1
Au	14.2
AuSn20 alloy	16.2 [64]
SnPb40 alloy	24
FR4	
longitudinal ^a	6.6
transversal ^a	30
Hysol FP5300	47 (data sheet)
PMMA	90 – 162

^awith respect to the orientation of the glass fibers.

Table 4.2: CTE for several materials commonly used in flip chip technology. From [19].

Such accelerated lifetime tests were carried out with the above described PMMA samples. In order to compare the results, the tests were also done with samples described in chapter 2. These are ACA-bonded chips on borofloat glass substrates.

Experimental procedure

PMMA dies with a size of $5 \times 5 \text{ mm}^2$ and a thickness of 2 mm are employed.

The PMMA devices were assembled without gold studs, in contrast to the devices presented in chapter 2 and section 4.2. The reason is the need for a fast and low-cost process. No gold stud bumping and flattening processes save time and equipment. Instead, the Si-chips were flip chip ACA-bonded directly to the PMMA surface, resulting in a smaller gap and a larger contact surface. The bonding process is described in table 4.3.

The bonding force acts on the entire chip surface which is $1.6 \text{ mm} \times 1.6 \text{ mm}$. The applied pressures are hence 1.56 MPa for a force of 400 g (type a) and 0.39 MPa for a force of 100 g (type b), respectively. For comparison reasons, devices which were ACA-bonded on borofloat glass are cycled with the identical temperature profile. These devices have flattened gold studs which define the contact surface. Type (c) samples were bonded with a force of 13 g/bump, type (d) samples were bonded with a force of 3 g/bump. Assuming an average contact surface of the

ACA bonding on PMMA	
Ramp up chip	in 15 seconds from 80 °C to 180 °C
Ramp up substrate	no heating
Hold time	12 seconds
N ₂ cooling	no active cooling
Force	
Type a	400 g
Type b	100 g
ACA bonding on borofloat glass	
Ramp up chip	in 15 seconds from 80 °C to 180 °C
Ramp up substrate	in 15 seconds from 50 °C to 180 °C
Hold time	12 seconds
N ₂ cooling	no active cooling
Force	
Type c	13 g/bump
Type d	3 g/bump
Adhesive	Hysol FP5300; epoxy matrix with Au-coated Ni particles with an average size of 7 μm

Table 4.3: Bonding parameters for ACA bonding on PMMA and on borofloat glass. The PMMA substrate is not heated actively.

bumps of 2000 μm² the bonding forces of 13 g/bump and 3 g/bump correspond to a pressure of 65 MPa and 15 MPa.

All samples have 30 contacts which form a daisy chain (design (b), see chapter 2). The increase in serial resistance is used as the failure criterion.

The temperature cycling tests were carried out in the environmental chamber SH-240 from ESPEC. The maximal and minimal temperatures of the cycle are +85 °C and -40 °C, respectively. The dwell time of both temperatures was 8 min with a ramp up and ramp down time of 120 min. The humidity was set to 50 %RH (above 0 °C).

Results

The initial resistance values are listed in table 4.4. The temperature cycling tests revealed that most ACA-on-PMMA devices did not survive the first 50 cycles. Tables 4.5 and 4.6 show the resistance as a function of the number of temperature cycles. The $\frac{1}{2}$ symbol indicates the appearance of failure, which is defined as a broken daisy-chain (infinite

Type	Device no.	Initial Resistance [$\text{m}\Omega$], $\pm 10 \text{ m}\Omega$
a	1	810
	2	820
	3	860
	4	560
	5	810
b	1	1430
	2	1660
	3	1410
	4	1390
	5	950
	6	1420
c	1	1200
	2	1190
	3	1240
	4	1250
d	1	2290
	2	3140
	3	2470
	4	2090

Table 4.4: Initial serial resistance of 30 bumps. The different types are described in table 4.3. Type (a) and (b) devices have thicker metal lines between the contacts than type (c) and (d) devices. The serial resistances have to be compared between (a) and (b) devices and between (c) and (d) devices. A discussion is given in the text.

resistance). In the case of PMMA devices with a bonding pressure of 1.56 MPa two samples did not survive the first 50 cycles. Another two samples failed after 100 cycles. One sample passed 128 cycles without failure. This sample did not show a significant change in the resistance.

In the case of PMMA devices with a bonding pressure of 0.39 MPa three samples failed after 50 cycles. Another two samples failed after 128 cycles. One sample passed 128 cycles. It showed a significant change in resistance.

Four borofloat-glass samples were assembled with a bonding force of 13 g/bump (type c), and four samples were assembled with a bonding force of only 3 g/bump (type d). The results are presented in figures 4.7 and 4.8. The type (c) samples all passed 278 cycles without failure. The serial resistances increased less than 20 %.

Type (d) samples show both a higher initial serial resistance and a

PMMA substrate, 400g, type a				
Device no.	Resistance after cycles [Ω]			
	initial	50 cycles	100 cycles	128 cycles
1	0.81	$\not\downarrow$		
2	0.82	$\not\downarrow$		
3	0.86	1	$\not\downarrow$	
4	0.56	10.3	$\not\downarrow$	
5	0.81	0.91	0.92	1.08

Table 4.5: Temperature cycling results for ACA bonding on PMMA with a bonding pressure of 1.56 MPa (type a).

PMMA substrate, 100g, type b				
Device no.	Resistance after cycles [Ω]			
	initial	50 cycles	100 cycles	128 cycles
1	1.43	$\not\downarrow$		
2	1.66	$\not\downarrow$		
3	1.41	$\not\downarrow$		
4	1.39	1.68	1.78	$\not\downarrow$
5	0.95	2.05	2.90	$\not\downarrow$
6	1.42	1.49	3.81	2.27

Table 4.6: Temperature cycling results for ACA bonding on PMMA with a bonding pressure of 0.39 MPa (type b).

stronger increase in serial resistance while the samples are cycled. Nevertheless, all four samples passed 278 cycles.

The definition of failure should be chosen according to the application. It strongly affects the results. Microelectronic devices may fail long time before the resistance of a flip chip joint becomes infinite. Therefore it is more realistic to define the failure as an increase of the resistance above a certain value which is related to the initial resistance. For example, the failure can be defined as an increase of 20 % of the initial value. Figure 4.9 shows the accumulative failure of the previously presented types (a), (b), (c), and (d). If the failure is defined as a 20 % increase there is a huge difference between the two types with borofloat glass substrates (c and d).

Discussion

The initial resistance values of PMMA samples and glass samples cannot be compared in terms of absolute values because the metal lines between the contacts contribute to the resistance. The resistance of the metal lines is lower for the PMMA samples because they have thicker metal lines. A comparison between type (a) and (b) samples and between type (c) and (d) samples reveals that the bonding force is a crucial parameter. Even though all samples have a finite initial resistance, the large variation and the high absolute resistance values of type (b) and (d) imply that the bonding force is too low for type (b) and (d) samples.

It can be seen from figure 4.9 that the definition of failure affects the results of temperature cycling tests. If failure is determined to be a 20 % increase in initial resistance the glass samples of type (d) with a bonding force of 3 g/bump fail after 100 cycles, whereas 0 % of type (c) samples fail even after 278 cycles.

The number of samples tested is not large enough to make a statistically relevant comparison of types (a),(b), and (c). Still, type (d) samples show a significantly better performance. Obviously, the here presented ACA bonding process on PMMA can never be as resistant to temperature cycles as samples with a borofloat glass substrate and an

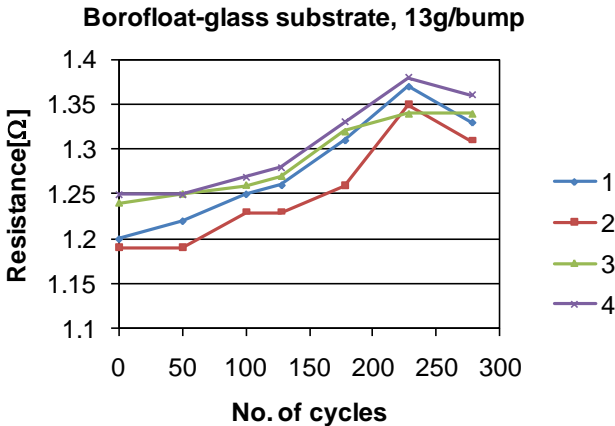


Figure 4.7: Temperature cycling results for ACA bonding on glass with a bonding force of 13 g/bump (type c). No device failed after 278 cycles.

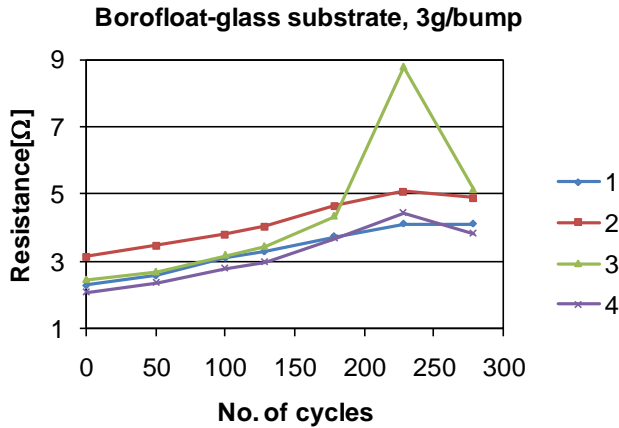


Figure 4.8: Temperature cycling results for ACA bonding on glass with a bonding force of 3 g/bump (type d). All devices failed because their resistances were raised more than 20 % of the initial resistance. Nevertheless, all devices have finite resistances after 270 cycles.

optimised bonding process.

We believe this low resistance to temperature cycling is due to the low T_g of the PMMA and the mismatch of CTE between the components of the device.

The bonding process can be considered as the first temperature cycle undergone by the device. Since the temperature in the process goes beyond the glass transition temperature the CTE mismatch between the components becomes even more pronounced. Even though the PMMA substrate was not actively heated in the above described process, the PMMA top surface locally heats up while in contact with the hot chip. The bonding process therefore introduces deformation and stress in the device which reduces the resistance to thermal fatigue during temperature cycling.

The high temperature of the PMMA top surface during the bonding process causes the PMMA to deform. Figure 4.10 shows a cross-sectional photograph of the ACA joint for type (a) devices bonded with the above described bonding parameters (400 g bonding force and 180 °C). It can be seen that the PMMA is strongly distorted from the bonding process. Figure 4.11 shows the ACA joint of a type (b) device which was bonded with the identical temperature profile but with a reduced bonding force

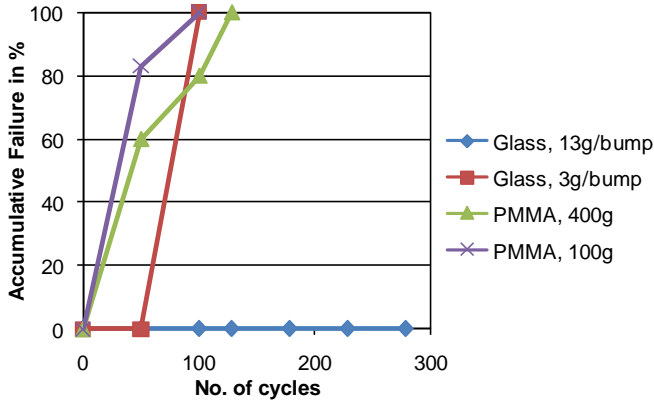


Figure 4.9: Accumulative failure of ACA-on-PMMA and ACA-on-glass samples. The failure criterion is an increase of the resistance above 20 % of the initial serial resistance.

of 100 g. The distortion is less pronounced but still recognisable. Furthermore, delamination of the metal line exactly at the edge of the ACA can be seen (right side of the photograph). For comparison, a device was assembled with a bonding temperature of 90 °C which is below the T_g of PMMA. The bonding force is 400 g and the bonding time 7 min. The ACA-joint of such a device is shown in figure 4.12. The PMMA is not distorted. Such an assembly process may increase the yield of the bonding process, but it is not expected to yield improved resistance to temperature cycling of functional devices since the CTE mismatch still remains. The drawback is the long bonding time which makes the process unfeasible for low-cost (disposable) products.

Temperature cycling imposes stresses at the PMMA – metal line – ACA interface because the CTE mismatches are highest between PMMA, metal and ACA. Cracking of the metal lines is therefore assumed to be a main reason for the low resistance to thermal fatigue in temperature cycles.

Resistance to thermal fatigue could be improved by reducing the CTE of the PMMA. This can be achieved by adding e.g. ceramic particle fillers [65].

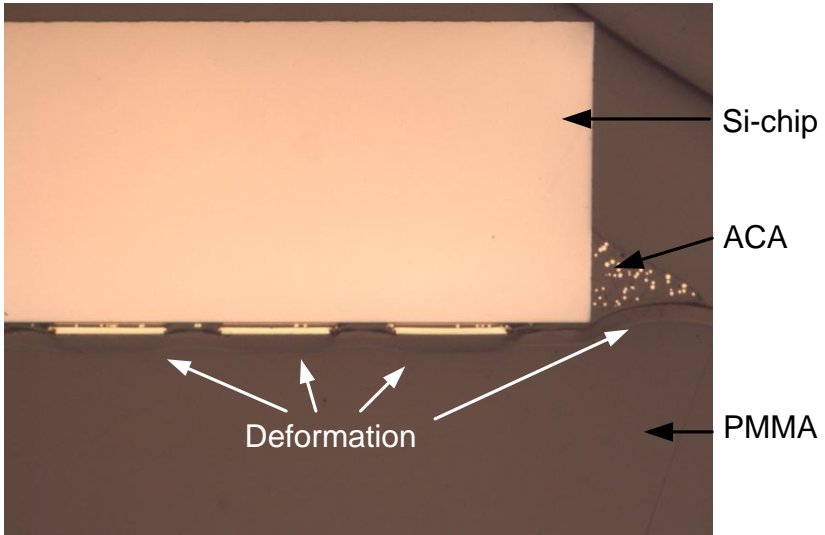


Figure 4.10: Cross section of a flip chip ACA-joint on a PMMA substrate. The bonding force is 400 g and the bonding temperature of the chip 180 °C. Deformation of the PMMA is visible.

4.2.4 Autoclave tests

Autoclaving is a common method to clean medical devices. Reusability of medical components, devices, or tools requires a sterilisation process. Any product has to survive the sterilisation without considerable degradation of its performance.

We therefore tested the resistance of PMMA substrates with ACA-bonded Si-chips (see previous subsections) to autoclaving.

Experimental procedure

A Sanyo Mac-1600PV sterilisation equipment was used to carry out the autoclaving tests. The chamber is saturated with water. The sample is subject to the 121 °C hot moisturised atmosphere for 20 min at an overpressure of 0.11 MPa. The sterilisation is followed by a 45 min long drying step.

The PMMA strip from subsection 4.2.1 (see figure 4.3) with three samples of design (a) and three samples of design (b) was autoclaved. The contact resistances of the design (a) samples and the serial resistances of the design (b) samples were measured before and after auto-

claving. The data are compared with the previously measured initial resistances presented in subsection 4.2.1.

Results

The contact resistances after autoclaving of the three design (a) devices on the PMMA strip are presented graphically in figure 4.13. The measured resistances before and after autoclaving are compared with the initial resistances of the samples. It can be seen that the resistance has not considerably changed within the 106 days storage at room temperature (and 50 %RH) between first measurement and the measurement right before the autoclaving test. However, the contact resistances of all 12 bonding sites are increased by approximately 2 m Ω after the autoclaving tests, which is 10 % of the initial value. Only site 4 of sample a2 shows a larger increase than 20 %.

The serial resistance of the design (b) samples with a daisy-chain structure of 30 bumps was also measured before and after autoclaving. The results are listed in table 4.7.

105 days storage at room temperature and 50 % humidity have not influenced the serial resistance. However, the autoclaving test drastically

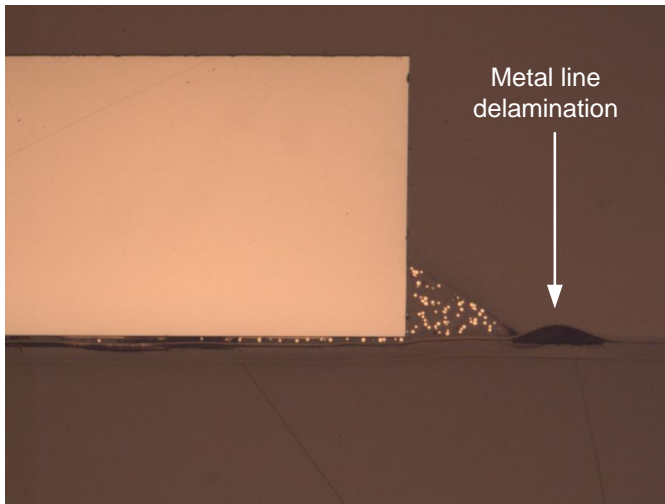


Figure 4.11: Cross section of a flip chip ACA-joint on a PMMA substrate. The bonding force is 100 g and the bonding temperature of the chip 180 °C. Small deformations are visible.



Figure 4.12: Cross section of a flip chip ACA-joint on a PMMA substrate. The bonding force is 400 g and the bonding temperature of the chip 90 °C. No deformation is visible.

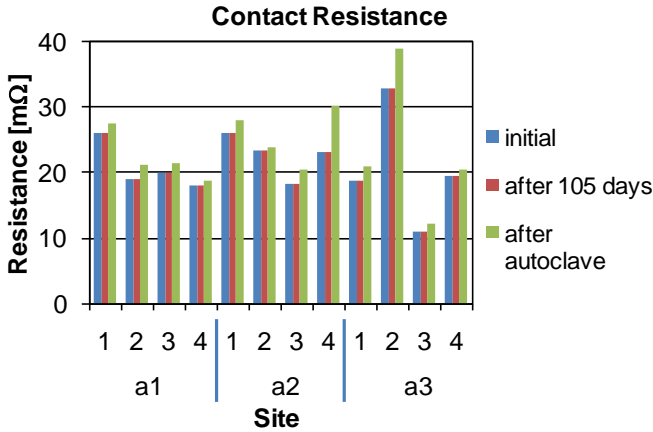
Design b: daisy chain with 30 bumps			
Sample	Serial Resistance [$m\Omega$] $\pm 10 m\Omega$		
	initial	after 105 days	after autoclaving
b4	1430	1430	2210
b5	1470	1460	2220
b6	1370	1370	∞

Table 4.7: Serial resistance of design (b) samples right after manufacture, 105 days after manufacture, and after autoclaving.

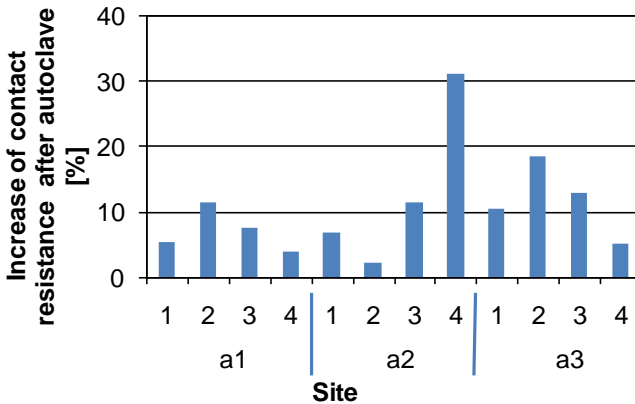
increased the resistances. Sample b6 has even an open circuit.

Discussion

The measurements of the contact resistances of samples a1, a2, and a3 after autoclaving tests show an increase of the electrical resistance in the range of 10 %. Only two contacts show considerably higher values. These samples are remarkably resistant to autoclaving. Since these devices allow measurement of the electrical contact resistance, this experiment provides only information about the resistance to autoclaving of



(a) Contact resistances before and after autoclaving



(b) Relative increase of the contact resistance after autoclaving

Figure 4.13: Contact resistances of PMMA substrates with flip chip ACA-bonded Si-chips. The resistances before and after autoclaving are compared with the initial values already presented in subsection 4.2.1.

the ACA-joint in the present configuration with Si-chips on PMMA substrates. No information is obtained about other failures that potentially reduce the performance of the device. Such a failure is e.g. cracking of the metal lines. The metal lines of the PMMA substrate are particularly

prone to failure because the Ni metal lines are sandwiches between the PMMA and the ACA which have a higher CTE than the metal. An increase in electrical resistance of the metal lines is not detected by contact resistance measurements.

The design (b) samples b4, b5, and b6 allow the measurement of the serial resistance of the daisy-chain which includes the metal lines between two adjacent bumps. The measured electrical resistance is hence a better measure to estimate the resistance to fatigue during autoclaving of the whole device. The metal lines between the bumps and the ACA-joints influence the electrical resistance.

We believe that the bigger contribution to the increase of the serial resistance of samples b4, b5, and b6 is mainly due to the metal lines. From the autoclaving tests with the samples a1, a2, and a3 we deduce that the average increase of the electrical resistance of an ACA-joint is approximately 2 m Ω . The design (b) samples have 30 bumps. The serial resistance should increase by 60 m Ω if the increase of the samples was only due to the degradation of the ACA-joint. However, the increase of the resistance of the samples b4 and b5 is in the range of 800 m Ω . Sample b6 even has an open circuit.

The resistance to degradation in autoclaving (and temperature cycling) could potentially be increased by adding ceramic fillers to the PMMA, which reduces the CTE.

It is not clear how the metal lines could be changed to improve the resistance to fatigue. One could argue that a softer and ductile metal can bear larger deformations and hence will not suffer from cracking. On the other hand, harder materials with a higher tensile strength are less deformed. The accumulative strain is potentially lower. Which path is better depends on many parameters of the package e.g. the metal lines thickness, width, and geometry, PMMA thickness, and ACA properties.

4.2.5 Conclusions

We demonstrated a low-cost and fast flip chip process on a low T_g substrate. The bonding technique provides electrical and mechanical connection of the sensor die and sealing of the active element of the sensor in one bonding step.

The employed technique is ACA-bonding with gold studs, as described in chapter 2. The electrical resistance of an interconnection is in the range of 20 m Ω , which is only slightly higher than resistances of ACA-on-glass devices. The mechanical connection is strong. It can stand up to 6 bar overpressure without any sign of degradation.

Resistance to temperature cycling of PMMA devices is strongly re-

duced compared to borofloat-glass devices. The reason are the stresses imposed on the ACA-joint and the metal lines due to the high CTE of PMMA. Such devices can be used in microfluidic applications which usually have less stringent requirements for reliability than electronic packages.

4.3 Flip chip packaging of MEMS devices

As it was described in the introduction, different flip chip techniques were developed and applied to diaphragm-based pressure sensor packaging. Basically, there are two approaches to manufacture functional devices which are not significantly influenced by the package. Either a flip chip technique is chosen which provides a compliant interconnection, or a substrate material is used which does not impose stress and strain on the sensor membrane due to temperature variations.

The first approach may employ compliant conductive polymer bumps. The substrate material may be rigid FR4. The latter approach requires a flexible substrate or a substrate with a CTE similar to the one of the sensor material.

We here present a bonding process of the second approach. The flip chip bonding technique is 'ACA with gold studs', presented in chapter 2 and section 4.2. It provides mechanical and electrical connection and it seals the membrane/diaphragm against the outside world. Since the contact pads of the sensor are located at the peripherals of the top surface, the ACA ring covers the pads while the membrane is free.

It was the aim to characterise the performance of the assembled sensors with regard to sensitivity (to pressure) and temperature dependence. The measurement procedure is described in table 4.8. The measurement setup is identical to the one shown in figure 3.10.

4.3.1 Experimental procedure

The chosen substrate material is commercially available borofloat glass. It has a CTE of 3.3 ppm/K. A metallised borofloat wafer was ordered from Reinhardt Microtech. The metal layers are (from bottom to top): Cr (adhesion layer), TiW (0.05 μm), Pd (0.15 μm), and Au (1.5 μm). The metal was structured with a TruMark Station 5000 UV laser. The substrate has holes under the sensor membrane to provide fluidic access, and metal pads to contact the sensor. Two assembled devices with different numbers of bonding sites are shown in figure 4.14. We used the differential pressure sensor MS7305D from Intersema [43], see chapter 3

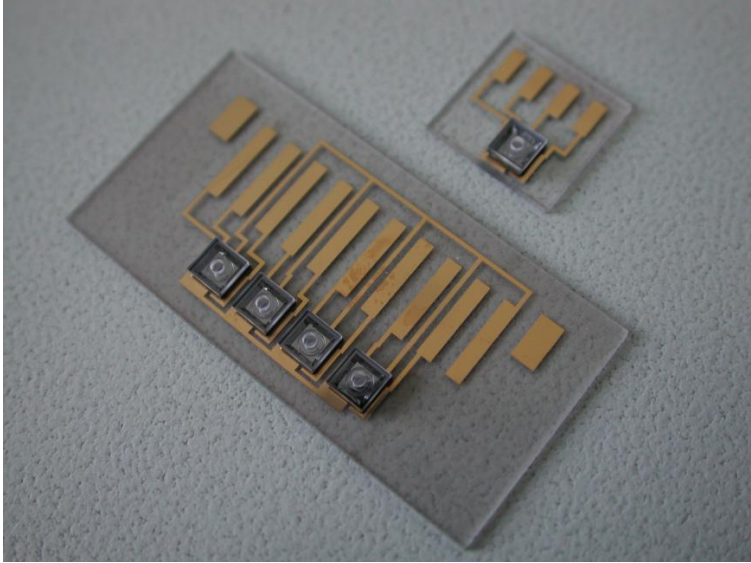


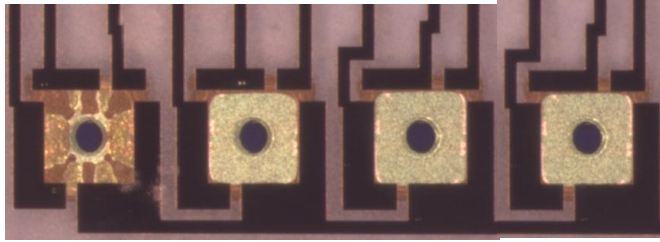
Figure 4.14: Structured borofloat glass substrate with flipped pressure sensors.

for the specifications. The design is identical to the one presented on the right side of figure 4.2(b), except that the devices have no cover.

to be characterised	Method of measurement
Sensitivity (to pressure)	Pressure is applied to one side of the sensor, the raw output signal is measured at room temperature. Supply voltage is 5 V.
Temperature dependence (TCO)	The sensors are placed in the environmental chamber. The offset signal is measured as a function of the temperature. See figure 3.10. Supply voltage is 5 V.

Table 4.8: Procedure for characterising the flip chip bonded pressure sensors on borofloat Glass. The bonding technique is ACA-bonding with gold studs.

It is crucial that the ACA does not touch the membrane of the sensor. The challenge is to dispense the right amount of ACA at the right place. If the dispensed ACA lines are too high, it will uncontrollably flow during



	4	3	2	1
Offset [mV]	230.0	1.7	10.0	8.8

Figure 4.15: Bottom view photograph of ACA-bonded pressure sensors from figure 4.14. Sensors 1,2, and 3 have a well defined ACA ring of rectangular shape which does not touch the membrane. The membrane of sensor 4 is partially covered with ACA. The sensor cannot be used.

sensor attachment and potentially touch the membrane. If the dispensed lines are too low, there is a risk of leaks in the ACA or open circuits. Figure 4.15 is a bottom view photograph (through the borofloat glass) of the four sensors shown in figure 4.14. The membrane of sensor 4 is partially covered with the ACA. The measured offset shows that the curing process has deformed the membrane. The sensor cannot be used because the offset is beyond the linear full scale range of 110 mV. Sensors 1,2, and 3 have a well defined ACA ring around the membrane. Their offsets are within the specified range of the sensor.

It is not possible to measure the temperature coefficient of the sensitivity (TCS, see chapter 3): In order to connect the fluidic in- and outlets, the devices were clamped between two PMMA plates with the fluidic inlets. Temperature variations let the PMMA plates expand and shrink. Therefore, the mechanical coupling between the plates and the device would render the measurements invalid.

Instead, the temperature dependence of the offset was used to characterise the sensitivity of the device to temperature changes. The offset can be measured without clamping the devices between the PMMA plates because no pressure has to be applied to the sensors. The results are compared to the temperature coefficient of offset (TCO) from the data sheet.

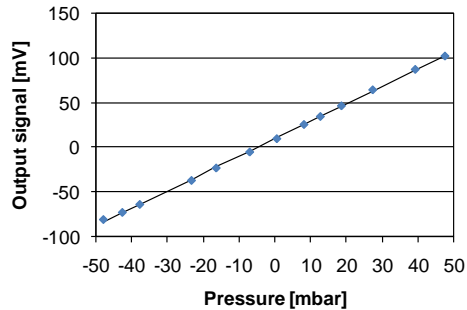


Figure 4.16: Characteristic output signal as function of pressure for sensor 1.

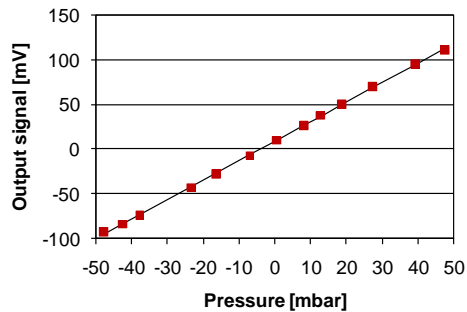


Figure 4.17: Characteristic output signal as function of pressure for sensor 2.

4.3.2 Results

Sensitivity

Three flip chip bonded pressure sensors were characterised as described above. Figures 4.16, 4.17, and 4.18 show the output signals of the sensors as a function of the applied pressure at room temperature. The sensors response linearly to the pressure. The sensitivities and offsets, calculated from these graphes, are listed in table 4.9. The specifications from the data sheet are also listed. The devices perform according to the specifications.

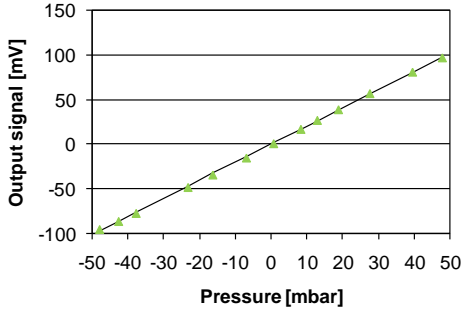


Figure 4.18: Characteristic output signal as function of pressure for sensor 3.

Sensor	Sensitivity [mV/mbar]	Offset [mV]
1	1.95	10.1
2	2.18	9.4
3	2.03	0.5
Specs	2.2 ± 0.4	0 ± 40

Table 4.9: Sensitivity and offset for three sensors flip chip bonded with ACA on a borofloat substrate.

Temperature dependence

This simple measurement should provide a first estimation of the temperature dependence of flip chip bonded pressure sensors. However, the measurement was precise enough to compare the measured values with the specifications of the pressure sensor dies.

The temperature was varied between $+25\text{ }^{\circ}\text{C}$ and $+85\text{ }^{\circ}\text{C}$ and the supply voltage is 5 V. The offsets of the three sensors are plotted in the figures 4.19, 4.20, and 4.21.

Starting point was $+25\text{ }^{\circ}\text{C}$. Then the temperature was steadily increase to $85\text{ }^{\circ}\text{C}$, followed by a cooling phase until $25\text{ }^{\circ}\text{C}$ was reached. According to the TCO of $(-40 \pm 40)\text{ }\mu\text{V}/^{\circ}\text{C}$ listed in the data sheet of the pressure sensor an offset shift of $(2.4 \pm 2.4)\text{ mV}$ is acceptable for a temperature variation of $60\text{ }^{\circ}\text{C}$. The variation of the offset for all three samples is below 1.5 mV, but no tendency can be observed. Each data point is averaged over 10 measured values, taken at random within 5 seconds. The error bars indicate the standard deviation. Therefore a flip chip bonded pressure sensor has a maximal temperature dependent

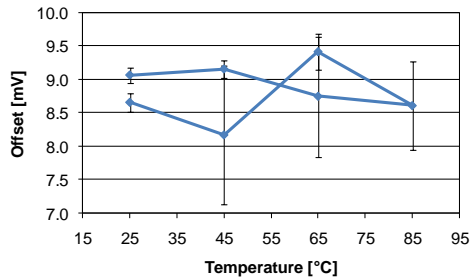


Figure 4.19: Characteristic offset signal as a function of temperature for sensor 1.

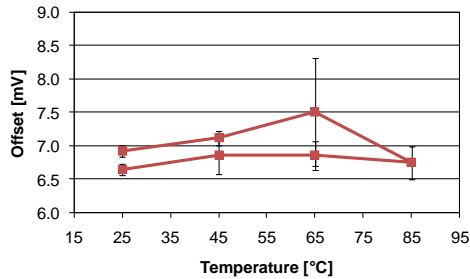


Figure 4.20: Characteristic offset signal as a function of temperature for sensor 2.

inaccuracy of 1.4 % ($= \frac{1.5 \text{ mV}}{110 \text{ mV}}$) per 60 °C or, equivalent, $\pm 25 \mu\text{V}/^\circ\text{C}$.

Offset drift

The repetition of the above described measurement after one week showed that the offset has a drift. The signal had changed by approximately 4mV which corresponds to 3.6 % of the full scale output range. Figure 4.22 shows the evolution of the offset as a function of time. The offset variations of the three tested devices within six hours are maximal 0.2 mV.

4.3.3 Discussion

The results show that sensitivity to pressure, offset, and temperature dependence of offset are within the specified range of the pressure sensor

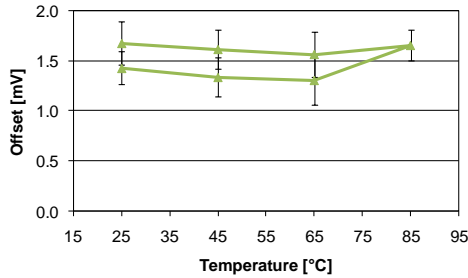


Figure 4.21: Characteristic offset signal as a function of temperature for sensor 3.

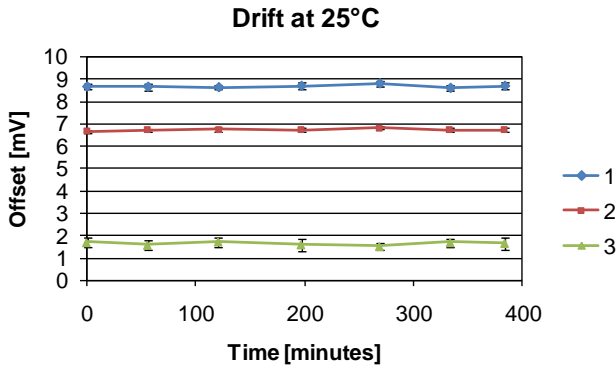


Figure 4.22: Offset drift within six hours.

die. The offset has a time-dependent drift which is probably due to the pressure sensor die.

The drift changed by approximately 3.6 % over one week. However, the drift is so slow (no drift detected over six hours) that flip chip bonded pressure sensors can be precise devices if a simple calibration cycle of the offset is carried out.

4.3.4 Conclusions

Flip chip packaging of MEMS devices was investigated by using diaphragm-based differential pressure sensors. The used bonding technique is ACA-bonding with gold studs on borofloat glass substrates.

The flip chip bonded pressure sensors show a linear response to applied pressure. The sensitivity is approximately 2 mV/mbar when biased with 5 V, which is slightly lower than for standard bonded sensors presented in chapter 3, but still within the specified range. The number of tested sensors is too small to draw statistically relevant conclusions on the influence of the bonding technique on the sensitivity.

The temperature induced shift of the offset is within the specified range of the bare pressure sensor.

The packaged sensors show a time-dependent offset drift of approximately 3.6 mV over one week. However, no drift was detected when the offset was measured every hour during six hours. Therefore, a simple offset calibration allows precise measurements.

Flip chip packaging of pressure sensors offers size reduction in the plane and out of plane. An array of sensor dies does not occupy much more space on the substrate than the footprint of the sensors because wire bonding is avoided.

Such an approach may replace the sensor array presented in chapter 3. The size of the substrate can be reduced by a factor of approximately 4.

4.4 Simulation of hygro swelling induced stresses in a MEMS device[†]

The influence of thermal expansion and the mismatch of CTEs was thoroughly discussed in chapter 3 and the previous sections. It is now clear that thermal management, design, and selection of materials is crucial in MEMS packaging and, in general, in microtechnology. Polymers usually have a high CTE and therefore introduce strain and stress in a package which is subject to temperature variations.

Polymers are also prone to moisture uptake. Apart from other corrosion processes in solder joints which are promoted by moisture, uptake of water lets the polymers swell. This phenomena is called *hygro swelling*.

Hygro swelling induced stress is mainly an issue in packages with flip chip contacts where the mechanical connection is provided by solder ball interconnects or thermocompressed gold studs. Such devices usually require polymeric underfills which impose stresses on the interconnects while they swell [66].

[†]The results of this section have been presented at the COMSOL conference, Grenoble, October 23-24, 2007. The article is included in the CD-proceedings [62].

Electrical contact in ACA-bonded devices is maintained by a compressive force of the ACA matrix on the conductive spheres in the contact surface. Main concern in ACA bonding is not stresses imposed by swelling, but there is a risk of open circuits if the compressive force is reduced by the swelling [67].

The aim of this section is to investigate the influence of swelling polymers to flip-chip soldered MEMS devices. Water diffusion in the underfill and swelling of the underfill is simulated. The swelling induced deformation of the membrane (diaphragm) is compared with thermally induced deformations.

The simulations are carried out with the finite-element (FEM) programme COMSOL Multiphysics.

4.4.1 Simulation model

The modelled device is a flip chip bonded absolute pressure sensor which consists of a silicon die with the diaphragm and a pyrex (borofloat) glass anodically bonded to the back side of the silicon die. Figure 4.23 sketches the device. The pressure sensor is face-down attached to a PCB with a rectangular hole which happens to be under the diaphragm. Solder balls provide the flip chip interconnect to the PCB. An underfill fills the gap between sensor and PCB, but does not occupy the volume directly under the diaphragm. The dimensions of the components and their material parameters are listed in table 4.10 on page 111. The underfill parameters are from [68].

4.4.2 Diffusion

The goal of the diffusion simulation is to obtain an idea about the time scale at which diffusion occurs.

Water diffusion in the underfill was simulated based on Fick's law (i.e. diffusion equation):

$$\frac{\partial C}{\partial t} = \Delta(D \cdot C). \quad (4.1)$$

C is the moisture concentration in the underfill, Δ is the Laplace operator, and D is the diffusivity ($[D] = m^2/s$). Assuming that D is independent of C and, therefore, constant in space, the diffusion equation has a unique and explicit solution [69]. Epoxies can sometimes show non-fickian behaviour (diffusion cannot be properly described by equation (4.1)). The reason is that D may be a function of C . It has also been observed that final moisture content depends on prior history [70]. This

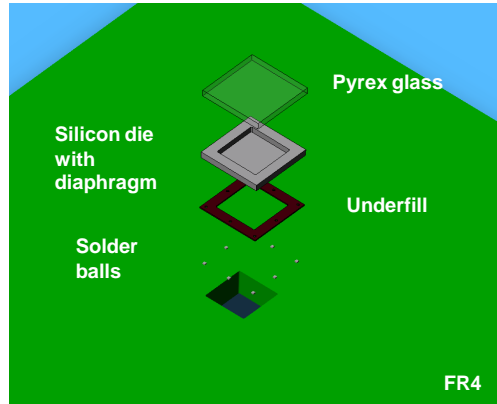


Figure 4.23: Simulation model. The pressure sensor consisting of silicon diaphragm and pyrex back cover is face-down attached with solder bumps on a PCB. The underfill ring seals the diaphragm from the outside.

may be due to the fact that there is an irreversible chemical reaction occurring between polymer and moisture such as formation of hydrogen bonds [68]. Some postulated that diffusivity is constant and moisture diffusion exhibits fickian behaviour for epoxy resins at lower temperature and environmental humidity levels such as 30 °C and 60 %RH [71].

First, moisture diffusion in the underfill was simulated by introducing a saturation concentration C_{sat} as the boundary value for the surfaces of the underfill in contact with the ambient air. This value is fixed by the environmental parameters temperature and relative humidity (see [68]). The used saturation concentration of 11.5 kg/m³ is a typical value for epoxy-based underfills. The inner boundaries are assumed to be protected from moisture. The simulation, based on transient analysis, shows how fast saturation is reached in the underfill if the device is subject to 85 °C and 85 %RH.

Figure 4.24 shows a plot of the moisture concentration in the underfill ring after three hours. Saturation has not yet been reached. At the inner edge of the underfill the concentration is 220 mol/m³ (which is equal to 4 kg/m³). In figure 4.25 the mass uptake is plotted as a function of time. The mass is the integral of the water concentration over the entire underfill volume.

These simulations give an idea about the time at which saturation is reached when the underfill is exposed to humidity. It is saturated after

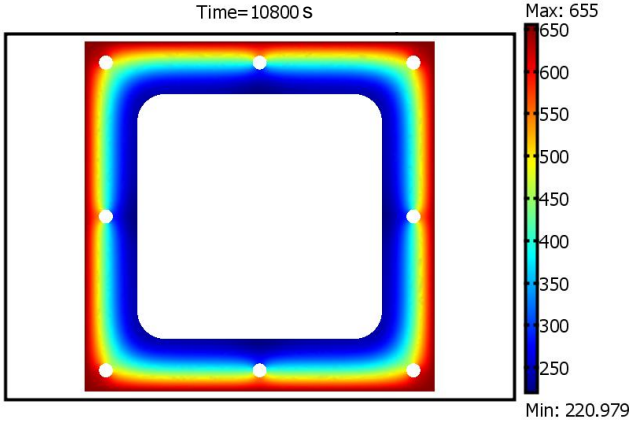


Figure 4.24: Plot of moisture concentration in the underfill ring after three hours. The saturation concentration $C_{sat} = 11.8 \text{ kg/m}^3 = 655 \text{ mol/m}^3$.

one day, when exposed to 85°C and $85\% \text{RH}$.

4.4.3 Hygro swelling

Due to the symmetry of the model only one quarter of the device has to be implemented and simulated. Hygro swelling and thermally induced stresses in elastic and isotropic materials are governed by the following equation:

$$\sigma_{ij} = \lambda \delta_{ij} (\epsilon_{11} + \epsilon_{22} + \epsilon_{33} - 3\alpha \Delta T - 3\beta C) + 2\mu \epsilon_{ij}. \quad (4.2)$$

σ_{ij} and ϵ_{ij} are the stress tensor and the strain tensor elements, respectively. δ_{ij} is the Kronecker symbol, α is the coefficient of thermal expansion (CTE), ΔT is the temperature change, β is the hygro swelling coefficient, and C is the moisture concentration. λ and μ are moduli and can be expressed by Young's Modulus E and Poisson's Ratio ν :

$$\lambda = \frac{\nu E}{(1 + \nu)(1 - 2\nu)}, \quad \mu = \frac{E}{2(1 + \nu)}. \quad (4.3)$$

Since the solder balls provide a strong mechanical connection between sensor and FR4, the underfill cannot swell freely in all directions, hence, the swelling induces stresses and strains in the device. As a consequence, the $50 \mu\text{m}$ thick diaphragm is deformed upwards. Figure 4.26

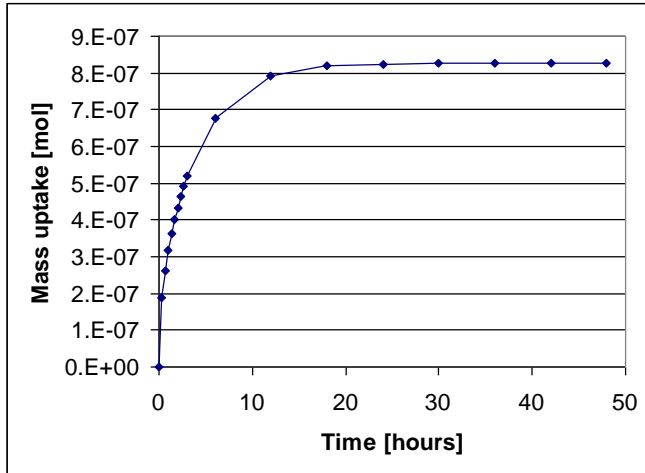


Figure 4.25: Evolution of the total moisture in the underfill.

is a 3D colour plot of the displacement in z-direction (perpendicular to diaphragm). The shown deformation is not to scale. Maximal deflection is reached in the centre of the diaphragm, corresponding to the symmetry of the device. Figure 4.27 shows the deflection along the diagonal of the diaphragm. The maximal deflection in the centre is 100 nm.

4.4.4 Comparison between hygro swelling and thermally induced deformation

Thermally induced stresses and strains are governed by equation (4.2) without the hygro swelling term $\beta \cdot C$.

In order to estimate the hygro swelling induced deformation, it was compared to deformations induced by a temperature change of the device. The assumed temperature change is 50 K. Figure 4.28 is a colour plot of the thermally induced deformation after the device was heated from 300 K to 350 K. The colour indicates the displacement in z-direction (perpendicular to diaphragm).

Figure 4.29 is a comparison of hygro swelling and thermally induced deformations along the diagonal of the diaphragm. The hygro swelling induced deformation of the diaphragm is presented by the green curve and is identical to the curve in figure 4.27. The thermally induced deformation of the diaphragm is presented by the red curve. The diaphragm

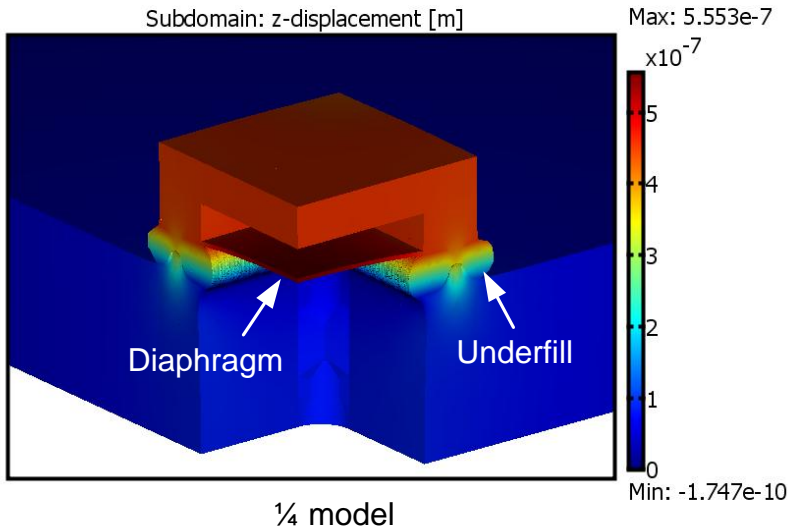


Figure 4.26: Colour plot of hygro swelling of the underfill. The swelling causes a deflection of the diaphragm. The deformation is not to scale.

is bent downwards. It is due to the large CTE of the FR4 substrate which expands stronger than the silicon or pyrex. The blue curve shows the deformation of a bare pressure sensor (silcon die and pyrex glass) heated from 300 K to 350 K. In contrast to the bonded sensor, the diaphragm is bent upwards, which is due to the fact that the pyrex cover has a larger CTE than the silicon die.

The simulations do not allow conclusions about the functionality of flip chip bonded pressure sensors, because the sensor model is strongly simplified. However, it is possible to estimate the influence of hygro swelling on a package. It is likely that the swelling changes the offset of the pressure sensor. Since piezoelectric pressure sensors have an intrinsic uncontrolled offset drift which requires periodic calibration, hygro swelling is not supposed to influence the performance of pressure sensors. The time scale of moisture diffusion is in the range of days, it should be possible to calibrate flip-chip bonded pressure sensors to compensate for both the intrinsic offset drift and the drift induced by hygro swelling of the underfill.

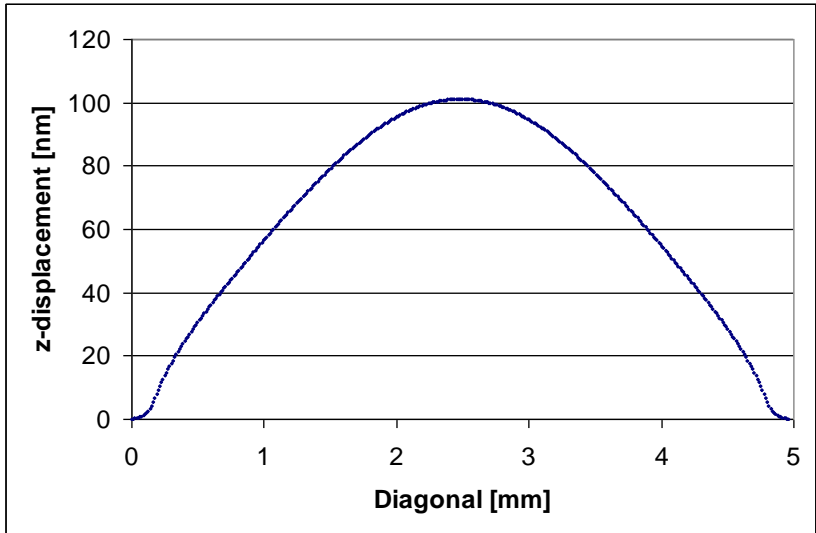


Figure 4.27: Simulations of hygro swelling induced deflection along the diagonal of the diaphragm.

4.4.5 Conclusions

Even though moisture diffusion in underfills is not exactly obeying Fick's law of diffusion, simulation of moisture diffusion based on the diffusion equation provides information on the time scale at which saturation happens.

According to the simulations, hygro swelling induced deformations can induce a time-dependent drift of the offset in the order of thermally induced shifts of the offset. However, the time scale of the diffusion allows compensation of the drift by a calibration procedure.

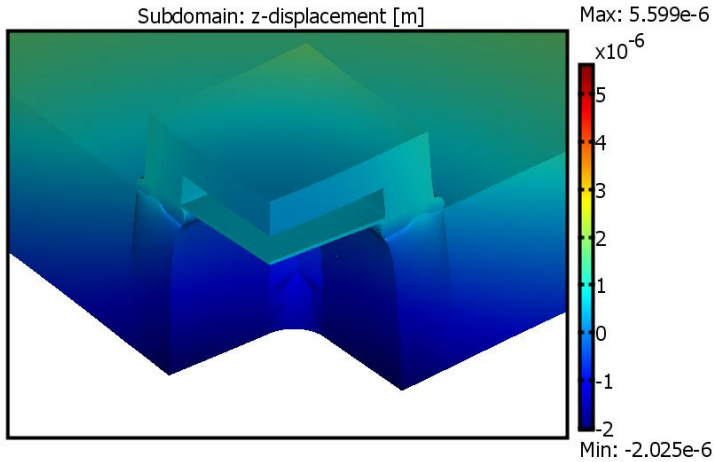


Figure 4.28: Colour plot of thermally induced deformation of the device. The diaphragm is bent downwards. The deformation is not to scale.

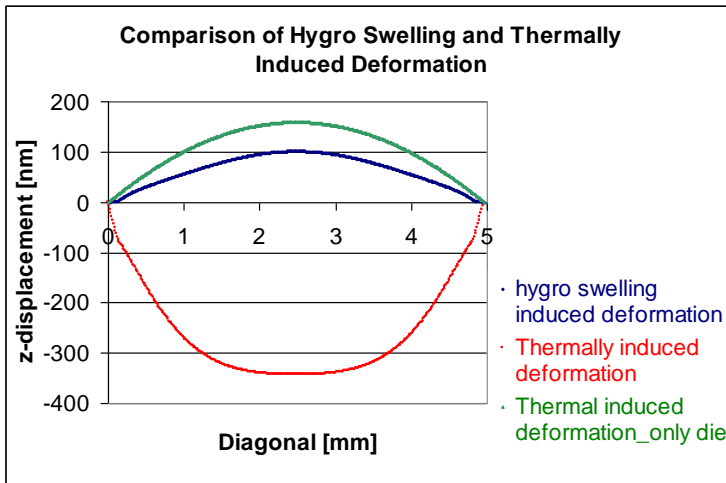


Figure 4.29: Diaphragm deflection induced by hygro swelling of the under-fill and by a mismatch of the CTEs of the components when subject to a temperature increase of 50 K.

	FR4	Solder balls	Underfill	Diaphragm	Silicon die	Pyrex
Dimensions [mm]						
Height	2	0.1	0.1	0.05	0.5	0.5
Width	arbitrary	0.2 \varnothing	5 \times 5	3.5 \times 3.5	5 \times 5	5 \times 5
Young's Modulus E [GPa]	22	68	2.6	170	170	70
Poisson's Ratio ν	0.4	0.4	0.4	0.28	0.28	0.2
CTE [ppm/K]	18 (in plane)	16	75	2.6	2.6	3.3
Diffusivity D [m^2/s]			14.7 $\times 10^{-12}$			
Hygro swelling β [m^3/kg]			4 $\times 10^{-4}$			
Moisture saturation C_{sat}						
at 85 °C/85 %RH [kg/m^3]						
			11.5			

Table 4.10: Material parameters used in the simulations of hygro swelling and thermomechanical stresses and strains. The material parameters of the underfill are from [68].

CASE II: Flow Sensor

5.1 Introduction

We here present a novel low-rate flow sensor for liquids with a targeted measurement range of $1 \mu\text{l/s}$. Due to the small physical dimensions of the sensor ($50 \text{ mm} \times 8 \text{ mm} \times 8 \text{ mm}$) it can be integrated in pipetting systems.

We developed and implemented a novel concept which uses the flip chip process presented in section 4.3 and the fact that a liquid flow induces a pressure drop (or vice versa) in a channel [72]. The sensor method is based on differential pressure measurement at two ends of a well defined fluidic microchannel. The pressures are directed to the two sides of one sensitive diaphragm-based differential pressure sensor.

Existing flow sensors are either based on two absolute pressure sensors or on heat conductance. The advantages of the here presented concept are the following:

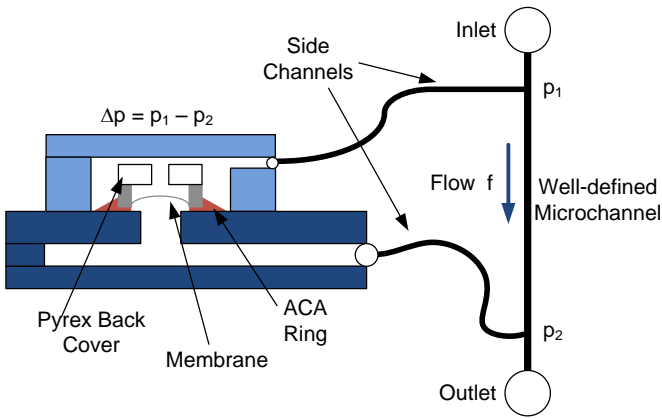
- The flow sensor is insensitive to high system pressures (e.g. 10 bar), because the single pressure sensor is exposed to the system pressure on both sides of its sensitive membrane.
- Since the pressure sensor membrane is entirely exposed to the system pressure, a very sensitive differential pressure sensor can be utilised.
- Compared to thermal based flow sensors the response time is faster and data processing is simpler.
- The flow sensor can basically be built with any commercially available pressure sensor die.

Liquid flow is measured in a variety of industries. Small liquid flow is particularly of interest in drug delivery, liquid handling, pump control / calibration, analytical instrumentation, lab-on-a-chip, molecular diagnostics and flow cytometry.

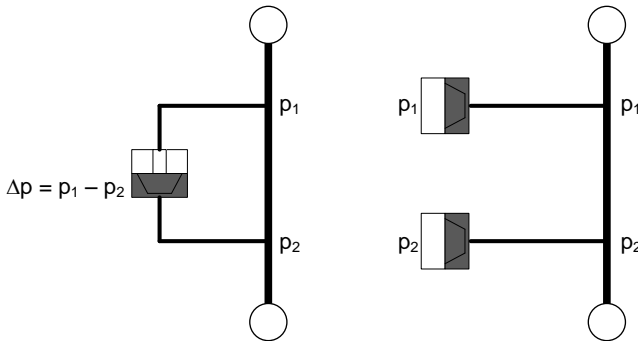
5.2 System design

5.2.1 Concept

The measurement principle is sketched in figure 5.1(a). A flow is driven through the well defined microchannel which produces a pressure difference $p_1 - p_2$ along the channel. Side channels guide the pressures to the



(a)



(b)

Figure 5.1: Novel flow sensor concept. The pressures at the inlet and outlet are directed to the front and back side of a differential pressure sensor which measures the pressure difference Δp (a). Subfigure (b) compares our concept with the existing concept which uses two absolute pressure sensors. The absolute sensors are subject to the system pressures p_1 and p_2 .

front and back side of the pressure sensor [72], instead of having two absolute pressure sensors at the ends of each side channel (see figure 5.1(b)). The advantage of our concept is that the differential pressure sensor is only subject to relatively small pressure differences, whereas in the latter design the absolute pressure sensors are subject to the absolute pressures p_1 and p_2 , respectively. Pressure peaks in the microchannel may destroy such sensors.

Furthermore, the flip chip approach reduces the dead volume of the cavity around the pressure sensor because wire bond connections are avoided. Devices with other packaging approaches than flip chip bonding suffer from large dead volumes in the cavity. High pressures in the system compress the air volume in the side channels. The liquid may reach the cavity and contaminate the sensor and promote corrosion of the sensor pads.

5.2.2 Governing equations

Assuming that the fluid is incompressible and the flow is laminar viscous, the pressure drop of a fluid in a long tube of length L and cross sectional lengths a and b is given by the Hagen-Poiseuille equation [73, 74]:

$$\frac{dV}{dt} = \dot{V} = \frac{K \cdot \min(a, b)^3 \cdot \max(a, b)}{12\eta L} \cdot \Delta p, \quad (5.1)$$

where K is given by:

$$K = 1 - \sum_{n=1}^{\infty} \frac{1}{(2n-1)^5} \frac{192}{\pi^5} \frac{\min(a, b)}{\max(a, b)} \tanh\left(\left(2n-1\right) \frac{\pi \max(a, b)}{2 \min(a, b)}\right) \quad (5.2)$$

\dot{V} is the volumetric flow rate, Δp is the pressure drop in the tube with length L , η is the dynamic viscosity. For $\min(a, b)$ and $\max(a, b)$ the smaller and larger value of a and b has to be chosen, respectively. The pressure drop scales with the cross sectional length to the 4th power.

The Hagen-Poiseuille equation is derived from the Navier-Stokes equation under the above stated assumptions. Equation (5.1) can be rearranged. Using:

$$R := \frac{12\eta L}{K \cdot \min(a, b)^3 \cdot \max(a, b)} \quad (5.3)$$

we can write:

$$\Delta p = R \cdot \dot{V}. \quad (5.4)$$

This equation corresponds to Ohm's law for electricity ($U = R \cdot I$). The voltage drop Δp is analogous to the electrical potential drop U (i.e. voltage) and the volumetric flow rate is analogous to the electrical current I .

The Hagen-Poiseuille equation (5.4) tells us that a well defined channel with length L and cross sectional area $a \cdot b$ imposes a resistance R to flow. The potential Δp is required to generate the volumetric flow rate \dot{V} .

Since the pressure drop is linearly dependent on the volumetric flow rate, a calibration process requires only two measurement points. In fact, one measurement point would be sufficient if the electrical output signal were zero for zero pressure drop. The inherent and random offset of the pressure sensors output signal requires a second measurement point. The second measurement point may be the offset at zero pressure drop (i.e. zero flow).

5.2.3 Design

The flow sensor consists of 4 parts with distinct functions:

- A differential pressure sensor which is face-down attached to the restriction module.
- The restriction module with the fluidic system. It provides fluidic and electrical connection to the pressure sensor.
- A PCB which provides fluidic and electrical connections to the outside world.

The *differential pressure sensor* MS3705-D from Intersema [43] was used. Its dimensions are $2.45 \text{ mm} \times 2.45 \text{ mm} \times 0.9 \text{ mm}$. It has aluminum contact pads at the peripherals of the top surface and a pyrex back cover with a hole to provide access to the membrane back side. The pressure range is $\pm 50 \text{ mbar}$ which corresponds to an output signal of $\pm 110 \text{ mV}$.

The *restriction module* consists of a pyrex and a silicon substrate anodically bonded together. It comprises the fluidic microchannel with inlet and outlet, side channels to the sensor, metal lines, and Au stud bumped contact pads. The microchannels are formed by sandblasting recesses in the back side of a pyrex substrate. The recesses are closed by

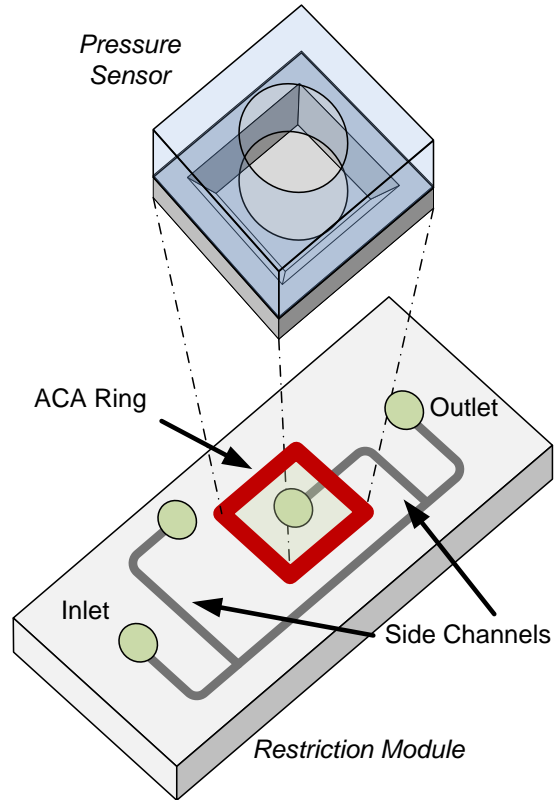


Figure 5.2: Flip chip assembly of a pressure sensor. The ACA ring covers the contact pads of the sensor which are located at the peripherals of the top surface and it seals the side channel with the opening under the sensor against the outside.

anodically bonding a silicon substrate of the same size to the pyrex substrate. Figure 5.2 depicts the design. The pressure sensor is face-down attached to the restriction module with ACA (see chapter 2), which forms a ring. It seals the side channel opening under the sensor against the outside. The opening of the second side channel needs to be connected to the opening of the pyrex cover of the sensor, as it is shown in figure 5.3.

The restriction module, in turn, is face-down attached to a FR4 *PCB* which accommodates also electrical components for signal processing. The macroscopic fluidic and electrical connections to the outside world are provided by the PCB, too. Figure 5.4 is a side view sketch of the complete device. It is feasible to employ FR4 not only as a carrier for electronic components, but also as a base plate for fluidic devices because fluidic structures are easily drilled in FR4.

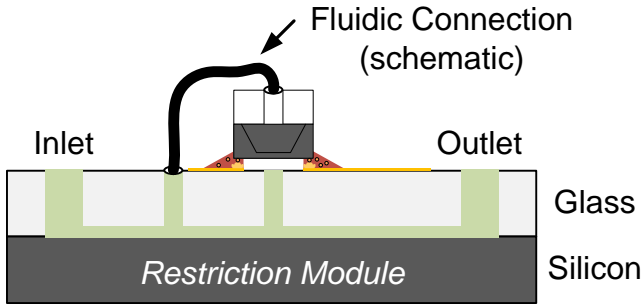


Figure 5.3: Side view sketch of restriction module and pressure sensor. The side channels are connected to front and back side of the pressure sensor.

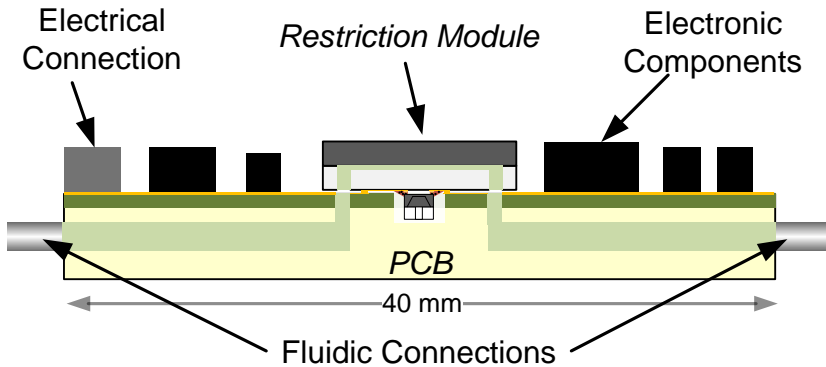


Figure 5.4: Side view sketch of the complete device. The PCB provides the macroscopic fluidic and electrical connections to the outside world.

The restriction module is required for two main reasons: It matches the CTE of the pressure sensor. Hence, temperature variations do not induce strains and stresses in the membrane. It was shown in chapter 2 that such a device works according to the specifications of the pressure sensor.

The second reason is the availability of technologies to manufacture microchannels in pyrex of $100\ \mu\text{m}$ width which is required to detect flow in the range of $1\ \mu\text{l/s}$.

The length of the microchannel is 22 mm long and has a square shaped cross section of 0.1 mm width. According to the Hagen-Poiseuille

equation (5.1) a pressure drop of 50 mbar (which is the measurement range of the used pressure sensor) corresponds to a volumetric flow rate of $0.8 \mu\text{l/s}$ for water with a dynamic viscosity of $1 \text{ mPa} \cdot \text{s}$ and $K = 0.4218$ for $a = b$. Doubling the width of the channel would increase the flow rate by a factor of 16. Apparently, manufacturing tolerances strongly influence the flow rate range and the sensitivity of the device.

5.3 Bonding procedures

Pressure sensor onto restriction module

The employed ACA-bonding process is identical to the process described in subsection 2.4.3 and employed in section 4.3. Gold studs are placed on the aluminum pads of the pressure sensor. They are then flattened to obtain smooth bumps of equal height. The ACA is dispensed in a way to cover the sensor pads at the peripherals of the top surface and to seal the membrane.

Restriction module onto PCB

The restriction module is face-down attached to the PCB with a compliant adhesive. The PCB has a cavity to accommodate the pressure sensor (see figure 5.4). The adhesive provides both mechanical connection and connection of the fluidic channels between restriction module and PCB. Figure 5.5 is photograph of an assembled device with electrical components for signal processing.

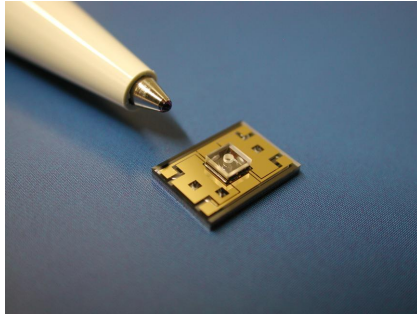
Final assembly step

An aluminum case will be used to protect the restriction module and the electrical components.

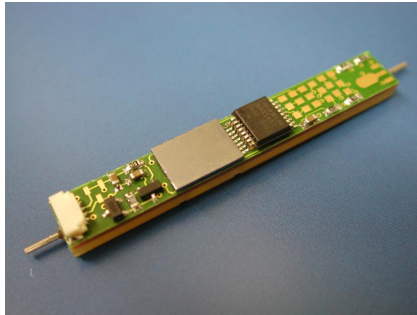
5.4 Characterisation

Since the flip chip process was already characterised in section 4.3, we here focus on the sensitivity and the flow rate range. Sensitivity S is defined as the ratio of change of the raw voltage output signal ΔU and the corresponding change in flow rate Δf :

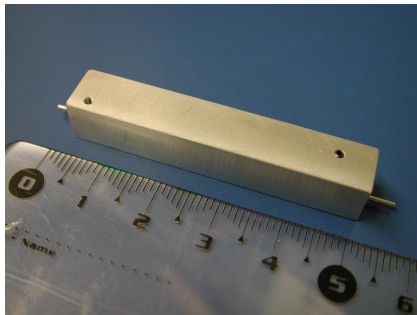
$$\text{Sensitivity } S = \frac{\Delta U}{\Delta f}. \quad (5.5)$$



(a)



(b)



(c)

Figure 5.5: Photographs of the restriction module (a), the assembled device with restriction module and read out electronics (b), and a flow sensor with an aluminum case (c).

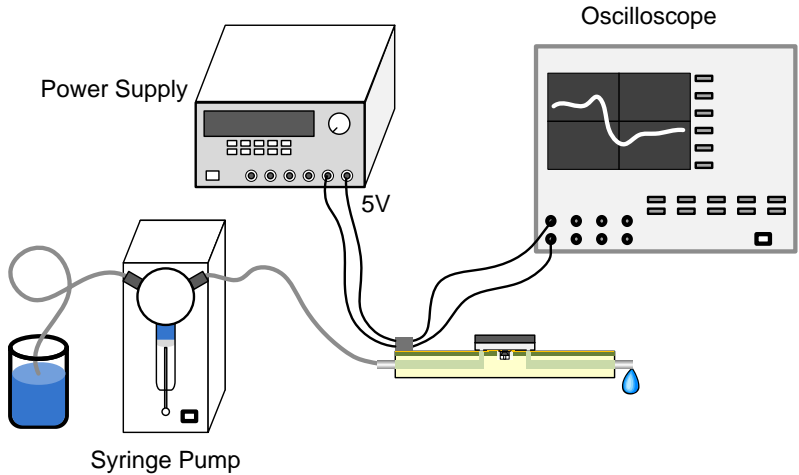


Figure 5.6: Measurement setup for characterisation of the flow sensor. The syringe pump provides a constant flow f while the oscilloscope reads the output signal.

The flow rate range is related to the output signal range by equation (5.5). The range in which the output signal responds linearly to the pressure drop is ± 110 mV according to the specifications of the pressure sensor.

Furthermore, we measured the response time which is the time period in which the output signal reaches the maximal value when a flow is abruptly switched on.

5.4.1 Measurement method and setup

Sensitivity measurements were carried out with the setup presented in figure 5.6. The inlet of the flow sensor is connected to a motorised syringe pump which allows adjustment of the flow. First, the pump sucks water from a reservoir. Then it has to switch a valve to generate a flow through the sensor by pushing forward the syringe piston. Due to the switching there is always some air in the syringe. When the syringe piston accelerates the air is compressed. Consequently, it takes several seconds until the flow becomes steady.

The pressure sensor die is driven with 5 V by a power supply. The output signal of the sensor is monitored and stored by an oscilloscope.

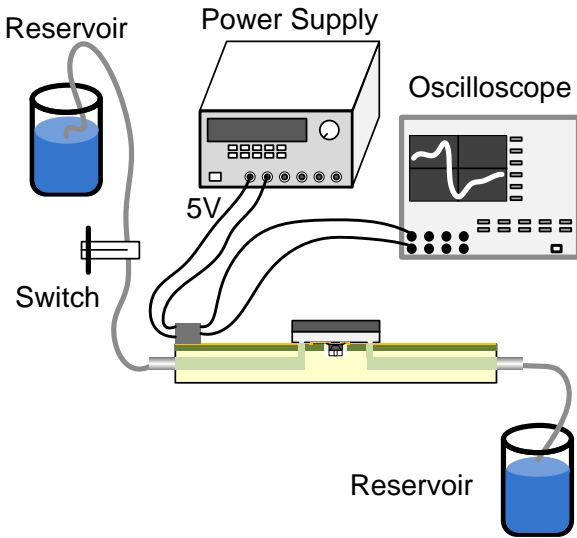


Figure 5.7: Measurement setup for characterisation of the flow sensor with two water reservoirs. The difference in potential energy of the two water reservoirs induces a flow as soon as the switch is opened.

Due to the above mentioned reason the syringe pump was not able to provide a sudden increase in flow which is required to measure the response time of the flow sensor. Therefore, two water reservoirs at different heights (difference in potential energy) were connected with the flow sensor in the connection line (see figure 5.7). This setup avoids air in the fluidic system. A switch is placed in the line. Quickly opening the switch causes an abrupt rise of the flow.

5.4.2 Sensitivity and flow rate range

Figure 5.8 shows the output signal of the fully packaged flow sensor when water is flowing through the microchannel. The sensor responds linearly to the applied flow. The measured sensitivity, which is defined as the slope of the linear curve, is $98.2 \text{ mV}/\mu\text{l/s}$. The full scale range of the pressure sensor is 110 mV , according to the data sheet. Hence, the full scale range of the flow sensor is $\dot{V}_r = 1.1 \mu\text{l/s}$, which deviates by 37.5% from the nominal value of $\dot{V}_n 0.8 \mu\text{l/s}$. This deviation is likely due to the channel width. Assuming that no other variations influence the measurement it is possible to calculate the deviation of the real microchannel width a_r to the nominal microchannel width a_n by applying the Hagen-Poiseuille equation (5.1):

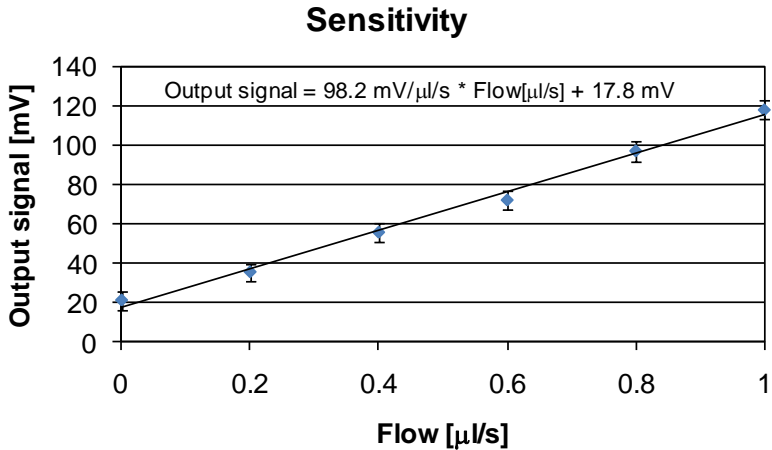


Figure 5.8: Output signal of the flow sensor as function of the flow. The sensor responds linearly to the flow. The sensitivity (slope of the linear curve) is 98 mV/ $\mu\text{l/s}$.

$$\frac{a_r^4}{a_n^4} = \frac{\dot{V}_r}{\dot{V}_n} = \frac{1.1}{0.8} = 1.38, \quad (5.6)$$

$$\Rightarrow a_r = 1.08 \cdot a_n.$$

This calculation shows that tolerances of the microchannel width are a critical issue. The real microchannel width is 8 % larger than it was designed. It is assumed that the sensitivity of the pressure sensor is not reduced by the package as showed in section 4.3. The flip chip bonded pressure sensors perform according to the specifications of the data sheet. However, the tolerances of the sensor dies are rather large (± 20 %, see table 4.9). Therefore, the influence of the package is negligible compared to the tolerances. Yet precise information of degradation of the performance can only be obtained by comparing sensitivity (and offset) values before and after bonding. Unfortunately, these values of the bare sensor dies are not provided by the manufacturer.

To conclude, there could be three reasons for the increased flow rate range (and hence decreased sensitivity). First, tolerances in the microchannel production. Second, tolerances in the sensitivity of the com-

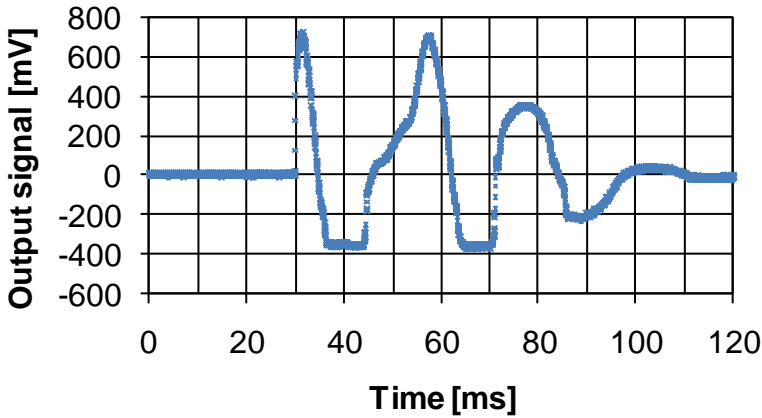


Figure 5.9: Output signal of the flow sensor corresponding to a pressure peak in the inlet tube. A hammer stroke on the inlet tube generates a sudden pressure increase and flow in the microfluidic system. The output signal peaks are due to the flow, as explained in the text.

mercial sensor dies, and third, influence of the package. Nevertheless, the flow sensor shows a high sensitivity and a flow rate range close to the aimed range.

Preliminary tests were carried out to test the insensitivity of the flow sensor to high pressures. A hammer stroke on the inlet tube should simulate a pressure peak in the microfluidic system. Figure 5.9 shows the output signal of the flow sensor corresponding to a hammer stroke. Due to a lack of pressure transducers with a sufficiently large pressure range the absolute pressure in the microfluidic system could not be measured. We believe that the output signal variation is induced by a flow in the microchannel and not by a propagating pressure signal: To depict this, a small calculation is done: If we assume that the first (positive) signal peak is induced by the pressure peak hitting the front side of the membrane, and that the first negative signal peak is induced by the pressure peak hitting the back side of the membrane, then the negative signal peak is delayed by the time the pressure signal requires to travel the additional distance. This additional distance corresponds to a delay of 10 ms (see figure 5.9). The speed of sound in water is 1500 m/s. Hence, the additional distance is $\text{speed} \cdot \text{time} = 15 \text{ m}$. This simple calculation

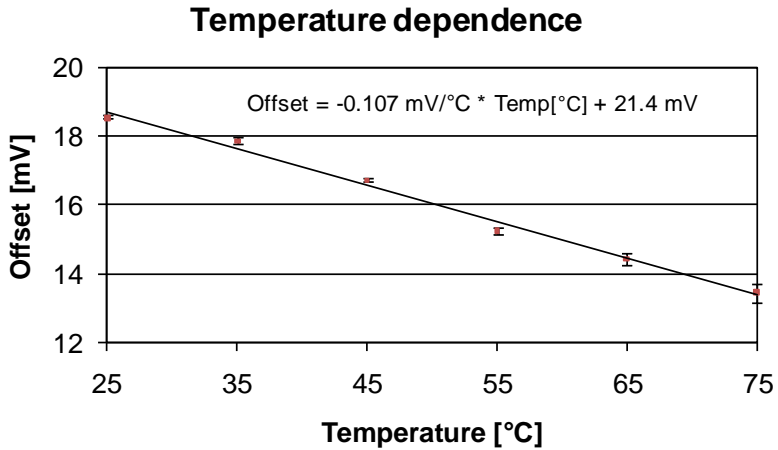


Figure 5.10: Offset as function of the temperature. The slope of the linear curve is the temperature coefficient of offset (TCO) and equals $-107 \mu\text{V}/^\circ\text{C}$.

shows that differences of the lengths of the traveling paths (e.g. due to fabrication tolerances) cannot be the reason for the measured output signal variations.

5.4.3 Temperature dependence of offset

Figure 5.10 depicts the temperature dependence of the offset which linearly decreases with increasing temperature. The temperature coefficient of offset (TCO) is $-107 \mu\text{V}/^\circ\text{C}$. Comparing this value with the specified TCO (see table 3.3 on page 55) and the TCO of flip chip bonded pressure sensors presented in section 4.3, we come to the conclusion that the flow sensor package has only a small influence on the performance of the pressure sensor. We believe it is due to the CTE mismatch between PCB and the silicon based restriction module and pressure sensor. For comparison, the TCOs for die-bonded and flip chip bonded devices and for the flow sensor are listed in table 5.1.

5.4.4 Response time

The setup from figure 5.7 provides a fast build up of the flow when the switch is opened. Figure 5.11 is a graph that shows the increase of the

Package	TCO [$\mu\text{V}/^\circ\text{C}$]
Data sheet	-40 ± 40
Standard bonding	-24 ± 10
Flip chip bonding with ACA	from -36 to -67
Flow sensor	-107

Table 5.1: Comparison of the temperature coefficients of offset (TCO) of the pressure sensor bonding procedures presented in this thesis.

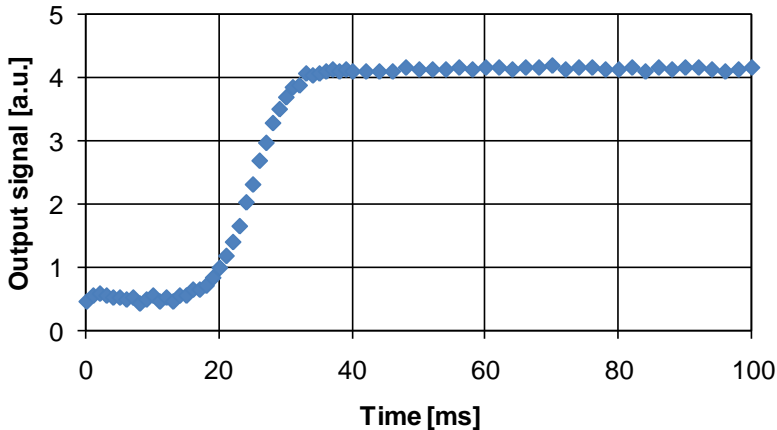


Figure 5.11: Measurement setup for characterisation of the flow sensor. The syringe pump provides a constant flow while the oscilloscope reads the output signal.

signal after the switch was opened. Continuous and constant flow is reached within 10 ms. The build up of the flow is not exactly a step function. Therefore, the measured response time has to be considered as an upper limit of the real response time.

We believe that the response time is limited due to the inertia of the fluid. When the switch is opened the water is accelerated by the gravitational force (i.e. the pressure drop is induced by gravity). The Hagen-Poiseuille equation (5.1) only describes steady-states.

5.5 Conclusions

The here presented novel concept with only one differential pressure sensor has superior properties compared to flow sensors with two wire bonded absolute pressure sensors at each end of the side channels and to thermal mass flow sensors.

- Differential pressure sensors are more sensitive because they work in a small range around 0 bar pressure difference. Absolute pressure sensors are pre-stressed because they have an evacuated chamber behind the membrane and are therefore less sensitive to pressure.
- Our sensor is insensitive to high system pressures because the differential pressure sensor is exposed to the system pressure on both sides of the membrane. Only the pressure drop acts on the membrane.
- Thermal mass flow sensors are equally sensitive but have response times in the range of 40 ms [75].
- The flip chip assembly with ACA proved to be very useful. It offers several advantages over standard face-up bonding and wire bonding of pressure sensors.
 - Smaller and more compact packages are feasible.
 - Large dead volumes at the back side of the sensor as well as wire bonds can be avoided.
 - The bonding method matches the needs of MEMS packaging. The flip chip bonded pressure sensors perform according to the specifications of the pressure sensor, as was already proven in section 4.3.

The FR4 base plate accommodates electronic components and part of the fluidic system. Availability and existing processes to machine FR4 boards make it a good choice as a base material.

The sensitivity of the flow sensor is in the range of $98 \text{ mV}/\mu\text{l/s}$. The output range of the pressure sensor of $\pm 110 \text{ mV}$ determines the maximal measurable flow rate which is $\pm 1.1 \mu\text{l/s}$. The small discrepancy to the nominal flow rate range of $0.8 \mu\text{l/s}$ is attributed either to tolerances in the microchannel fabrication, tolerances in the sensitivity of the sensor, or the influence of the package. However, sensitivity is excellent

and both sensitivity and flow rate range of the first prototype met our expectations.

An upper limit for the response time of the flow sensor of 10 ms was found, this in comparison to the response time of the pressure sensor of 1 ms. Due to the limitations of the measurement set-up it can be expected that the response time of the flow sensor is effectively lower than 10 ms.

Conclusions and Outlook

6

6.1 Conclusions

In this thesis, flip chip bonding technologies were investigated in terms of electrical performance and applicability of the bonding processes. A ACA-bonding process was developed which is suited for low T_g material substrates and MEMS devices.

ACA bonding proved to be advantageous over the other bonding techniques because it provides good electrical contacts and mechanical strength avoiding high temperature loads and forces on the device during the bonding process. Furthermore, dispensing tools with an accuracy of no better than $100\ \mu\text{m}$ are sufficient to produce ACA structures so that it can seal sensing elements of chips against the outside world.

Standard bonding of pressure sensors was characterised and successfully used in a pressure strip for non-invasive measurement of flows and pressures on arbitrarily shaped aerodynamic bodies. Sensitivity and temperature dependence of these devices are a benchmark for flip chip bonded pressure sensors.

The developed ACA-bonding process was successfully applied to low T_g materials especially suited for microfluidic applications such as lab-on-a-chip and liquid handling. At present, reliability and resistance to autoclaving are still low due to a high CTE mismatch between the components.

The ACA process was also successfully applied to a MEMS device. In our case it is a diaphragm-based differential pressure sensor which is sensitive to stresses and strains by nature. *The ACA process is hence a generic approach to MEMS packaging.*

The ACA process is also the key element in the package of the flow sensor presented in this thesis. The ACA approach avoids large dead volumes in the fluidic system. The flow sensor is highly sensitive to liq-

uid flows while being protected from high system pressures (e.g. 10 bar)

6.2 Outlook

The ACA process with pressure sensors requires dispensing of precise amounts of ACA. Mainly the height of the dispensed ACA decides whether bonding was successful or not. If the ACA lines are too high it may flow below the membrane of the sensor.

Alternatively, anisotropic conductive films could be employed. These films have a well-defined thickness and are laminated. The film could be structured before or after lamination. One could even think of laminating and structuring an entire wafer before dicing.

Anisotropic conductive adhesives might be spin coated on the wafer.

The pressure strip uses standard-bonded pressure sensors. The FR4 board is large and thick due to the wire bonds which need to be protected by side walls and silicone gel from environmental and mechanical impact.

The flip chip approach with ACA has the potential to drastically reduce the size of the package. Neither side walls nor silicone gel are needed because the bond is mechanically strong. The flip chip interconnects are protected by the ACA.

A higher level of integration could be reached by employing foil-based substrates, as described in section 3.6. Pressure sensor dies can be thinned below 100 μm and completely buried in the foil. A sandwich-structure (polyimide foil – embedded sensors and electronic components – polyimide foil) provides protection of the sensors and mechanical flexibility of the film. The ACA-bonding process could be a key process for the realisation of highly integrated pressure sensing foils.

Potential markets for pressure sensing foils include testing environments (e.g. wind tunnels) in automotive, aerospace, wind turbines, and watercraft industries.

The capability of flip chip bonding highly sensitive sensor dies (e.g. diaphragm-based differential pressure sensors) can have an impact on applications in life sciences where handling of very small liquids is a major issue. The flow sensor could be used to regulate the flow of a micropump or it could even be integrated in a lab-on-a-chip device.

4-Point Measurement Error Estimation



Using the values listed in table 2.1, the error of the measurement due to the 4-point setup can be calculated. For convenience, we rewrite: $R_W + R_C + R_L =: R_a$ and $U_W + U_C + U_L =: U_a$. Using Kirchhoff's laws and figure 2.8, we find the relations:

$$U_B = -U_M - 2 \cdot U_a - U_{TL} - U_B, \quad I_A = I_B + I_M, \quad (\text{A.1})$$

and

$$\frac{U_B}{U_M} = -1 - \frac{2 \cdot U_a + U_{TL} + U_B}{U_M} = -1 - \frac{2 \cdot R_a + R_{TL} + R_B}{R_M}, \quad (\text{A.2a})$$

$$\frac{I_A}{I_B} = \frac{I_B + I_M}{I_B} = 1 + \frac{R_B}{R_M + 2 \cdot R_a + R_{TL} + R_B}. \quad (\text{A.2b})$$

If we combine the equations (A.2a) and (A.2b) and the resistance values from table 2.1, we find an expression for the ratio of true and measured resistances:

$$\begin{aligned} \frac{R_B}{R_{\text{Measure}}} &\stackrel{2.1,2.2}{=} -\frac{U_B}{U_M} \cdot \frac{I_A}{I_B} \\ &= \left(1 + \frac{2 \cdot R_a + R_{TL} + R_B}{R_M}\right) \cdot \left(1 + \frac{R_B}{R_M + 2 \cdot R_a + R_{TL} + R_B}\right) \\ &\simeq (1 + 4 \cdot 10^{-7}) \cdot (1 + 10^{-9}) \\ &\simeq (1 + 4 \cdot 10^{-7}). \end{aligned} \quad (\text{A.3})$$

Rearranging this equation provides the result of equation (2.3). \square

Number of spheres within a contact in ACA bonding

B

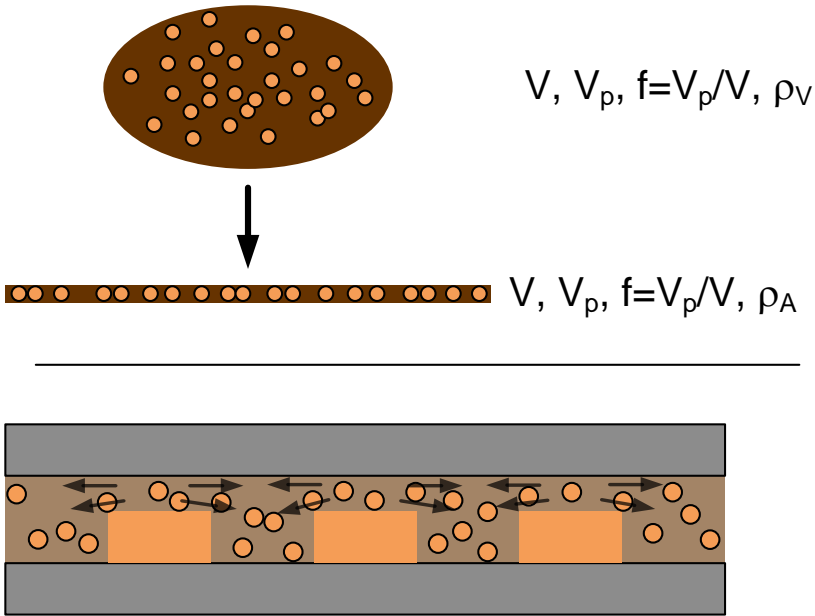


Figure B.1: ACA-spheres within a contact surface. The number of particles per surface ρ_A can be calculated from the volume fraction f of the spheres in the ACA and their average diameter d (upper drawing). The number of spheres within the contact surface is lower than expected from the particle density because of ACA flow during bonding (lower drawing).

If a drop of ACA is squeezed to a layer with the thickness of the average bump diameter d , the number of particles per surface ρ_A can be calculated from the number of spheres per volume ρ_V . For the volume fraction f of the spheres in the ACA, the number of spheres per volume ρ_V , and the number of spheres per surface ρ_A we find the expressions:

$$f = \frac{V_p}{V} = \frac{N \cdot v}{A \cdot d}, \quad (\text{B.1a})$$

$$\rho_V = \frac{N}{V} = \frac{N}{A \cdot d}, \quad (\text{B.1b})$$

$$\rho_A = \frac{N}{A}. \quad (\text{B.1c})$$

V_p is the volume of N spheres in a drop of ACA with the Volume V . v is the average volume of a sphere, A is the surface and d is the thickness (and the average diameter of a sphere) of the squeezed ACA. Substituting the expression for ρ_V and ρ_A in equation (B.1a), we find the following equation:

$$\frac{N \cdot v}{A \cdot d} = \rho_V \cdot v = \rho_A \cdot \frac{v}{d}. \quad (\text{B.2})$$

Solving for ρ_A provides

$$\rho_A = d \cdot \rho_V. \quad (\text{B.3})$$

However, the number of particles per surface ρ_A is not equal to the number of particles per contact area (with respect to the same surface). One reason is the ACA flow during bonding, as it is depicted in the lower drawing of figure B.1. The spheres flow into the spaces between the stud bumps [21, 76]. The number of spheres within the contact surface is reduced.

$$\rho \leq \rho_A. \quad (\text{B.4})$$

Strictly speaking, this is only true if the spheres are arranged in an array. Due to the random distribution of the spheres in the employed ACA, the number of spheres per contact surface ρ can even be bigger than the average number of spheres per surface ρ_A .

Bibliography

- [1] T. R. Hsu, “*MEMS packaging*”, Inspec, 2004
- [2] J. H. Lau, “*Flip chip technologies*”, McGraw-Hill, 1996
- [3] W. D. Callister, Jr., “*Fundamentals of materials science and engineering; an integrated approach, chapter 17: Thermal properties*”, John Wiley & Sons Inc., 2nd Edition, 2005
- [4] E. Suhir, “*Micro- and opto-electronic materials and structures, Vol. 2, chapter 1: Analytical thermal stresses modeling in physical design for reliability of micro- and opto-electronic systems: role attributes, challenges, results*”, Springer, 2007
- [5] C. A. Harper, “*Electronic packaging and interconnection handbook*”, McGraw-Hill, 3rd Edition, 2000
- [6] G. Carson, M. Todd, “*Underfill technology – from current to next-generation materials*”, Advanced Packaging, may/june 2006, pp. 44-45
- [7] X. F. Ang et al., “*Temperature and pressure dependence in thermocompression gold stud bonding*”, Thin Solid Films, 504, pp. 379-383(2006)
- [8] S-Y. Kang, P. M. Williams, Y-C. Lee, “*Modeling and experimental studies on thermosonic flip-chip bonding*”, IEEE Transactions on Components, Packaging, and Manufacturing Technology B, Vol. 18, No. 4, pp. 728-733(1995)
- [9] Henkel AG and Co. KGaA, www.henkel.com, no-flow underfill for thermocompression: Hysol FP5001
- [10] N. R. Basavanahally et al., “*Direct chip interconnect with adhesive-connector films*”, Proceedings of the 42nd Electronic Components and Technology Conference, 18-20 May, pp. 487-491(1992)
- [11] J. Liu, “*ACA bonding technology for low cost electronics packaging applications–current status and remaining challenges*”, Soldering & surface mount technology, 13/3, pp. 39-57(2001)

- [12] J-K. Lin et al., “*Conductive polymer bump interconnects*”, Proceedings of the 46th Electronic Components and Technology Conference, 28-31 May, pp. 1059-1068(1996)
- [13] K. W. Oh, C. H. Ahn, K. P. Roenker, “*Flip-chip packaging using micromachined conductive polymer bumps and alignment pedestals for MOEMS*”, IEEE Journal of Selected Topics in Quantum Electronics, Vol. 5, No. 1, pp. 199-126(1999)
- [14] H. Cong, T. Pan, “*Photopatternable conductive PDMS materials for microfabrication*”, Advanced Functional Materials, 18, pp. 1912-1921(2008)
- [15] L. F. Miller, “*Controlled collapse reflow chip joining*”, IBM Journal of Research and Development, Vol. 13, Issue 3, pp. 239-250(1969)
- [16] G. Harman, “*Wire bonding in microelectronics: materials, processes, reliability, and yield*”, McGraw-Hill, 2nd Edition, 1997
- [17] J. H. Lau (Editor), R. Sharma, R. Subrahmanyam, “*Flip chip technologies, chapter 3: Solder-bumped flip chip interconnect technologies: materials, processes, performance, and reliability*”, McGraw-Hill, 1996
- [18] T. B. Massalski, “*Binary alloy phase diagrams*”, Vol. 1, American Society of Metals, 1986
- [19] W. D. Callister, Jr., “*Fundamentals of materials science and engineering; an integrated approach*”, John Wiley & Sons Inc., 2nd Edition, 2005
- [20] M. Hutter, G. Engelmann, H. Oppermann, “*Betrachtung von galvanisch erzeugten AuSn-Bumps unter geometrischen Gesichtspunkten und die Auswirkungen auf den Bumpingprozess und die Flip-Chip-Montage*”, ITG-Workshop Photonische Aufbau- und Verbindungstechnik, May 15-16, 2003, Wernigerode
- [21] J. H. Lau (Editor), I. Watanabe, N. Shiozawa, K. Takemura, T. Ohta, “*Flip chip technologies, chapter 9: Flip chip interconnection technology using anisotropic conductive adhesive films*”, McGraw-Hill, 2nd Edition, 1997
- [22] D. D. Chang, P. A. Crawford, J. A. Fulton, R. McBride, M. B. Schmidt, R. E. Sinitiski, C. P. Wong, “*An overview and evaluation of anisotropically conductive adhesive films for fine pitch electronic*

- assembly*”, IEEE Transactions on Components, Hybrids, and Manufacturing Technology, Vol. 16, No. 8, pp. 828-835(1993)
- [23] J. H. Lau (Editor), H. Date, Y. Hozumi, H. Tokuhira, M. Usui, E. Horikoshi, T. Sato, “*Flip chip technologies, chapter 8: Anisotropic conductive adhesive for fine pitch flip chip interconnects*”, McGraw-Hill, 2nd Edition, 1997
- [24] Y. Huang, X. Gong, T. Bruemmer, S. K. Khanna, W J. Chappell, “*Magnetically aligned anisotropic conductive adhesive for high-frequency interconnects*”, IEEE MTT-S International Microwave Symposium Digest, June 2005, pp. 861-864,
- [25] K. Ishibashi, J. Kimura, “*A new anisotropic conductive film with arrayed conductive particles*”, IEEE Transactions on Components, Packaging, and Manufacturing Technology-Part B, Vol. 19, No. 4, pp. 752-757(1996)
- [26] L. Maiocco, D. Smyers, P. R. Munroe, I. Baker, “*Correlation between electrical resistance and microstructure in gold wirebonds on aluminum films*”, IEEE Transactions on Components, Hybrids, and Manufacturing Technology, Vol. 13, No. 3, pp. 592-595(1990)
- [27] A. Syed, “*Accumulated creep strain and energy density based thermal fatigue life prediction models for SnAgCu solder joints*”, IEEE Proceedings of the 54th Electronic Components and Technology Conference, Vol. 1, Issue 1, 1-4 June 2004, pp. 737-746
- [28] A. Schubert, R. Dudek, E. Auerswald, A. Gollhardt, B. Michel, H. Reichel, “*Fatigue life models for SnAgCu and SnPb solder joints evaluated by experiments and simulation*”, IEEE Proceedings of the 53rd Electronic Components and Technology Conference, 27-30 May 2003, pp. 603-610
- [29] A. Syed, “*Updated life prediction models for solder joints with removal of modeling assumptions and effect of constitutive equations*”, IEEE Proceedings of the 7th International Conference on Thermal, Mechanical and Multiphysics Simulation and Experiments in Micro-Electronics and Micro-Systems, EuroSime2006, 24-26 April 2006, pp. 639-647
- [30] H. Oppermann, M. Hutter, M. Klein, G. Engelmann, M. Toepper, J. Wolf, “*Flip chip reliability of GaAs on Si thinfilm substrates using AuSn solder bumps*”, Proceedings of the Materials Research Society Symposium B, Vol. 863, Spring 2005, pp. B10.1.1-B10.1.12

- [31] Y. T. Lai, C. Y. Liu, “*Study of wetting reaction between Eutectic AuSn and Au foil*”, Journal of Electronic Materials, Vol. 35, No. 1, pp. 28-34(2006)
- [32] M. Chin, K. A. Iyer, S. J. Hu, “*Prediction of electrical contact resistance for anisotropic conductive adhesive assemblies*”, IEEE Transactions on Components and Packaging Technologies, Vol. 27, No. 2, pp. 317-326(2004)
- [33] N. Schmid, M. Fretz, S. Bitterli, T. Burch, L. Neumann, J. Auerwald, H. F. Knapp, S. Graf, C. Bosshard, P. Sollberger, F. Zimmermann, Z. Stössel, T. G. Harvey, J. Zhu, R. Hamza, “*Pressure sensing strip for rapid aerodynamic testing*”, CSEM annual scientific report, p. 97(2007)
- [34] M. Fretz, N. Schmid, T. G. Harvey, J. Zhu, A.-C. Pliska, C. Bosshard, “*Pressure sensing strip - packaging aspects*”, CSEM annual scientific report, p. 98(2007)
- [35] www.scanivalve.com
- [36] M. Zagnoni, A. Golfarelli, S. Callegari, A. Talamelli, V. Bonora, E. Sangiorgi, M. Tartagni, “*A non-invasive capacitive sensor strip for aerodynamic pressure measurement*”, Sensors and Actuators A, 123-124, pp. 240-248 (2004)
- [37] W. T. Chen, C. W. Nelson, “*Thermal stress in bonded joints*”, IBM Journal of Research and Development, Vol. 23, No. 2, pp. 179-188(1979)
- [38] E. Suhir, “*Interfacial stresses in bimetal thermostats*”, Journal of Applied Mechanics, Vol. 56, pp. 595-600(1989)
- [39] J. C. Glaser, “*Thermal stresses in compliantly joined materials*”, Journal of Electronic Packaging, Transactions of the ASME, Vol. 112, pp. 24-29(1990)
- [40] E. Suhir, “*Predicted thermal stresses in a bimaterial assembly adhesively bonded at the ends*”, Journal of Applied Physics, Vol. 89, No. 1, pp. 120-129(2001)
- [41] J. K. Reynolds, D. Catling, R. C. Blue, N. I. Maluf, T. Kenny, “*Packaging a piezoresistive pressure sensor to measure low absolute pressures over a wide sub-zero temperature range*”, Sensors and Actuators A, 83, pp. 142-149(2000)

- [42] M. Röllig, S. Wiese, K.-J. Wolter, “*Extraction of material parameters for creep experiments on real solder-joints by FE analysis*”, IEEE Proceedings of the 7th International Conference on Thermal, Mechanical and Multiphysics Simulation and Experiments in Micro-Electronics and Micro-Systems, EuroSime2006, 24-26 April 2006, pp. 281-289
- [43] www.intersema.ch
- [44] www.sensortechnics.com
- [45] M. S. Zarnik, D. Rocak, S. Macek, “*Residual stresses in a pressure-sensor package induced by adhesive material during curing: a case study*”, Sensors and Actuators A, 116, pp. 442-449(2004)
- [46] N. Schmid, M. Fretz, H. F. Knapp, T. Burch, S. Bitterli, C. Bosshard, F. Zimmermann, P. Sollberger, T. G. Harvey, “*Towards integrated hybrid microsystems: flexible distributed pressure sensing strips*”, Proceedings of the 3rd European Conference & Exhibition on integration issues of miniaturized systems – MEMS, MOEMS, Ics, and electronic components, SMART SYSTEM INTEGRATION, Brussels, March 10–11, 2009
- [47] J. Mallon, J. Bryzek, J. Ramsey, G. Tomblin, F. Pourahmadi, “*Low-cost, high volume packaging techniques for silicon sensors and actuators*”, Solid-State Sensors and Actuator Workshop, IEEE (1998)
- [48] J. Gavillet, S. Getin, E. Quesnel, S. Martin, G. Delapierre, K. Hiller, J. Nestler, T. Gessner, J. Soechtig, G. Voirin, L. Buergi, J. Auerswald, H. F. Knapp, S. Ross, S. Bigot, M. Ehrat, A. Lieb, M.-C. Beckers, D. Dresse, “*Nanostructured polymer thin films – application to biosensors*”, Materials Science Forum, Vol. 570, pp. 10-17(2008)
- [49] J. Auerswald, H. F. Knapp, “*Quantitative assessment of dielectrophoresis as a micro fluidic retention and separation technique for beads and human blood erythrocytes,*”, Microelectronic Engineering, Elsevier, Vol.67-68, pp. 879-886(2003)
- [50] J. F. L. Goosen, “*Design considerations for silicon sensors for use in catheters and guide wires*”, Smart Materials and Structures, 11, pp. 804-812(2002)
- [51] Patent: US5074947, “*Flip chip technology using electrically conductive polymers and dielectrics*”, 1991

- [52] Patent: US5611140, “*Method of forming electrically conductive polymer interconnections on electrical substrates*”, 1997
- [53] Patent: DE102005037948A1, “*Sensoranordnung mit einem Sensorbauelement und einem Träger und Verfahren zur Herstellung einer Sensoranordnung*”, 2005
- [54] F. Campabadal, J. L. Carreras, E. Cabruja, “*Flip-chip packaging of piezoresistive pressure sensors*”, *Sensors and Actuators A*, Vol. 132, Issue 1, pp. 415-419(2006)
- [55] L. Li, J. E. Morris, “*Reliability and failure mechanism of isotropically conductive adhesives joints*”, *Proceedings of the 45th Electronic Components and Technology Conference*, 1995, pp. 114-120
- [56] K. W. Oh, C. H. Ahn, “*Flip chip packaging with micromachined conductive polymer bumps*”, *Proceedings of the 3rd International Conference on Adhesive Joining and Coating Technology in Electronics Manufacturing*, 1998, pp. 224-228
- [57] K. W. Oh, C. H. Ahn, K. P. Roenker, “*Flip-chip packaging using micromachined conductive polymer bumps and alignment pedestals for MOEMS*”, *IEEE Journal of Selected Topics in Quantum Electronics*, Vol. 5, Issue 1, pp. 119-126(1999)
- [58] R. S. Pai, K. M. Walsh, “*The viability of anisotropic conductive film as a flip chip interconnect technology for MEMS devices*”, *Journal of Micromechanics and Microengineering*, Vol. 15, No. 6, pp. 1131-1139(2005)
- [59] G-w. Xiao, P. C. H. Chan, A. Teng, J. Cai, M. M. F. Yuen, “*A pressure sensor using flip-chip on low-cost flexible substrate*”, *Proceedings of the 51st Electronic Components and Technology Conference*, 2001, pp. 750-754
- [60] M. Fretz, J. Auerswald, T. G. Harvey, J. Zhu, N. Schmid, C. Bosshard, “*Flip-chip bonding of sensor dies on PMMA for low-cost microfluidic applications*”, *Proceedings of the 1st European Conference on Microfluidics – Microfluidics 2008*, Bologna, December 10-12, 2008
- [61] T. Nguyen, E. Byrd, D. Alsheh, W. McDonough, J. Seiler, “*Interfacial water and adhesion loss of polymer coatings on a siliceous substrate*”, *Proceedings of the Materials Research Society Symposium*, Vol. 385, April 18-20, 1995, pp. 57-63

- [62] M. Fretz, “*Simulation of hygro swelling induced stresses in flip chip interconnects in a stress-sensitive chip-on-board configuration*”, CD-Proceedings of COMSOL Conference, Grenoble, October 2007
- [63] E. H. Wong, R. Rajoo, S. W. Koh, T. B. Lim, “*The mechanics and impact of hygroscopic swelling of polymeric materials in electronic packaging*”, Journal of Electronic Packaging, Vol. 124, Issue 2, pp. 122-126(2002)
- [64] F. G. Yost, M. M. Karnowsky, W. D. Drotning, J. H. Gieske, “*Thermal expansion and elastic properties of high gold-tin alloys*”, Metallurgical and Materials Transactions A, Vol. 12, No. 7, pp. 1885-1889(1990)
- [65] D. P. Rucker, S. G. Bike, “*Rheological properties of silica filled poly (methyl methacrylate)*”, Proceedings of the Materials Research Society Symposium, Vol. 385, 1995, pp. 173-178
- [66] J. H. Okura, A. Dasgupta, J. F. J. M. Caers, “*Hygro-mechanical durability of underfilled flip-chip-on-board (FCOB) interconnects*”, Journal of Electronic Packaging, Vol. 124, Issue 3, pp. 184-187(2002)
- [67] C. Y. Yin, H. Lu, C. Bailey, Y. C. Chan, “*Moisture effects on the reliability of anisotropic conductive films*”, IEEE Proceedings of the 6th International Conference on Thermal, Mechanical and Multiphysics Simulation and Experiments in Micro-Electronics and Micro-Systems, EuroSime2005, 18-20 April 2005, pp. 162-167
- [68] T. P. Ferguson, “*Moisture and interfacial adhesion in microelectronic assemblies*”, Ph.D. Thesis, Georgia Institute of Technology, Atlanta, Georgia, June 2004
- [69] T. P. Ferguson, J. Qu, “*Moisture absorption analysis of interfacial fracture test specimens composed of no-flow underfill material*”, Journal of Electronic Packaging, Vol. 125, Issue 1, pp. 24-30(2003)
- [70] L. L. Marsh, R. Lasky, D. P. Seraphim, G. S. Springer, “*Moisture solubility and diffusion in epoxy and epoxy-glass composites*”, IBM Journal of Research and Development, Vol. 28, No. 6, pp. 655-661(1984)
- [71] E. H. Wong, K. C. Chan, T. B. Lim, T. F. Lam, “*Non-fickian moisture properties characterisation and diffusion modeling for electronic packages*”, Proceedings of the 49th Electronic Components and Technology Conference, 1999, pp. 302-306

-
- [72] Patent: US provisional US61/043,631, “*Differential pressure flow-rate measuring device*”, 2008
- [73] L. Kleiser, T. Rösgen, “*Fluiddynamik I – Skript zur Vorlesung*”, Lecture notes on Fluid dynamics, Institut für Fluiddynamik, ETH Zürich, Summer 2007
- [74] H. Bruus, *Theoretical Microfluidics*, Oxford University Press, 2008
- [75] www.sensirion.ch
- [76] E. Suhir, Y. C. Lee, C. P. Wong (Editors), J. E. Morris, J. Liu, “*Micro- and Opto-electronic materials and structures, Vol. 2: Physics, mechanics, design, reliability, packaging, chapter 20: Electrically conductive adhesives. a research status review*”, Springer, 2007

List of Figures

2.1	Test device with an array of solder bumps	8
2.2	Design of test devices	10
2.3	Overlaid metal structures of chip and substrate	11
2.4	Process flow of first type devices for gold stud bump assembly	13
2.5	Process flow of devices for solder bump assembly	15
2.6	Flow diagram for the characterisation scheme	17
2.7	Kelvin configuration	18
2.8	4-Point measurement principle	19
2.9	Employed shear test parameters and test setup	20
2.10	SEM micrograph of an array of AuSn20 solder bumps	23
2.11	SEM micrograph of a portion of a solder bump	24
2.12	Process steps for bonding with eutectic AuSn20 solder	25
2.13	Cross sections of a reflowed and a soldered bump	26
2.14	SEM micrograph of an array of stud bumps	28
2.15	Magnified view of a stud bump	29
2.16	Process steps for thermocompression with gold studs	30
2.17	Comparison of hard and soft spheres	32
2.18	SEM micrograph of an array of flattened stud bumps	33
2.19	SEM micrograph of a flattened stud bumps	34
2.20	Process steps for ACA bonding	35
2.21	Photograph of a cross section through an ACA contact	36
2.22	Electrical resistance for the investigated flip chip bonding processes	37
2.23	Influence of measurement geometry on measured resistance value	38
2.24	Photographs of complete and partial wetting	40
2.25	Correlation between contact surface and contact resistance in a ACA joint	42
2.26	Top view on gold stud with ACA-spheres	43
3.1	Pressure strip	45
3.2	Conventional technique to measure pressure profiles	46
3.3	Pressure strip concept	48
3.4	Pressure sensor on PCB	49

3.5	Pressure strip application	50
3.6	Photograph of an assembled pressure strip	51
3.7	Bonding procedure for the pressure strip	52
3.8	Simulation model and description	53
3.9	Simulation of membrane deflection due to a temperature change	54
3.10	Measurement setup for the pressure strip	56
3.11	Characteristic curve for silicone bonded sensors	57
3.12	Characteristic curve for an epoxy-bonded sensor at 120 °C . .	58
3.13	Characteristic curve for an epoxy-bonded sensor at 60 °C . .	59
3.14	Temperature-dependent sensitivity of silicone-bonded pressure sensors	61
3.15	Temperature-dependent sensitivity of epoxy-bonded pressure sensors at 120 °C	62
3.16	Temperature-dependent sensitivity of epoxy-bonded pressure sensors at 120 °C	63
3.17	Comparison of temperature dependent sensitivities of silicone- and epoxy-bonded sensor dies	64
3.18	TCS as a function of temperature for silicone-bonded sensors, which was calculated using adjacent measurement points . . .	64
3.19	Temperature dependence of sensitivity for silicone-bonded pressure sensors	67
3.20	Temperature dependence of sensitivity for epoxy-bonded pressure sensors at 120 °C	68
3.21	Temperature dependence of offset for epoxy-bonded pressure sensors at 120 °C	69
3.22	Comparison of temperature dependent offset of silicone- and epoxy-bonded sensor dies	70
3.23	Temperature-induced error in pressure measurement with epoxy-bonded sensors	70
3.24	Comparison of standard pressure tap readings and pressure strip measurements	71
3.25	Thin polyimide film with fluidic channels and metal structures	72
4.1	Flip chip with ACA on PMMA for microfluidic applications .	75
4.2	Flip chip bonding of pressure sensors	76
4.3	PMMA platform with several flip chip bonding sites	79
4.4	Photograph of a cross section through an ACA-on-PMMA contact	80
4.5	Electrical resistance for the investigated flip chip bonding processes including the ACA-on-PMMA-process	81
4.6	Silicon platform with ACA-bonded PMMA dies	81

4.7	Temperature cycling results for ACA bonding on glass with a bonding force of 13 g/bump	88
4.8	Temperature cycling results for ACA bonding on glass with a bonding force of 3 g/bump	89
4.9	Accumulative failure of ACA-on-PMMA and ACA-on-glass samples	90
4.10	Cross section of ACA-joint with bonding force 400 g and temperature 180 °C	91
4.11	Cross section of ACA-joint with bonding force 100 g and temperature 180 °C	92
4.12	Cross section of ACA-joint with bonding force 400 g and temperature 90 °C	93
4.13	Contact resistances of PMMA substrates with flip chip ACA-bonded Si-chips after autoclaving	94
4.14	Structured borofloat substrate with flipped pressure sensors .	97
4.15	Bottom view photograph of ACA-bonded pressure sensors . .	98
4.16	Characteristic output signal as function of pressure for sensor 1	99
4.17	Characteristic output signal as function of pressure for sensor 2	99
4.18	Characteristic output signal as function of pressure for sensor 3	100
4.19	Offset signal as a function of temperature for sensor 1	101
4.20	Offset signal as a function of temperature for sensor 2	101
4.21	Offset signal as a function of temperature for sensor 13	102
4.22	Offset drift within six hours	102
4.23	Simulation model	105
4.24	Plot of moisture concentration in the underfill ring after three hours	106
4.25	Evolution of the total moisture in the underfill	107
4.26	Colour plot of hygro swelling of the underfill	108
4.27	Simulation of hygro swelling induced deflection along the diagonal of the diaphragm	109
4.28	Colour plot of thermally induced deformation of the device .	110
4.29	Diaphragm deflection induced by hygro swelling of the underfill and by a mismatch of the CTEs	112
5.1	Novel flow sensor concept	114
5.2	Flip chip assembly of pressure sensor	117
5.3	Side view sketch of restriction module and pressure sensor . .	118
5.4	Side view sketch of the complete device	118
5.5	Photographs of the flow sensor	120
5.6	Measurement setup for characterisation of the flow sensor . .	121
5.7	Measurement setup for characterisation of the flow sensor with two water reservoirs	122

5.8	Output signal of the flow sensor as function of the flow	123
5.9	Output signal corresponding to a pressure peak	124
5.10	Offset as function of the temperature	125
5.11	Measurement setup for characterisation of the flow sensor . .	126
B.1	ACA-spheres within a contact surface	132

List of Tables

1.1	Most common flip chip bonding processes	3
2.1	Relevant resistances in the 4-point setup	20
2.2	Parameters for bonding with eutectic AuSn20 solder	24
2.3	Bonding parameters for thermocompression	29
2.4	Bonding parameters for ACA bonding	34
2.5	Most important bonding parameters	39
3.1	Relevant simulation parameters	52
3.2	Bonding procedures	54
3.3	Pressure sensor parameters	55
3.4	Temperature coefficient of span	60
3.5	Temperature coefficient of offset	66
4.1	Contact resistance and serial resistance of 30 bumps	82
4.2	CTE for materials commonly used in flip chip technology	84
4.3	Bonding parameters for ACA bonding on PMMA and on glass	85
4.4	Initial serial resistance of 30 bumps	86
4.5	Temperature cycling results for ACA bonding on PMMA with a bonding pressure of 1.56 MPa	87
4.6	Temperature cycling results for ACA bonding on PMMA with a bonding pressure of 0.39 MPa	87
4.7	Serial resistance of design (b) samples right after manufac- ture, 105 after manufacture, and after autoclaving	93
4.8	Procedure for characterising the flip chip bonded pressure sensors on borofloat Glass	97
4.9	Sensitivity and offset for three sensors flip chip bonded with ACA on a borofloat substrate	100
4.10	Material parameters used in the simulations of hygro swelling and thermomechanical stresses and strains	111
5.1	Comparison of the temperature coefficients of offset (TCO)	126

List of Publications

Patents

US2008223141, N. Schmid, H. F. Knapp, J. Auerswald, C. Bosshard, **M. Fretz**, A.-C. Pliska, *Pressure measurement device and system, and method for manufacturing and using the same*

US provisional US61/1043,631, N. Schmid, **M. Fretz**, H. F. Knapp, J. Auerswald, C. Bosshard, *Differential pressure flow-rate measuring device*

Publications

M. Fretz, T. G. Harvey, A.-C. Pliska, C. Bosshard, “*Flip-Chip Bonding on Polymers: A Die Attachment Method for Low Tg Materials*”, MST-News, No.4/07, August 2007

T. Bach, **M. Fretz**, M. Jazbinšek, P. Günter, “*Double phase conjugate mirror using Sn₂P₂S₆ for injection locking of a laser diode bar*”, Optics Express, Vol.16, No.20, September 2008

Conference proceedings

M. Fretz, “*Simulation of Hygro Swelling Induced Stresses in Flip Chip Interconnects in a Stress-Sensitive Chip-on-Board Configuration*”, CD-Proceedings of COMSOL Conference, Grenoble, October 2007

M. Fretz, J. Auerswald, T. G. Harvey, J. Zhu, N. Schmid, C. Bosshard, “*Flip-Chip Bonding of Sensor Dies on PMMA for Low-Cost Microfluidic Applications*”, Proceedings of 1st European Conference on Microfluidics (muFlu’08), Bologna, Italy, December 2008

N. Schmid, **M. Fretz**, H. F. Knapp, T. Burch, S. Bitterli, Ch. Bosshard, F. Zimmermann, P. Sollberger, T. G. Harvey, “*Towards integrated hybrid microsystems: flexible pressure sensing strips*”, Proceedings of the 3rd European Conference & Exhibition on integration issues of minia-

turized systems – MEMS, MOEMS, ICs, and Electronic Components, SMART SYSTEM INTEGRATION, Brussels, March 10–11, 2009

CSEM annual scientific report

M. Fretz, T. G. Harvey, A.-C. Pliska, C. Bosshard, “*Flip Chip Bonding on Polymers: A Die Attachment Method for Low Tg Materials*”, CSEM scientific report 2006

M. Fretz, T. G. Harvey, J. Auerswald, N. Schmid, A.-C. Pliska, C. Bosshard, “*Flip Chip Bonding on Polymers: Die Attach and Leak-Tight Sealing*”, CSEM scientific report 2007

N. Schmid, **M. Fretz**, S. Bitterli, T. Burch, L. Neumann, J. Auerswald, H. F. Knapp, S. Graf, C. Bosshard, P. Sollberger, F. Zimmermann, Z. Stössel, T. G. Harvey, J. Zhu, R. Hamza, “*Pressure Sensing Strip for Rapid Aerodynamic Testing*”, CSEM scientific report 2007

M. Fretz, N. Schmid, T. G. Harvey, J. Zhu, A.-C. Pliska, C. Bosshard, “*Pressure Sensing Strip: Packaging Aspects*”, CSEM scientific report 2007

M. Fretz, N. Schmid, S. Bitterli, L. Neumann, C. Bosshard, H. F. Knapp, D. Fengels, “*Novel Flow Sensor Concept and Implementation*”, CSEM scientific report 2008

M. Fretz, N. Schmid, T. G. Harvey, J. Zhu, C. Bosshard, “*Flip Chip Bonding on Polymers for Low-Cost Microfluidic Application*”, CSEM scientific report 2008

Acknowledgement

First of all, I would like to express my gratitude to Professor Herzig from the University of Neuchâtel for being my supervisor.

My advisors Christian Bosshard and Anne-Claire Pliska at CSEM did a great job in supporting me during the thesis. Many thanks to them. I always appreciated their competent and friendly support.

I would also like to thank Noa Schmid and Matthias Krieger for many interesting discussions. They let me share their expertises in microfluidics and adhesive bonding.

Undoubtedly, I could profit from Stephan Berchtold, Stefan Bitterli, and Thomas Burch. I thank them for their support in design and fabrication of microfluidic and electronic devices.

I would like to mention my colleagues Markus Lützel Schwab, Jörg Pierer, Sylvain Grossmann, Rony Jose James, and Guido Spinola. I thank them for the pleasant working atmosphere and occasional bike tours and dinners.

Philipp Schmid, Alex Steinecker, Jens Taprogge, and Qun Lai: I thank them for the ping-pong challenges. I am capable now of returning a slice shot.

I would like to thank Rogér Ziltener, formerly employee of Injector Solutions, for sharing his knowledge in solder processes and Tom Harvey and James Zhu from Epigem Ltd. for the good and fruitful collaboration.

Finally, I want to thank Wilfried Noell, Hans Peter Herzig, Tom Harvey, and Christian Bosshard for being (co-) examiners of the defence.

Curriculum Vitae

Name	Mark Fretz
Born	22 August 1979 in Zug (Switzerland)
August 2009	Ph.D. thesis on “ <i>Flip chip bonding technologies for hybrid integration</i> ”
2005–2009	Ph.D. student at CSEM Alpnach in the ‘Optics & Packaging’ group led by Christian Bosshard, in collaboration with Professor Hans Peter Herzig from the Institute of Microtechnology at the University of Neuchâtel
2005	Graduation with a diploma in experimental physics on “ <i>Double phase conjugate mirror for laser beam clean up</i> ”
1999–2005	Studies in Physics at the Swiss Federal Institute of Technology (ETH Zürich). Specialisation in nonlinear optics
1998–1999	Employment as a chauffeur
1992–1998	Grammar school at ‘Gymnasium Immensee’ (SZ, Switzerland)
1986–1992	Primary school in Risch (ZG, Switzerland)